

Chapter 5

RESEARCH ACTIVITIES

5.1 Nuclear physics

N. Madhavan, P. Sugathan and R. P. Singh

During the year, the combined operation of Pelletron plus LINAC accelerators helped to accomplish the completion of many user experiments pending for a long time. This year, eight students have completed their PhD experiments using the GPSC and NAND facilities, performing heavy ion induced reactions. These experiments attempt to address current problems in fusion-fission dynamics by measuring the fission fragment mass distribution and mass gated pre-scission neutron multiplicity. The research topics covered measurements exploring the existence of different modes of fission in Uranium nuclei, presence of asymmetric fission in lead-island isotopes, entrance channel effects on shell closure in fission dynamics, pre-equilibrium neutron emission at high excitation energies etc. In a recent publication, we have reported the impact of multi-chance fission on shell effects observed in mass distribution and fragment mass-neutron correlation in light actinide fission initiating more experiments in this direction. Other detector developmental activities involved the fabrication of assembly frames for micro-channel plate based time-of-flight detector and modular particle identification system for performing multi-nucleon transfer (MNT) reactions for future experiments.

It is also planned to develop a new experimental facility for nuclear physics in beam hall I making use of the low-energy ion beams from upcoming HCI accelerator facility. With the designed energy gain of 1.8 MeV/ nucleon, light ion beams up to ^{20}Ne can be obtained from HCI which can be used for low energy nuclear reaction studies, which has importance in nuclear astrophysics related experiments. To measure the energy and angular distribution of the reaction products, a scattering chamber is being designed and the fabrication will start soon.

Indian National Gamma detector Array (INGA) setup at IUAC was used for experiments to explore both the nuclear structure and heavy ion nuclear reaction dynamics. The experiments were carried out using beams from Pelletron as well as Pelletron-Linac. A CsI based charge particle detector array (CPDA) consisting of 32 detectors and an array of 5 LaBr detectors were used in conjunction with INGA for above studies. The CPDA was used to identify the light charge particles like alpha and protons in coincidence with de-exciting gamma rays. LaBr detectors were used for measurement of lifetime of excited nuclear states in the sub-nanosecond range. Simulation studies for the incorporation of LaBr detectors in INGA were also carried out for inclusion of up to sixteen LaBr detectors. In the last academic year, significant effort was also put on helping the students with the analysis of data in ROOT format. A number of results were published highlighting the dynamical aspect of nuclear structure in various regions of the periodic table. Nuclei close to magic numbers 20, 28, 50 and 82 were studied to examine their high spin structure within the spherical shell model framework. However, many with moderate deformation showed various dynamical aspects such as magnetic, anti-magnetic rotational and wobbling bands. Some nuclei featured more than one aspect in the same nucleus such as chirality, enhanced octupole correlation and magnetic or anti-magnetic rotational bands. It is challenging for any model to depict such varied phenomena. In the reaction dynamics investigations, incomplete fusion at low energy (about 2-6 MeV/A) in heavy ions has been studied. In these studies various aspects which affect fusion (and incomplete fusion), such as structure of the reactants, alpha Q -value of projectiles with α -cluster structure, break-up energy of the projectile etc. were investigated. This

5. RESEARCH ACTIVITIES

year clover gamma detectors were also used in a project to study residual activity in some of the building materials. In the last academic year, a workshop on *INGA - Recent results and New Ancillary Devices* and a school on *Nuclear Models for Structure Studies* were held. The workshop was helpful in taking stock of the on-going research work and the school was particularly beneficial to young research scholars.

Heavy Ion Reaction Analyzer (HIRA) and HYbrid Recoil mass Analyzer (HYRA) were used in three and six thesis experiments, respectively, probing sub- and near-barrier fusion, transfer and quasi elastic backscattering processes. The SC-linac campaign in the second half of the academic year was utilized to perform all the six HYRA experiments using high energy beams, two of which were performed with the HYRA + TIFR 4π spin spectrometer for evaporation residue (ER) spin distribution measurements. A split-anode, deep ionization detector has been developed and commissioned at the focal plane of HIRA facility. Tests with α -particle and fission fragment sources will be followed by a facility test with beam-induced nuclear reactions prior to making it available for users. The addition of this detector will be immensely useful in background reduction and / or particle identification in measurements involving low cross sections. A two-day workshop on HIRA / HYRA and a week-long school on nuclear reactions helped in consolidating the activities / plans for these facilities and in training the next set of around fifty research scholars, respectively. A total of four manuscripts were published and a few more were submitted (or under review) based on earlier experiments with these two facilities. The work carried out by the group members were presented in FUSION23 conference held in Shizuoka, Japan during November 19 - 24, 2023. Thus, the academic year 2023 - 2024 was quite successful in reducing the backlog in AUC-sanctioned experiments and in preparing the young researchers for the future.

5.1.1 Study of transfer reactions in $^{28}\text{Si}+^{140,142}\text{Ce}$ using a recoil separator

Chandra Kumar¹, Gonika¹, J. Gehlot¹, Phurba Sherpa², Anjali Rani², A. Parihari³, Anjali Merin⁴, Abhijit Bairagya⁵, K. Prameela⁶, N. Madhavan¹ and S. Nath¹

¹Inter-University Accelerator Centre, Aruna Asaf Ali Marg, New Delhi 110067

²Department of Physics & Astrophysics, University of Delhi, Delhi 110007

³Dept. of Physics, Rajdhani College, University of Delhi, Delhi 110015

⁴Department of Physics, Central University of Kerala, Kasargod 671320

⁵Department of Physics, Visva-Bharati, Santiniketan, Bolpur 731235

⁶Department of Nuclear Physics, Andhra University, Visakhapatnam 530003

Heavy ion-induced multi-nucleon transfer (MNT) reactions [1] are important for studying the transition from quasielastic to deep-inelastic regime, production of heavy neutron rich nuclei and probing nucleon-nucleon correlation. MNT channels are also known to influence fusion dynamics near and below the Coulomb barrier. Transfer products are often identified by electromagnetic recoil separators. A new generation of large acceptance magnetic spectrometers (see *e.g.* Ref. [2]) have been commissioned to study transfer reactions in which the projectile-like ions are identified by reconstruction of their trajectories. Transfer reactions can also be studied around the Coulomb barrier using conventional separators by detecting the heavier target-like ions in forward angles in the laboratory frame. This technique was first employed to study one-neutron ($1n$) and two-neutron ($2n$) transfer channels in $^{58}\text{Ni}+^A\text{Sn}$ systems [3], using the Daresbury recoil mass spectrometer.

Transfer yields are often normalized by the yield of the elastic channel to obtain transfer probabilities [4]. Biswas *et al.* reported a methodology [6,7] to extract differential cross sections from measured yields of quasielastic events at the focal plane of the Heavy Ion Reaction Analyzer (HIRA) [8]. One-proton ($1p$) and two-proton ($2p$) stripping excitation functions for an intermediate mass system [9] were recently measured with a recoil separator for the first time, using this methodology.

We report here new measurements of transfer excitation functions for the systems $^{28}\text{Si}+^{140,142}\text{Ce}$ at centre of mass (c.m.) angle, $\theta_{\text{c.m.}} = 180^\circ$ using the HIRA. The target-like ions have been transported to the focal plane and detected by a position-sensitive multi-wire proportional counter. The spectrum between χ -position and time-of-flight (TOF) of the target-like ions for the system $^{28}\text{Si}+^{142}\text{Ce}$ at $E_{\text{lab}} = 115$ MeV is shown in Fig. 5.1. The reaction products are dispersed according to their mass over charge state $\left(\frac{A}{q}\right)$ values at the focal plane of the HIRA. To eliminate the possibility of any ambiguity in channel identification, the experimental spectrum has been compared with a simulated spectrum generated using a Monte-Carlo code [7]. We are performing coupled reaction channel (CRC) calculations [10] to understand the mechanism of transfer of nucleon(s) in this system. The methodology adopted in this work can be adapted for measuring transfer cross sections using similar devices.

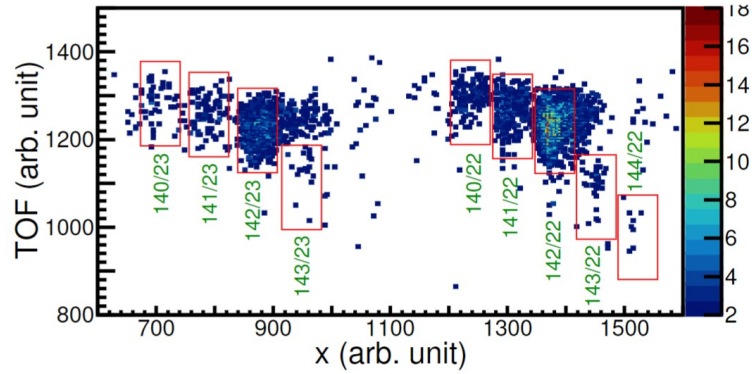


Figure 5.1: Transfer channels identified at the focal plane of the HIRA with $\frac{A}{q}$ values.

References:

1. L. Corradi, G. Pollarolo and S. Szilner, J. Phys. G: Nucl. Part. Phys. **36**, 113101 (2009).
2. F. Cappuzzello, C. Agodi, D. Carbone and M. Cavallaro, Eur. Phys. J. A **52**, 167 (2016).
3. R. R. Betts, P. M. Evans, C. N. Pass, N. Poffé *et al.*, Phys. Rev. Lett. **59**, 978 (1987).
4. Sunil Kalkal, S. Mandal, N. Madhavan, A. Jhingan *et al.*, Phys. Rev. C **83**, 054607 (2011).
5. S. Nath, Comput. Phys. Commun. **179**, 492 (2008);
6. Rohan Biswas and S. Nath, Eur. Phys. J. A **56**, 1 (2020).
7. Rohan Biswas, Sunil Kalkal and S. Nath, Eur. Phys. J. A **57**, 9 (2021).
8. A. K. Sinha, N. Madhavan, J. J. Das, P. Sugathan *et al.*, Nucl. Instrum. Methods A **339**, 543 (1994).
9. Rohan Biswas, S. Nath, J. Gehlot, Gonika *et al.*, Eur. Phys. J. A **59**, 60 (2023).
10. Ian J. Thompson, Comput. Phys. Rep. **7**, 167 (1988); <http://www.fresco.org.uk>

5.1.2 Probing the influence of weak channels on fusion dynamics in $^{28}\text{Si}+^{140,142}\text{Ce}$ near the barrier

Chandra Kumar¹, Gonika¹, J. Gehlot¹, Phurba Sherpa², A. Parihari³, K. Kundalia⁴, Ashna B.⁵, Amar Das⁶, Rajesh K. Sahoo⁷, Rayees Ahmad Yattoo⁸, Md. Moin Shaikh⁹, Sunil Kalkal⁸, N. Madhavan¹ and S. Nath¹

¹Inter-University Accelerator Centre, Aruna Asaf Ali Marg, New Delhi 110067

²Department of Physics & Astrophysics, University of Delhi, Delhi 110007

³Dept. of Physics, Rajdhani College, University of Delhi, Delhi 110015

⁴Department of Physics, Bose Institute, 93/1 APC Road, Kolkata 700009

⁵Department of Physics, Central University of Kerala, Kasargod 671320

⁶Department of Physics, Gauhati University, Guwahati 781014

⁷Department of Physics, Central University of Jharkhand, Ranchi 835222

⁸Department of Physics and Material Science, Thapar Institute of Engineering and Technology, Patiala

⁹Department of Physics, Chanchal College, Malda 732101, West Bengal

Heavy ion-induced fusion reactions near the Coulomb barrier provide an excellent probe to explore the structure of participating nuclei and the influence of weak channels, such as transfer channels [1,2]. Numerous experiments and theoretical studies have shown that nuclear deformations influence fusion reactions, often enhancing fusion cross-sections compared to the predictions of the one-dimensional barrier penetration model (1D-BPM), which treats nuclei as structure-less entities. However, the impact of transfer channels on fusion dynamics is not as straightforward as that of deformations. While some systems exhibit significant enhancement in fusion cross-sections due to transfer channels [2,3], this is not universally observed across all systems [4]. Although many systematic studies have been conducted, there are still exceptions that do not follow the general trends [5].

Therefore, to explore the effect of transfer channels on fusion dynamics, we measured the fusion reactions of $^{28}\text{Si}+^{140}\text{Ce}$ and $^{28}\text{Si}+^{142}\text{Ce}$ near the Coulomb barrier. The $^{28}\text{Si}+^{140}\text{Ce}$ system has $2n$ and $4n$ positive Q -value transfer channels, while the $^{28}\text{Si}+^{142}\text{Ce}$ system has positive Q -value transfer channels ranging from $1n$ to $6n$. The measurement of fusion reactions for the $^{28}\text{Si}+^{140,142}\text{Ce}$ systems was conducted using the Heavy Ion Reaction Analyzer (HIRA) [6]. Projectile energies ranged from 103.5 MeV to 136 MeV in the laboratory frame, with steps of 1.5 MeV and 3 MeV. HIRA was optimized to detect evaporation residues by adjusting its electric and magnetic fields.

5. RESEARCH ACTIVITIES

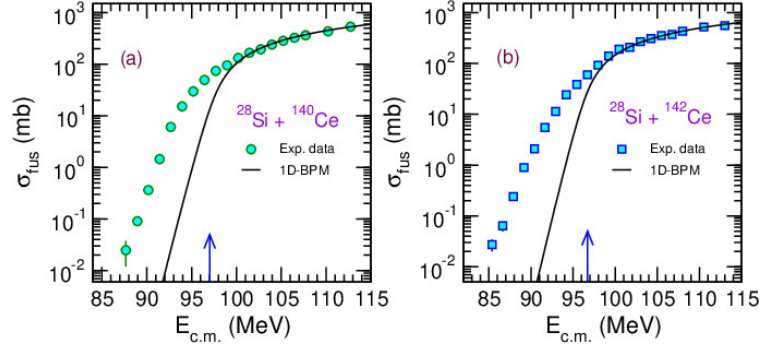


Figure 5.2: Fusion excitation functions for the systems (a) $^{28}\text{Si}+^{140}\text{Ce}$ and (b) $^{28}\text{Si}+^{142}\text{Ce}$. The arrow in each frame indicates location of the Coulomb barrier.

These ions were identified using a multi-wire proportional counter (MWPC) located at the focal plane of the HIRA, which had dimensions of $150 \times 50 \text{ mm}^2$. To distinguish between scattered beam-like particles and desired reaction products at the focal plane, we measured the time-of-flight of the ions. The start signal was derived from the MWPC anode, while the RF signal served as the stop.

The result of the data analysis for the fusion measurement is shown in Fig. 5.2, where the obtained fusion cross-sections are compared with predictions from the 1D-BPM, calculated by CCFULL [7]. The theoretical cross-section underestimates the observed values significantly, indicating the influence of internal degrees of freedom. Detailed theoretical calculations are currently underway to provide a more fundamental understanding of these effects.

References:

1. Giovanna Montagnoli and Alberto M. Stefanini, *Eur. Phys. J. A*, **59**, 138 (2023).
2. M. Beckerman *et al.*, *Phys. Rev. Lett.*, **45**, 1472 (1980).
3. Rudra N. Sahoo *et al.*, *Phys. Rev. C*, **102**, 024615 (2020).
4. H. M. Jia *et al.*, *Phys. Rev. C*, **86**, 044621 (2012).
5. V. V. Sargsyan *et al.*, *Phys. Rev. C*, **86**, 014602 (2012).
6. A. K. Sinha *et al.*, *Nucl. Instrum. Methods A* **339**, 543 (1994).
7. K. Hagino *et al.*, *Comput. Phys. Comm.* **123**, 143 (1999).

5.1.3 Study of entrance channel effect on fusion-fission dynamics for $A \sim 200$

Phurba Sherpa¹, Shashi Verma¹, I. Majumdar², Jhilam Sadhukhan^{3,4}, N. Madhavan⁵, S. Nath⁵, J. Gehlot⁵, Gonika⁵, Chandra Kumar⁵, A. Parihari⁶, K. Chakraborty¹, P. S. Rawat¹, P. Khandelwal¹, N. Patel¹, Renu Kumari¹, Amninderjeet Kaur⁷, Taniya M. Sonowal⁸, Komal⁷, Neeraj Kumar⁹ and S. Mandal¹

¹Department of Physics & Astrophysics, University of Delhi, Delhi 110007, India

²Tata Institute of Fundamental Research, Mumbai 400005, India

³Physics Group, Variable Energy Cyclotron Centre, Kolkata 700064, India

⁴HBNI, Training School Complex, Anushaktinagar, Mumbai 400094, India

⁵Inter-University Accelerator Centre, Aruna Asaf Ali Marg, New Delhi 110067, India

⁶Rajdhani College, University of Delhi, Raja Garden, New Delhi 110015, India

⁷Department of Physics, Panjab University, Chandigarh 160014, India

⁸Department of Physics, Gauhati University, Guwahati 781014, India and

⁹Institut Pluridisciplinaire Hubert Curien, CNRS/IN2P3-UDS, 67037 Strasbourg Cedex 2, France

Entrance channel effects play important roles in the heavy ion-induced fusion mechanism. Significant fusion inhibition has been observed for the reaction following symmetric entrance channel at the mass region $A \sim 200$ [1,2]. Evaporation residue (ER) and ER-gated spin distribution measurements are most sensitive probe to study such effects in the presaddle fusion-fission dynamics [3,4]. These measurements were performed for two different reactions, using the HYbrid Recoil mass Analyzer (HYRA) coupled with the TIFR 4π spin spectrometer at IUAC. The first reaction involved the nuclei ^{48}Ti and ^{160}Gd while the second reaction involved ^{30}Si and ^{178}Hf . Both reactions formed the same compound nucleus $^{208}\text{Rn}^*$.

Pulsed beams of ^{48}Ti and ^{30}Si , with pulse separation of 250 ns and 2 μs , respectively, were used. The measurements were carried out at several energies, which ranged from around the Coulomb barrier to 20% above the barrier. Magnetic fields and the gas pressure of HYRA was optimised to ensure the maximum transmission of ERs to the focal plane. These ERs were detected using a position sensitive multi-wire

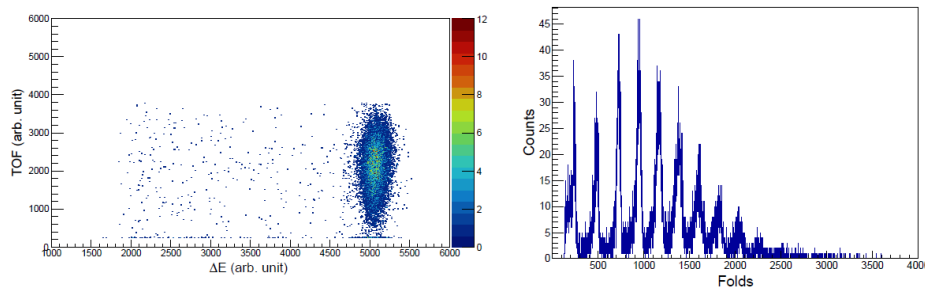


Figure 5.3: Scatter plot between ΔE and TOF and (b) ER-gated γ -fold distribution for $^{48}\text{Ti}+^{160}\text{Gd}$ at $E_{\text{lab}} = 208.2$ MeV.

proportional counter (MWPC) located at the focal plane. The closely packed 4π array of 29 NaI detectors were placed around the target chamber to capture the emitted γ -rays. Correlation plots between the energy loss (ΔE) and time-of-flight (TOF) of the ERs were used to identify the ERs as shown in the left panel of Fig. 5.3. A clear separation of the ERs from other possible scattered particles reaching the focal plane is evident. ER-gate, from this plot, was then applied to the raw γ -folds to remove the background, as shown in the right panel of Fig. 5.3. Complete analysis of the data, to obtain ER cross sections and ER-gated γ -multiplicity distributions for both the reactions, is underway.

References:

1. A. C. Berriman *et al.*, Nature (London) **413**, 144 (2001).
2. N. Kumar *et al.*, Phys. Lett. B **214**, 136062 (2021).
3. G. Mohonto *et al.*, Phys. Rev. C **88**, 034606 (2013).
4. W. Ye, Phys. Rev. C **83**, 044611 (2011).

5.1.4 Understanding the role of neutron transfer in the sub-barrier fusion of $^{32}\text{S}+^{138}\text{Ba}$ system

Malvika Sagwal¹, Moumita Maiti¹, Rishabh Kumar¹, Pavneet Kaur¹, Himanshu Sharma¹, Yasir Arafat¹, Bharat Kharpuse¹, Gonika², Chandra Kumar², S. Nath², J. Gehlot² and N. Madhavan²

¹Department of Physics, Indian Institute of Technology Roorkee, Roorkee 247667, Uttarakhand, India

²Nuclear Physics Group, Inter-University Accelerator Centre, New Delhi 110067, India

Below the classical Coulomb barrier, the fusion phenomenon in nuclei has been better understood through quantum tunnelling effect. However, compared to the quantum mechanical one-dimensional barrier penetration model (1DBPM), several orders of increase in cross section have been seen for heavy-ion fusion processes in the sub-barrier region [1]. The role of various degrees of freedom of the participating nuclei, such as static and dynamical deformations, couplings among inelastic states, nucleon transfer, etc., has been put forth as a major accountable factor [2]. However, the extent of contribution of each degree of freedom along with their mutual interplay is still being investigated.

We chose to measure the $^{32}\text{S}+^{138}\text{Ba}$ system and compare it with our previous measurement of the $^{30}\text{Si}+^{140}\text{Ce}$ system, where both form the same compound nucleus $^{170}\text{Hf}^*$. For the former system, the Q -values are positive up to $6n$ pickup by the projectile from the target. Contrarily, they are all negative for the latter system. Understanding the sub-barrier fusion enhancement in excitation function using theoretical frameworks can aid the knowledge of structural features of the nuclei and couplings to transfer channels.

The experiment was performed at the 15UD Pelletron and LINAC facility of IUAC, incorporating 1st stage of the Hybrid Recoil mass Analyzer (HYRA) [3]. To carry out the evaporation residue (ER) cross-section measurement, ^{138}Ba target having $200 \mu\text{g}/\text{cm}^2$ thickness [4] was bombarded with ^{32}S beam. In the present run, the beam energy (E_{lab}) was varied between 154 - 132 MeV, spanning 17% above to near the Coulomb barrier, while the lower energy data (up to 10% below the barrier) were collected in the previous run. To normalize the ER counts absolutely, two Passivated Implanted Planar Silicon (PIPS) detectors were mounted in the target chamber. The Helium gas pressure and the magnetic field settings of the HYRA were optimized through an in-house code to result in the maximum transmission of ERs and rejection of the scattered beam-like particles. The ERs were directed to the focal plane and detected by a multi-wire proportional counter (MWPC) of $15.0 \times 5.0 \text{ cm}^2$ area. Two-dimensional energy loss (ΔE) versus time-of-flight

5. RESEARCH ACTIVITIES

(TOF) spectra were generated at each energy to identify and gate the ER counts distinctly. The data were acquired through the IUAC software NIAS-MARS and analyzed using the ROOT framework. The total ER cross-section was calculated through the formalism given below

$$\sigma_{\text{ER}} = \frac{Y_{\text{ER}}}{Y_{\text{mon}}} \left(\frac{d\sigma}{d\Omega} \right)_{\text{R}} \Omega_{\text{mon}} \frac{1}{\epsilon_{\text{HYRA}}}, \quad (5.1)$$

where Y_{ER} and Y_{mon} are the yields of ERs at the focal plane and of the scattered particles at the monitor (PIPS) detectors, respectively, $\left(\frac{d\sigma}{d\Omega} \right)_{\text{R}}$ is the differential Rutherford scattering cross-section, Ω_{mon} is the solid angle subtended by the monitor detectors at the centre of the target and ϵ_{HYRA} is efficiency of the HYRA.

As the fission probability is negligible for the reaction, $\sigma_{\text{ER}} \simeq \sigma_{\text{fusion}}$. The fusion excitation function has been compared with the coupled-channels code CCFULL [5]. Cross sections are found to be enhanced by several orders of magnitude with respect to the 1DBPM predictions in the sub-barrier region. The $^{32}\text{Si}+^{138}\text{Ba}$ reaction shows additional fusion enhancement compared to the $^{30}\text{Si}+^{140}\text{Ce}$ reaction, which might be due to neutron transfer in the former system. Detailed theoretical calculations are being performed to understand the couplings to transfer channels and structural degrees of freedom of the colliding partners.

References:

1. M. Beckerman, Rep. Prog. Phys. **51**, 1047 (1988).
2. H. Esbensen, G. Montagnoli and A. M. Stefanini, Phys. Rev. C **93**, 034609 (2016).
3. S. Muralithar, N. Madhavana, P. Sugathan, R. P. Singh, A. Jhingan, R. Kumar, S. Nath *et al.*, Eur. Phys. J. A **58**, 250 (2022).
4. K. K. Rajesh, M. M. Musthafa, M. M. Hosamani, A. Shamlath, S. R. Abhilash and D. Kabiraj, Vacuum **141**, 230 (2017).
5. K. Hagino, N. Rowley and A. T. Kruppa, Comput. Phys. Commun. **123**, 143 (1999).

5.1.5 Systematic investigation of the effect of neutron excess in ER survival probability against fission in reactions populating isotopes of Ra

Ashna B.¹, E. Prasad¹, N. Madhavan², S. Nath², J. Gehlot², Gonika², Anjali Merin¹, Chandra Kumar², Varsha K. V.¹, A. M. Vinodkumar³, S. K. Duggi⁴, Ramakrishna Reddy⁴, K. Prameela⁴, S. Appannababu⁴, Jinu K. V.³, P. Manju¹ and Rayees Ahmad Yatoo⁵

¹Department of Physics, Central University of Kerala, Kasaragod 671316, India

²Inter-University Accelerator Centre, Aruna Asaf Ali Marg, New Delhi 110067, India

³Department of Physics, University of Calicut, Calicut 673635, India

⁴Department of Nuclear Physics, Andhra University, Visakhapatnam 530003, India

⁵Thapar Institute of Engineering and Technology, Patiala 147004, India

Comprehending the nuclear reaction dynamics and the factors determining its outcome in the superheavy mass region is challenging [1]. The effect of neutron excess in ER survival probability against fission in heavy ion fusion reactions is a matter of considerable interest. The quasifission (QF) process [2], in which the system reseparates before reaching a compact compound nucleus (CN), is a significant hurdle in forming heavy and superheavy evaporation-residues (ERs) in heavy-ion induced reactions. It is reported that QF is present in $^{30}\text{Si}+^{186}\text{W}$ reaction[3]. Conclusive evidence of QF can be inferred from anomalous fission fragment angular anisotropies, broadened fission fragment mass distributions, mass-angle correlations and strong reduction in ER cross-section [3]. So we are interested to study the N/Z effect in fusion and QF.

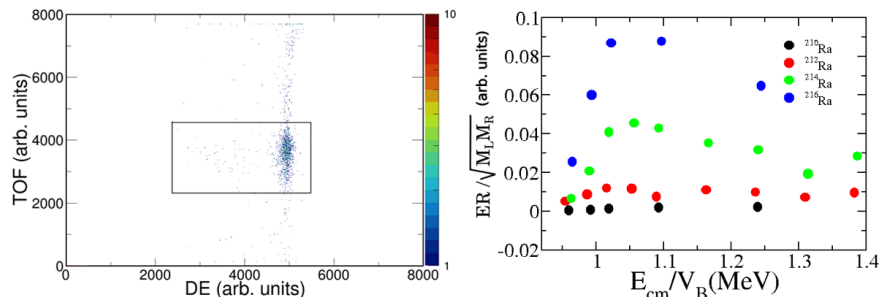


Figure 5.4: ΔE versus TOF for $^{30}\text{Si}+^{184}\text{W}$ at $E_{\text{lab}} = 160$ MeV (left) and $E_{\text{c.m.}}/V_{\text{B}}$ versus $\text{ER}/\sqrt{M_{\text{L}}M_{\text{R}}}$ for isotopes of Ra.

The ER excitation function measurement was performed at the 15UD Pelletron+LINAC facility of IUAC. Pulsed $^{28,30}\text{Si}$ beam with 2 μs pulse separation was used to bombard the isotopically enriched $^{182,184,186}\text{W}$ targets of thickness 400 $\mu\text{g}/\text{cm}^2$, 200 $\mu\text{g}/\text{cm}^2$ and 300 $\mu\text{g}/\text{cm}^2$, respectively on 25 $\mu\text{g}/\text{cm}^2$ thick carbon backing at laboratory energies (E_{lab}) in the range of 133 to 192 MeV. ERs were separated from the intense beam background using the HYbrid Recoil mass Analyzer (HYRA) [4]. Two silicon detectors were used inside the target chamber, placed at $\theta = 26^\circ$, to detect the Rutherford scattered beam-like particles for absolute normalization of ER cross sections. These detectors were also used for positioning the beam at the center of the target. The ERs reaching the focal plane were detected using a position sensitive multi-wire proportional counter (MWPC). Time-of-flight (TOF) spectra were generated with the timing pulse from the MWPC anode as start and the radio frequency (RF) signal, delayed suitably, as stop. The energy loss (ΔE) vs TOF spectra helped in unambiguous identification of ERs (left panel of Fig. 5.4) amidst the beam-like contamination. Normalized ER yields for isotopes of Ra ($\text{ER}/\sqrt{M_{\text{L}}M_{\text{R}}}$; M_{L} and M_{R} are yields of the left and the right monitor detectors, respectively) are plotted as a function of $E_{\text{c.m.}}/V_{\text{B}}$ in the right panel of Fig. 5.4, where V_{B} is the Coulomb barrier.

References:

1. Yu. Ts. Oganessian *et al.*, Phys. Rev. Lett. **109**, 162501 (2012).
2. D. J. Hinde *et al.*, Phys. Rev. Lett. **74**, 1295 (1995).
3. A. C. Berriman *et al.*, Nature (London) **413**, 144 (2001).
4. N. Madhavan *et al.*, Pramana - J. Phys. **75**, 317 (2010).

5.1.6 Measurement of ER cross-sections for $^{48}\text{Ti}+^{124}\text{Sn}$ reaction

Amninderjeet Kaur¹, A. Kumar¹, Komal¹, Basant¹, Neha Dhanda¹, Raghav¹, B. R. Behera¹, N. Madhavan², S. Nath², J. Gehlot², Gonika², Chandra Kumar², Phurba Sherpa³, M. Anser⁴ and H. P. Sharma⁴

¹Department of Physics, Panjab University, Chandigarh 160014

²Inter-University Accelerator Centre, Aruna Asaf Ali Marg, New Delhi 110067

³Department of Physics and Astrophysics, University of Delhi, Delhi 110007

⁴Department of Physics, Banaras Hindu University, Uttar Pradesh 221005, India

To study the sub-barrier fusion enhancement phenomena and the effect of couplings on sub-barrier fusion cross-sections, we have measured the evaporation residue (ER) cross-sections for $^{48}\text{Ti}+^{124}\text{Sn}$ system using the HYRA facility. These measurements were done at 10 energy points in the range of 6% below and 11% above the Coulomb barrier. ^{48}Ti beam was accelerated up to 197.6 MeV using the Pelletron+linac facility and was bombarded on a ^{124}Sn target having thickness 100 $\mu\text{g}/\text{cm}^2$ with carbon backing of thickness 20 $\mu\text{g}/\text{cm}^2$. In the target chamber, two silicon detectors were placed at a distance of 42 mm from the target ladder, making an angle of 26.1 with respect to the beam direction. These detectors were used for the detection of elastically scattered ^{48}Ti ions for Rutherford cross-section normalization and positioning the beam at the centre of the target. ERs formed in the target chamber were detected by a multi-wire proportional counter (MWPC) of dimension $15 \times 5 \text{ cm}^2$, placed at the focal plane. We compared the results obtained from this experiment with our earlier measurement on $^{30}\text{Si}+^{142}\text{Ce}$ system to understand the effects of entrance channel mass-asymmetry and deformation of the colliding nuclei on fusion cross sections.

Fig. 5.5 shows the measured ER cross-sections for $^{48}\text{Ti}+^{124}\text{Sn}$. We also performed coupled-channels calculations using the code CCFULL [1]. Experimental results overpredicts the one-dimensional barrier penetration model cross-sections, as shown in the figure. To explain the below-barrier enhancement of cross sections, we included couplings both in projectile and target nuclei. We used the Akyüz-Winther parameterization for nuclear potential in the present calculations [2]. The data were reproduced reasonably well after inclusion of couplings, in the measured energy range, as shown in Fig. 5.5.

References:

1. K. Hagino, N. Rowley and T. Kruppa, Comput. Phys. Commun. **123**, 143 (1999).
2. R. A. Broglia and A. Winther, Heavy Ion Reactions, (Benjamin Cummings, San Francisco, 1981).

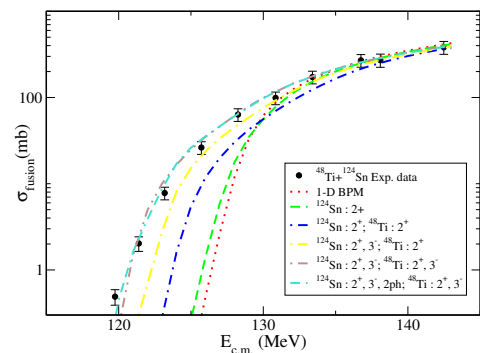


Figure 5.5: Measured and calculated ER excitation functions for $^{48}\text{Ti}+^{124}\text{Sn}$.

5. RESEARCH ACTIVITIES

5.1.7 Measurement of quasielastic scattering excitation functions and barrier distributions

Amar Das^{1,2}, K. Kalita², Harun Al Rashid^{2,3}, Lakhyajit Sarma², Nabendu Kumar Deb^{2,4}, Taniya Sonowal², Anita Tamang², M. Bhuyan⁵, Chandra Kumar⁶, Rajesh Kumar Sahoo⁷, Bhargav Baruah⁸, Rasna Baruah⁸, Anamika Parihari⁹, Madhuchanda Swain¹⁰, Gonika⁶, J. Gehlot⁶, S. Nath⁶ and N. Madhavan⁶

¹Department of Physics, Suren Das College, Hajo Assam, India

²Department of Physics, Gauhati University, Guwahati 781014, Assam, India

³Department of Physics Baoci Banikanta Kakati College, Nagaon, Barpeta, Assam, India

⁴Department of Physics Kamrup College, Chamata, Nalbari Assam, India

⁵Department of Physics, Rangia College, Rangia 781354, Assam, India

⁶Inter-University Accelerator Centre, New Delhi 110067, India

⁷Department of Physics, Central University of Jharkhand, Ranchi, India

⁸Department of Physics, Cotton University, Guwahati, Assam, India

⁹Department of Physics, Rajdhani College, Delhi University, New Delhi, India

¹⁰Cenurion University of Technology and Management, Odisha

We report here our measurement of quasielastic scattering (QES) for the systems $^{16}\text{O}+^{116}\text{Sn}$, ^{176}Yb , ^{178}Hf , considering both spherical and deformed targets. Measurements were carried out at back angles (for projectile-like ions) and at 180° (for target-like ions) simultaneously using the Heavy Ion Reaction Analyzer (HIRA) at IUAC. For the study of QES at 180° , the HIRA was set at 0° [1]. The measurements were performed in the range of $0.78V_C$ to $1.09V_C$ for $^{16}\text{O}+^{116}\text{Sn}$ and $0.78V_C$ to $1.10V_C$ for $^{16}\text{O}+^{176}\text{Yb}$, ^{178}Hf ; V_C is the Coloumb barrier. QES barrier distribution (BD) was extracted from excitation functions using the point difference formula. Our aim was to measure excitation functions for spherical and deformed targets to see the effects of deformation and couplings on the BD. In our preliminary analysis, effect of the hexadecapole deformation of ^{176}Yb on BD could be seen against the reported values from 0.012 to -0.059 [2,3].

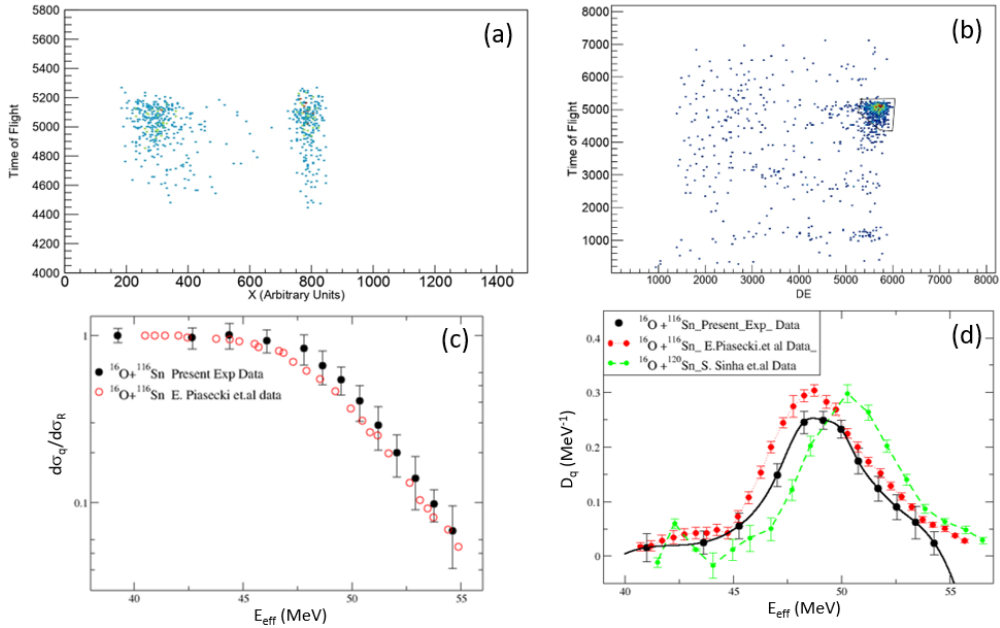


Figure 5.6: (a) X-TOF spectrum for $^{16}\text{O}+^{178}\text{Hf}$ at $E_{\text{lab}} = 77$ MeV, (b) ΔE -TOF spectrum for $^{16}\text{O}+^{178}\text{Hf}$ at $E_{\text{lab}} = 77$ MeV, (c) excitation function for $^{16}\text{O}+^{116}\text{Sn}$ and (d) the corresponding barrier distributions.

We used two silicon detectors at backward angles of 150° and 138.5° to measure the projectile-like ions. The target-like ions were measured using a multi-wire proportional counter (MWPC) placed at the HIRA focal plane. Two monitor detectors were used for absolute normalization. Scatter plots between ΔE -TOF and X-TOF for $^{16}\text{O}+^{178}\text{Hf}$ are, respectively, shown in panels (a) and (b) of Fig. 5.6. Excitation function for O+Sn system from the present work along with the data obtained from Refs. [4] are shown in Fig. 5.6(c) while the corresponding barrier distributions [4,5] are depicted in Fig. 5.6(d). Detailed analysis of the data is in progress.

References:

1. Rohan Biswas and S. Nath, Eur. Phys. J. A **56**, 1 (2020).
2. H. J. Wollersheim, W. Wilcke and T. W. Elze, Phys. Rev. C **11**, 2008 (1975).
3. P. Möller, Nucl. Phys. A **142**, 1 (1970).
4. E. Piasecki, M. Kowalczyk, K. Piasecki *et al.*, Phys. Rev. C **65**, 0546119 (2002).
5. Shrabani Sinha, M. R. Pahlavani, R. Varma, R. K. Choudhury, B. K. Nayak and A. Saxena, Phys. Rev. C **64**, 024607 (2001).

5.1.8 Probing low and high spin states of nuclei of A~70 mass region through heavy-ion induced gamma spectroscopy

Sramana Biswas¹, K. Bhandary¹, A. Goswami¹, S. Barman¹, A. Biswas¹, S. Maiti¹, A. K. Mondal¹, U. S. Ghosh², S. Rai¹, K. Mondal¹, S. Mondal¹, Soumyajit Biswas¹, B. Mukherjee¹, A. Chakraborti¹, U. D. Pramanik³, Yashraj², I. Bala², K. Kartre², A. Sharma², R. P. Singh² and S. Muralithar²

¹Department of Physics, Visva-Bharati, Santiniketan, West Bengal 731235, India

²Inter-University Accelerator Center, New Delhi 110067, India

³Saha Institute of Nuclear Physics, 1/AF Bidhannagar, Kolkata, West Bengal 700064, India

A variety of physical phenomena can be investigated through heavy-ion induced fusion evaporation reaction in the mass region A~60-70. The nuclei in this mass region, having ⁵⁶Ni as core, are excellent candidates to explore competition between single particle and collective excitation. Existence of strong coupling between intruder $1g_{9/2}$ and normal $2p_{3/2}$ orbitals play an important role in deciding the deformation of nuclei in this region [1,2]. Low lying negative parity states is one of the compelling indicators of reflection asymmetry which is important in the context of octupole correlation [3]. Heavy ion induced reaction is needed to extent the level scheme to higher spin state. We were aimed to explore low as well as high spin states of nuclei in this mass region through heavy ion beam.

In order to populate nuclei in A~70 mass region a beam of ²⁸Si at 100 MeV lab energy was produced by the 15UD Pelletron accelerator at the Inter University Accelerator Center (IUAC) New Delhi. The beam was bombarded onto a ⁴⁸Ti target of thickness 1 mg/cm² backed by 8 mg/cm² ¹⁹⁷Au. The emitted gamma rays were detected in coincidence mode with 16 Compton suppressed HPGe clover detectors of the Indian National Gamma Array (INGA) set up.

Analysis of the data is done with the help of the standard analysis packages viz., CANDLE [4], RADWARE [5] and INGASORT [6]. A gamma-gamma coincidence matrix is formed after data sorting (left panel of Fig. 5.7). Populated nuclei are confirmed by gating the gamma energies.

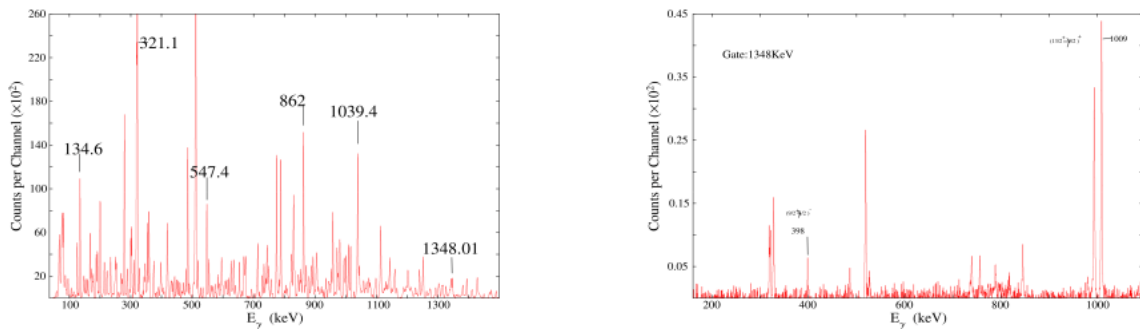


Figure 5.7: (Left) A typical gamma ray spectrum obtained from experimental data and (right) coincidence spectrum of ⁶⁹Ge, gated on 1348 KeV.

⁶⁹Ge, ⁷²Se, ⁷⁰As and other nuclei in the mentioned mass region with a desirable cross-section. Coincidence spectra of ⁶⁹Ge which is gated on 1348 KeV gamma energy is shown in the right panel of Fig. 5.7. In a recent work $15/2^-$ state is found as octupole rotational band [3]. The coupling between $1g_{9/2}$ particle orbital and 3^- octupole state takes major part in making $15/2^-$ state. Se isotopes also shows the octupole correlation. Further investigation and data analysis is in progress.

5. RESEARCH ACTIVITIES

Acknowledgements: The authors would like to acknowledge financial support from UGC-DAE CSR Kolkata Centre (project No.CRS/2021-22/02/468), SERB, New Delhi(project No.CRG/ 2020/000715), IUAC, New Delhi (project No. UFR-67309). Our gratitude extends to Mr. Abhilash S. R. and Dr. D. Kabiraj of the Target Laboratory at IUAC for their assistance in target preparation.

References:

1. F. Becker, et al., Nucl. Phys. A **626**, 799 (1997).
2. A. Mukherjee, et al., Phys. Rev. C **105**, 014322 (2022).
3. C. G. Wang, et al., Phys. Rev. C **106**, L011303 (2022).
4. D. C. Radford, Nucl. Instrum. Methods Phys. Res., Sect. A **361**, 297 (1995).
5. R. K. Bhowmik, et al., in Proceedings of the 44th DAE-BRNS Symposium on Nuclear Physics, p. 422.

5.1.9 Spectroscopic study of rare earth nuclei produced in the fusion-fission reaction

A. Choudhary¹, V. Kumar¹, Y. P. Singh¹, Gobind Ram¹, Samant Kumar Yadav¹, M. K. Sharma¹, Abhishek Yadav², Dhananjaya Sahoo³, A. Y. Yeo³, Yashraj⁴, U. S. Ghosh⁴, Indu Bala⁴ and R. P. Singh⁴

¹Department of Physics, University of Lucknow, Lucknow 226007, India

²Department of Nuclear Science and Technology, Amity University, Noida 201302, India

³Department of Physics, Indian Institute of Technology Roorkee, Roorkee 247667, India

⁴Inter-University Accelerator Centre, New Delhi 110067, India

It is important for the study of the structure of atomic nuclei to understand the limits of nuclear existence as functions of neutron and proton number, as well as excitation energy, angular momentum and elongation. The role that microscopic shell corrections play in enhancing and in extending the limits of nuclear stability is central to this understanding. The present work studies rare earth nuclei which could not be produced in fusion evaporation reactions. We used ²⁸Si beam on ¹⁷⁵Lu target at $E_{lab} = 145 - 160$ MeV to produce some of the nuclei through fusion-fission process. Some of the nuclei identified are mentioned below. In addition to the above, we are also pursuing reaction dynamics studies for the same system.

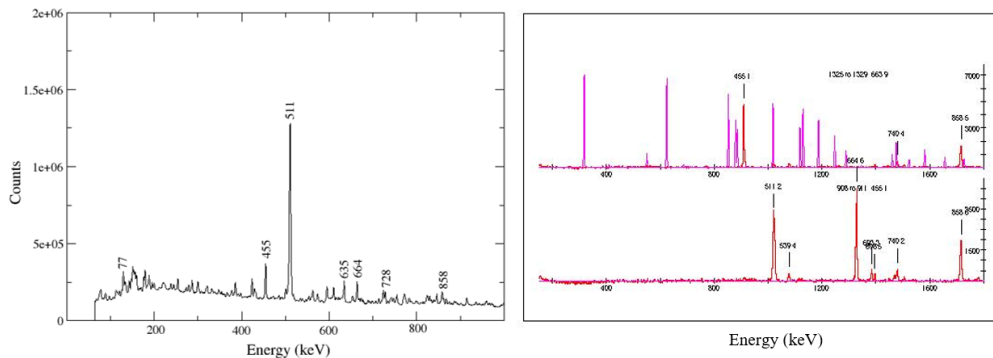


Figure 5.8: Projected spectrum (left) and gated spectrum (right).

At present we are analyzing the data. A two-dimensional $E_\gamma - E_\gamma$ matrix has been sorted with the calibrated and gain matched data. The projection of the matrix is shown in the left panel of Fig. 5.8. A gated spectrum from our preliminary analysis is shown in the right panel of Fig. 5.8. So far, we have identified the following isotopes: ^{70,72,73,74,75}Se, ^{76,77,78,79,80}Kr, ^{78,79,81,84}Sr, ^{76,79,81}Rb and ^{71,72}Br.

5.1.10 Study of neutron multiplicity and mass distribution in Pb region with NAND facility

Raghav¹, B. R. Behera¹, N. K. Rai¹, Amninderjeet Kaur¹, Neha Dhanda¹, Kiran¹, Basant Sura¹, Amit Jangra¹, P. Sugathan², K. S. Golda², Akhil Jhingan², N. Saneesh², Punit Dubey³, Lakhyajeet Sharma⁴ and Avitesh Agrawal⁵

¹Department of Physics, Panjab University, Chandigarh 160014, India

²Inter-University Accelerator Center, New Delhi 110067, India

³Department of Physics, Banaras Hindu University, Varanasi 221005, India

⁴Department of Physics, Gauhati University, Guwahati, Assam 781014

⁵Central University of Haryana, Mahendragarh, Haryana 123031, India

Quasifission (QF) process plays a major role in the suppression of compound nucleus formation. Several experimental as well as theoretical approaches have been adopted to understand the dynamics of Fusion-Fission (FF) and QF processes in heavy nuclei. It is well established that the pre-scission neutron multiplicity is one of the most proficient probes to study the dynamics of heavy-ion induced FF and QF reactions [1]. This is because FF and QF reactions have their own characteristic reaction times, implying

that each reaction process is associated with the different pre-scission neutron multiplicity. Therefore, measurement of pre-scission neutron multiplicities from an isotopic chain will be a suitable tool to disentangle FF and QF processes. With this motivation, we have measured pre-scission neutron multiplicities from two compound nuclei, namely $^{190,198}\text{Pb}$ populated by $^{48}\text{Ti}+^{142,150}\text{Nd}$ systems at 248 to 285 MeV of laboratory energy using the National Array of Neutron Detectors (NAND) facility at IUAC. The pulsed beam of ^{48}Ti with a pulse separation of 250 ns, delivered from the 15UD Pelletron plus LINAC, was bombarded on $^{142,150}\text{Nd}$ targets of thickness $350\ \mu\text{g}/\text{cm}^2$ with carbon backing of $30\ \mu\text{g}/\text{cm}^2$ and carbon capping of $20\ \mu\text{g}/\text{cm}^2$. Two MWPCs ($20 \times 10\ \text{cm}^2$) were kept symmetrically at 57° at a distance of 25 cm each from the target in order to detect the fission fragments. The neutrons were discriminated using the pulse shape discrimination (PSD) based on the zero crossing and TOF technique [2]. Neutrons were detected using 50 organic liquid scintillators (BC501A) in coincidence with either of the fission fragments detected using the two MWPCs. The PSD vs TOF spectrum of neutrons emitted in the fission direction after applying mass gating in detector no. 7054 is as shown in (Fig. 5.9). Gated portion (solid line) shows the neutron events. To reduce the background, the beam dump was placed 4 m downstream from the target and it was shielded with paraffin and lead bricks. The main motive of the data analysis is to extract the mass-gated neutron multiplicity, mass distribution and mass-energy correlations of the binary fission fragments. The simultaneous analysis to determine the mass distribution and neutron multiplicity is in progress.

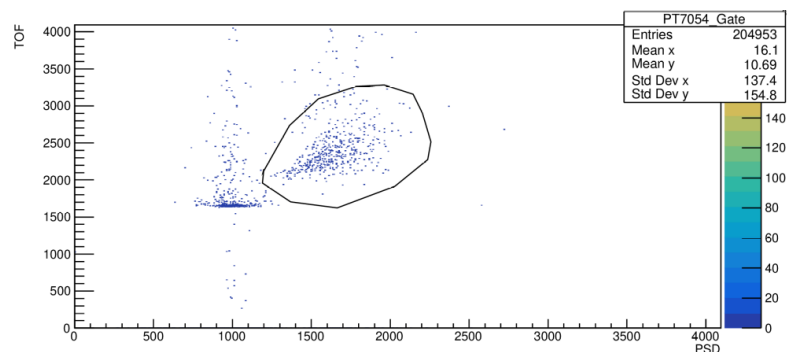


Figure 5.9: PSD versus TOF graph of the neutron detector no. 7054 at 258 MeV energy.

References:

1. D. J. Hinde, et al., Nucl. Phys. A **452**, 550 (1986).
2. S. Venkataramanan, et al., Nucl. Instrum. Methods Phys. Res. A **596**, 248 (2008).

5.1.11 Pre-equilibrium neutron emission at high excitation energies and validation with nuclear reaction models

Swapna Balakrishnan¹, F. S. Shana¹, M. M. Musthafa¹, Shaima Akbar¹, Vafiya. T¹, Akhil Ramesh¹, Nived. K¹, Midhun. C. V¹, P. Sugathan², K. S. Golda², N. Saneesh², Mohit Kumar² and Manoj K. Sharma³

¹Department of Physics, University of Calicut, Malappuram 673635, India

²Inter-University Accelerator Center, New Delhi 110067, India

³Department of Physics, University of Lucknow, Lucknow 226007, India

Pre-equilibrium emission has been identified as a prominent nuclear reaction mechanism in the energy region of the order of 10 MeV/nucleon and above [1,2]. Pre-equilibrium emissions are characterized by the forward peaked angular distribution of emitted particles, energy spectrum shifted to higher mean energies and slowly descending tails of excitation function. The pre-equilibrium effects are evident in both particle emission and fission reactions [3]. Since the pre-equilibrium mechanism involves a lesser number of nucleon-nucleon interactions and particles/clusters emitted before the equilibration of the compound nucleus the outgoing particles carry larger energy and angular momentum. Further, as the outgoing particles carry larger energy the energy available for successive emissions will be reduced leading to a reduction in the multiplicity of emissions. This will affect the yield of the residual nucleus corresponding to each channel, the number of emitted particles, and the energetics of the outgoing particles. This is important in the application of nuclear data like production of radioactive isotopes, hadron therapy like proton therapy, neutron therapy,

5. RESEARCH ACTIVITIES

alpha therapy and carbon therapy, material modification, and design of structural materials for fusion and fission reactors, etc.

Various models based on semi-classical statistical model approaches and quantum mechanical approaches have been developed for explaining the pre-equilibrium emission mechanism. However, their predictivity is to be limited for a particular set of data, say light charged particles induced reactions, neutron induced reactions, etc. that is true over very limited energy intervals [1,4]. Further, for each reaction system, one has to optimize the nuclear parameters to reproduce the experimental data for each case. This loses the universality of the models. Comprehensive theoretical modeling, that can reproduce the experimental data covering a wide range of energies and masses, is yet to be evolved. More recently attempt has been focused to generate a uniform nuclear reaction model with a unique global set of parameters that can generate nuclear reaction data over a wide range of interests. There is a good number of data on excitation functions for the light-charged particle induced reactions at low and medium energies. However, there is a lack of sufficient data for the heavy-ion induced reactions. Heavy-ion reactions are more complex processes than light-ion reactions, that occur as a result of the relatively large number of nucleons involved and a large amount of angular momentum transfer that occurs between the projectile and the target nucleus [5].

The modern carbon ion therapy uses high energy ^{12}C beam for medical therapy and the design and operation of such accelerator facility require accurate knowledge on neutron shielding due to background neutrons produced by beam hitting on surfaces. The present work is proposed to study measurement of neutron yield from targets of ^{56}Fe and ^{93}Nb when bombarded by ^{12}C . The chosen reaction is important to understand the production of neutrons from Fe and Nb are two prominent materials in building heavy ion accelerator components. The new data are useful to the application of accelerator shielding design. The data is of significant interest in reactor physics also. There are finite probability of producing carbon ions in fission reactors as a result of ternary fission [6,7] and hence study of secondary neutron generation by interaction of ^{12}C is very significant here.

One ^{nat}Fe target foil of thickness $\sim 2.755 \text{ mg/cm}^2$ and two ^{93}Nb target foils of thickness $\sim 2.790 \text{ mg/cm}^2$ and $\sim 194.540 \text{ mg/cm}^2$ are prepared by rolling. All the three target foils and one blank target holder were fixed to the target ladder placed inside the high vacuum ($\sim 10^{-6}$ torr) National Array of Neutron Detectors (NAND) chamber. Irradiation was performed in the direction perpendicular to the sample surface. The ion beam was focused to a spot of $\sim 5 \text{ mm}$ diameter using the quartz placed in the target ladder. The foils were irradiated with 15UD Pelletron and LINAC accelerators and energy-angle distribution of neutrons is measured by time of flight using the large number of neutron detectors (100) distributed at different angles in NAND. Carbon beams with energies ranging from 125 MeV to 70 MeV were used for irradiation at a current of $\sim 1.5 \text{ pA}$. To compensate for background radiation, a blank run was conducted for each energy. Currently, analysis is ongoing to explore the impact of pre-equilibrium neutron emission in ^{12}C induced reactions in both ^{nat}Fe and ^{93}Nb targets.

References:

1. T. Otsuka, K. Harada, Phys. Lett. B **121**, 106 (1983).
2. B.P. Singh, et al., Nucl. Instrum. Methods Phys. Res. A **562**, 717 (2006).
3. T. Kawano, et al., Phys. Rev. C **63**, 601 (2001).
4. D. Singh, et al., Indian J. Pure Appl. Phys. **57**, 580 (2019).
5. M. Blann, Nucl. Phys. A **235**, 211 (1974).
6. G. M. Ter-Akopian, et al., Phys. At. Nucl. **67**, 1860 (2004).
7. A. V. Daniel, et al., Phys. Rev. C **69**, 041305 (2004).

5.1.12 Study of fission dynamics for the reactions $^{30}\text{Si}+^{194,198}\text{Pt}$

S. Ramakrishna Reddy¹, S. K. Duggi¹, K. Prameela¹, N. Saneesh², Mohit Kumar², Avitesh Agrawal³, Ashna B.⁴, Lakhyajit Sarma⁵, Raghav Agrawal⁶, Rishab Prajapati², E. Prasad⁴, A. Jhingan², K. S. Golda², P. Sugathan², S. Appannababu¹ and P. V. Madhusudhana Rao¹

¹Department of Nuclear Physics, Andhra University, Visakhapatnam 530003, India

²Inter-University Accelerator Centre, Aruna Asaf Ali Marg, New Delhi 110067, India

³Department of Physics and Astrophysics, Central University of Haryana, Mahendergarh 123031, India

⁴Department of Physics, Central University of Kerala, Kasaragod 671316, India

⁵Department of Physics, Gauhati University, Guwahati 781014, India

⁶Department of Physics, Panjab University, Chandigarh 160014, India

Recently, there has been a lot of interest in the study of fusion-fission dynamics, in order to understand the influence of the shell structure of the fissioning nucleus and nascent fragments at low excitation energies. Further, at these energies, several reports indicate the existence of multimodal fission [1]. In order to

investigate the impact of shell structure on fission dynamics, we performed an experiment to measure the mass and total kinetic energy (TKE) distributions as well as neutron multiplicities for the reactions $^{30}\text{Si}+^{194,198}\text{Pt}$.

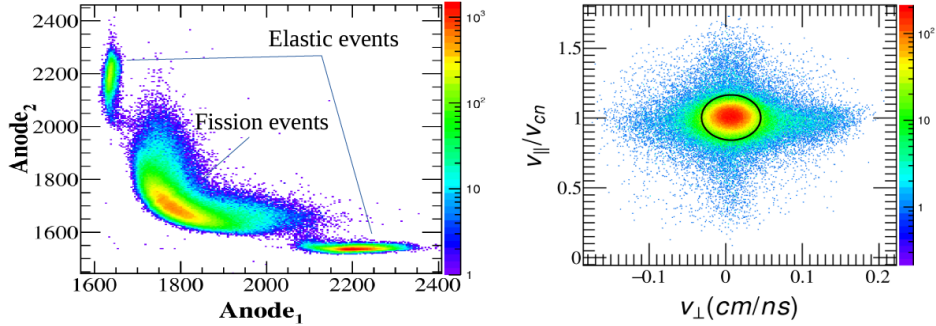


Figure 5.10: Two-dimensional correlation plot between anode signals from both the MWPCs (left) and two-dimensional plot between velocity components of the fission fragments (right) for the reaction $^{30}\text{Si}+^{198}\text{Pt}$ at $E_{\text{lab}} = 154$ MeV.

The experiment was performed at the 15UD Pelletron-LINAC facility of IUAC. A pulsed beam of ^{30}Si (pulse width ~ 1 ns and pulse separation of 250 ns) was bombarded on ^{194}Pt (thickness $\sim 150\mu\text{g}/\text{cm}^2$) and ^{198}Pt ($\sim 200\mu\text{g}/\text{cm}^2$) targets with beam energy (E_{lab}) ranging from 135 to 208 MeV. Sixteen BC501A organic scintillator detectors, placed at different polar and azimuthal angles in a geodesic dome structure of the National Array of Neutron Detectors (NAND) [2], were used for detection of neutrons. Each detector was situated at a distance of 175 cm from the target. Fission fragments were detected in coincidence by using two large area (20 cm \times 10 cm) position sensitive Multi-Wire Proportional Counters (MWPCs), placed at a folding angle of 140° with respect to the beam direction. The online data acquisition was performed with the NiasMars (Multi parameter Acquisition Root-based Storage) software.

The timing correlation spectrum of the two MWPCs allows for a clear distinction of the fission fragments from other elastic or quasielastic events, as shown in the left panel of Fig. 5.10. A typical two-dimensional plot between v_{\perp} versus $v_{\parallel}/v_{\text{cn}}$ is shown in the right panel of Fig. 5.10 for $E_{\text{lab}} = 154$ MeV, in which majority of the events were observed at 0 and 1. The events inside the circle were analysed to derive the mass and TKE distributions.

References:

1. K. -H. Schmidt *et al.*, Nucl. Phys. A **665**, 221 (2000).
2. P. Sugathan *et al.*, Pramana -J. Phys. **83**, 807 (2014).

5.1.13 Fission mass distribution studies for the reaction $^{30}\text{Si}+^{176}\text{Yb}$ and $^{14}\text{N}+^{193}\text{Ir}$ populating compound nuclei $^{206,207}\text{Po}$

Lakhyajit Sarma¹, K. Kalita¹, Harun Al Rashid^{1,2}, Amar Das^{1,3}, Nabendu Kumar Deb⁴, M. Bhuyan⁵, Taniya M. Sonowal¹, Gyandeep Narzary¹, Rayees Ahmad Yatoo⁶, S. Ramakrishna Reddy⁷, Avitesh Agrawal⁸, A. Jhingan⁹, K. S. Golda⁹, N. Saneesh⁹, M. Kumar⁹ and P. Sugathan⁹

¹Department of Physics, Gauhati University, Guwahati 781014, Assam, India

²Department of Physics, BBK College, Nagaon, Barpeta 781311, Assam, India

³Department of Physics, Suren Das College, Hajo 781102, Assam, India

⁴Department of Physics, Kamrup College, Chamata, Nalbari 781306, Assam, India

⁵Department of Physics, Rangia College, Rangia 781354, Assam, India

⁶School of Physics & Materials Science, Thapar Institute of Engineering & Technology, Patiala 147004, India

⁷Department of Nuclear Physics, Andhra University, Visakhapatnam 530003, India

⁸Department of Physics & Astrophysics, Central University of Haryana, Mahendergarh 123029, India

⁹Inter-university Accelerator Centre, Aruna Asaf Ali Marg, New Delhi 110067, India

To disentangle the CN fission from NCN fission processes, study of fission fragments (FFs) mass-angle correlation and the width of the fragments mass distribution have extensively used, utilizing one or more entrance channel parameters [1]. To understand the fission dynamics in the pre-actinide region, we populate $^{206,207}\text{Po}$ via two different entrance channels, $^{30}\text{Si}+^{176}\text{Yb}$ and $^{14}\text{N}+^{193}\text{Ir}$ respectively. The experiments were performed at IUAC, New Delhi with 15 UD pelletron accelerator using NAND facility. Pure enriched isotopic targets of ^{176}Yb [2] and ^{193}Ir were fabricated at the target laboratory of IUAC for performing the

5. RESEARCH ACTIVITIES

experiment. Two larger area MWPCs (20 *10 cm²) were mounted at the folding angles to collect the fission fragments in coincidence. The fission events are separated from elastic events from the timing correlation of the MWPCS by putting a gate as shown in Fig. 1 (a). For the analysis of the data, time and position calibration were done and from the calibrated timing and position information, folding angle and the velocities of the fission fragments were reconstructed. The fragments folding angle and velocity distributions are shown in Fig. 1 (b) and Fig. 1 (c), respectively.

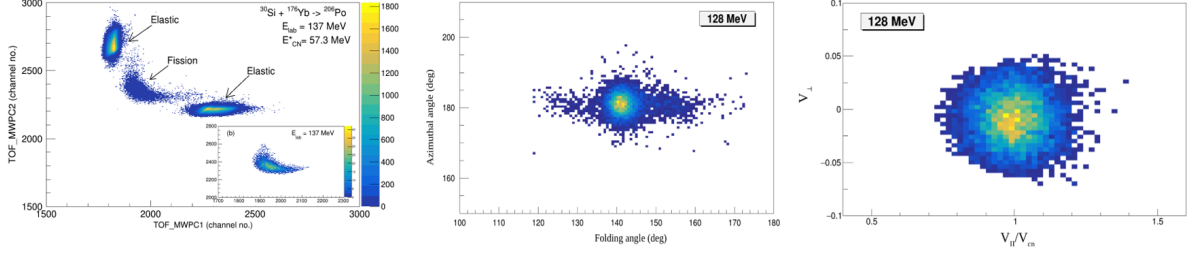


Figure 5.11: (a) TOF correlation between MWPC1 and MWPC2, (b) folding angle distribution of the FFs and (c) Velocity distribution of the FFs for the reaction $^{30}\text{Si} + ^{176}\text{Yb}$ at $E_{\text{lab}} = 128 \text{ MeV}$.

After reconstruction of the velocity components in the laboratory frame, mass of the FFs were calculated as shown in the Fig. 2 [3]. The mass distribution at the studied energy range is found to be symmetric (peaked at $A_{\text{cn}}/2$, where A_{cn} is the compound nucleus mass) and fitted with a single Gaussian function to extract the width of the mass distribution (m). The m values for the reaction $^{30}\text{Si} + ^{176}\text{Yb}$ is higher than that of the statistical model calculation, which may be due to the presence of quasifission. The present result is consistent with the earlier findings [4] of the similar nearby systems. Moreover, effect of orientation dependent quasifission is also observed at below barrier energies, where magnitude of the m abruptly increases. The analysis of the $^{14}\text{N} + ^{193}\text{Ir}$ system are in progress. As the two reactions under study have different entrance channel properties and populated with around similar excitation energies, The dynamical evolution of the composite system after capture can be compared to understand the onset quasifission and the influence of entrance channel parameters on compound nucleus and non-compound nucleus fission.

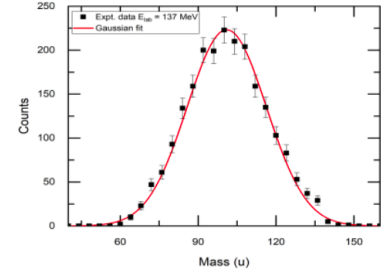


Figure 5.12: FF mass distribution for the reaction $^{30}\text{Si} + ^{176}\text{Yb}$ at $E_{\text{lab}} = 137 \text{ MeV}$.

References:

1. T. K. Ghosh *et al.*, Phys. Rev. C **79**, 054607 (2009).
2. L. Sarma *et al.*, Vacuum **224**, 113131 (2024).
3. D. J. Hinde *et al.*, Phys. Rev. C **53**, 1290 (1996).
4. R. Rafiei *et al.*, Phys. Rev. C **77**, 024606 (2008).

5.1.14 Transfer reaction studies of $^{10,11}\text{B} + ^{40}\text{Ca}$ at 50 MeV using GPSC facility

Harun Al Rashid^{1,2}, K. Kalita¹, Lakhyajit Sarma¹, Amar Das^{1,3}, Nabendu K. Deb⁴, P. Sugathan⁵, K. S. Golda⁵, A. Jhingan⁵, N. Saneesh⁵, Mohit Kumar⁵, Anamika Parihari⁶, Honey Arora⁷, J. J. Das⁸ and B. J. Roy⁹

¹Department of Physics, Gauhati University, Guwahati 781014, India

²Department of Physics, BBK College, Nagaon 781311, India

³Department of Physics, Suren Das College, Hajo 781102, India

⁴Department of Physics, Kamrup College, Chamata 781306, Assam, India

⁵Inter-University Accelerator Centre, New Delhi 110067, India

⁶Department of Physics, Rajdhani College, University of Delhi, Delhi 110015, India

⁷Department of Physics, Central Michigan University, Mt. Pleasant, Michigan, USA

⁸Department of Physics, Cotton University, Guwahati 781001, Assam, India

⁹Nuclear Physics Division, Bhabha Atomic Research Centre, Mumbai 400085, India

In order to perform a scattering experiment at the General Purpose Scattering Chamber (GPSC), IUAC to study elastic and transfer reactions for the systems $^{10,11}\text{B} + ^{40}\text{Ca}$, we fabricated carbon backed CaF_2 films of thickness $272.5 \mu\text{g}/\text{cm}^2$ at the IUAC Target Laboratory [1]. The experiment was carried out at laboratory energy of 50 MeV for both the ion beams. Four $\Delta E - E$ silicon detectors of thickness ranging from 15 - 40 μm for ΔE type and 300 - 2000 μm for E type were mounted on the two movable arms of the chamber.

Two monitors were also placed at 10° on the either side of the beam direction. Data were collected using the NIAS-MARS (Multi-parameter Acquisition with Root base Storage) software.

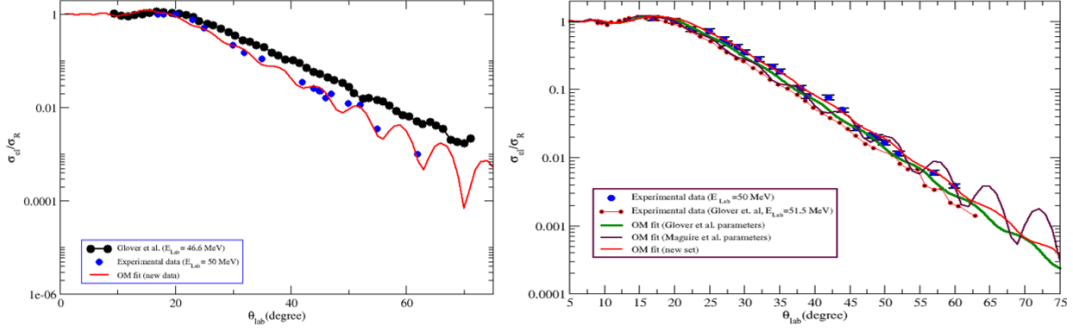


Figure 5.13: Ratio of elastic to Rutherford cross section for $^{10}\text{B}+^{40}\text{Ca}$ (left) and $^{11}\text{B}+^{40}\text{Ca}$ (right) at $E_{\text{lab}} = 50$ MeV.

Well separated transfer bands along with elastic peaks were observed for $^{10,11}\text{B}+^{40}\text{Ca}$ reactions. From our data, we have seen multi-nucleon transfer channels such as stripping reactions in $^{10}\text{B}+^{40}\text{Ca}$ and both pickup and stripping channels have been observed in $^{11}\text{B}+^{40}\text{Ca}$. Optical model analysis has been carried out for both the systems in the framework of Wood-Saxon potential. Theoretical calculations are carried out using the code FRESKO. New sets of optical model parameters are extracted for both systems and they are compared with the data obtained by Glover *et al.* [2] as shown in Fig. 5.13. Further analysis of data is going on for both the systems.

References:

1. H. A. Rashid, L. Sarma, K. Kalita *et al.*, Nucl. Instrum. Methods A **1057**, 168775 (2023).
2. C. W. Glover, K. W. Kemper, L. A. Parks *et al.*, Nucl. Phys. A **337**, 520 (1980).

5.1.15 Investigation of mass distribution of the $^{28}\text{Si}+^{158}\text{Gd}$ system: Role of shell effects

Pavneet Kaur¹, Moumita Maiti¹, Rishabh Kumar¹, Ankur Singh¹, Himanshu Sharma¹, Yasir Arafat¹, N. Saneesh², A. Parihari³, M. Kumar², K. S. Golda², A. Jhingan² and P. Sugathan²

¹Department of Physics, Indian Institute of Technology Roorkee, Roorkee 247667, Uttarakhand, India

²Inter-University Accelerator Centre, Aruna Asaf Ali Marg, New Delhi 110067, India

³Department of Physics and Astrophysics, University of Delhi, Delhi 110007, India

An experiment was performed in order to investigate the fission fragment mass distributions (FFMD) and underlying fission fragment properties of the ^{186}Pt compound nucleus. The pulsed beam, with a pulse separation of 250 ns, was bombarded on the 97% enriched $^{158}\text{Gd}_2\text{O}_3$ target of thickness $\approx 110 \mu\text{g}/\text{cm}^2$ with carbon backing of $\approx 35 \mu\text{g}/\text{cm}^2$. To detect the coincident fission fragments, two identical position-sensitive multi-wire proportional counters (MWPCs) having dimensions $20 \text{ cm} \times 10 \text{ cm}$ were positioned symmetrically at $\pm 70^\circ$ with respect to the beam direction and 25 cm apart from the target in the scattering chamber of the National Array of Neutron Detectors (NAND) facility. The anodes of both MWPCs delivered the fission fragment's time-of-flight (TOF) information, whereas the position information was obtained through the delay-line readout of the wire grids. The VME-based data acquisition system was used to acquire the list-mode data. The logical AND of the radiofrequency (RF) pulse of the beam with the OR output of the TOF signals from both the MWPCs served as the trigger for the data acquisition system. Fig. 5.14 represents the two-dimensional correlated TOF signals, TOF-1 and TOF-2, from MWPC-1 and MWPC-2, respectively. This TOF information provided by

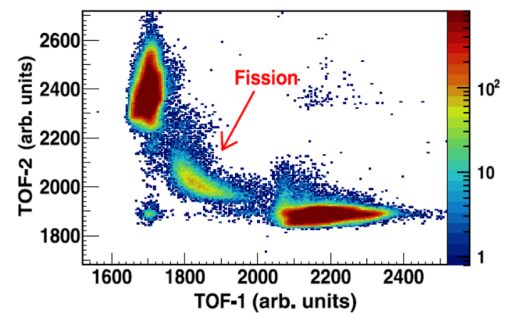


Figure 5.14: Scatter plot of TOF-1 versus TOF-2 at $E^* = 51.3$ MeV, where the arrow refers to the fission events (middle patch), which are well separated from the elastic or quasielastic events (extreme patches).

5. RESEARCH ACTIVITIES

the MWPCs was utilized to get the velocities, which were further used to estimate the fission fragment mass and kinetic energy distributions.

Consequently, the FFMD at different excitation energy (E^*) was found to be broad and flat-topped, indicating the existence of the admixture of symmetric and asymmetric fission modes. In view of this, a comparative analysis was carried out to test the closer fitting to the experimental mass distribution among the one-Gaussian (one symmetric mode), two-Gaussian (one asymmetric mode), and three-Gaussian (one symmetric and one asymmetric mode). The one-Gaussian fit failed to satisfy the experimental mass distributions, whereas the two- and three-Gaussian fits efficiently reproduced the distributions, signifying the crucial role of the quadrupole deformed ($Z \approx 34, 36, 42, 44$ and 46) shell gaps in deciding the fate of the compound nucleus. Moreover, the experimental mass distributions and fragment properties were also compared with the GEneral Fission (GEF) model predictions in order to test this model code's reliability in the sub-lead region. Although the GEF model failed to predict the structure of the experimental mass distributions for all three E^* s (64.1, 51.3 and 47.0 MeV), it grossly predicted the fragment properties of the present system. No signature of the quasifission process was observed. Also, the symmetric contribution estimated for ^{186}Pt was compared with GEF model outcomes. A good agreement between the GEF code-derived symmetric contribution and the experimental ones was observed for each energy [1].

References:

1. Pavneet Kaur, Moumita Maiti, R. Kumar, A. Singh *et al.*, Phys. Rev. C **110**, 034613 (2024).

5.1.16 Study of entrance channel effect on shell closure in fission dynamics

Punit Dubey¹, Mahesh Choudhary¹, Namrata Singh¹, Mahima Upadhyay¹, Shweta Singh¹, Utkarsha Mishra¹, Sriya Paul¹, N. Saneesh², Mohit Kumar², Rishabh Prajapati², K. S. Golda², Akhil Jhingan², P. Sugathan², Raghav Agarwal³, Kiran³ and Ajay Kumar¹

¹Department of Physics, Banaras Hindu University, Varanasi 221005, India

²Inter-University Accelerator Centre, Aruna Asaf Ali Marg, New Delhi 110067, India

³Department of Physics, Panjab University, Chandigarh 160014, India

Nuclear fusion-fission dynamics is heavily influenced by factors such as the entrance channel mass asymmetry (α), the shell effect and the N/Z value. Researchers have conducted experimental and theoretical studies [1] to determine the influence of these characteristics on fusion-fission dynamics. We found that the most effective method for determining the relationship between these parameters in fission dynamics is to study the pre-scission neutron multiplicity (M_{pre}).

In this academic session (2023-24), we performed our experiment entitled ‘‘Study of entrance channel effect on shell closure in fission dynamics’’ utilizing the Pelletron + LINAC facility in the NAND [2] beamline in February 2024. We aimed to calculate the pre-scission neutron multiplicity and investigate the influence of the entrance channel, neutron-to-proton ratio (N/Z) and shell closure on fusion-fission dynamics. For this investigation, we selected the following reactions: $^{28}\text{Si}+^{178}\text{Hf}$ and $^{28}\text{Si}+^{186}\text{W}$.

We have completed analysis of the data and are currently engaged in theoretical study. The results obtained for one of the reactions ($^{28}\text{Si}+^{178}\text{Hf}$) are presented in Table 5.1 and Fig. 5.15.

Table 5.1: Summary of the results obtained for the reaction $^{28}\text{Si}+^{178}\text{Hf} \rightarrow ^{206}\text{Rn}^*$.

E^* (MeV)	M_{pre}	M_{post}	M_{total}	T_{pre}	T_{Tpost}
61.00	2.12±0.13	3.26±0.07	5.38±0.15	1.34±0.07	1.11±0.03
71.70	2.79±0.13	3.46±0.07	6.25±0.15	1.46±0.06	1.17±0.03
79.00	3.15±0.16	3.74±0.10	6.89±0.19	1.47±0.06	1.26±0.03
90.00	3.31±0.18	3.84±0.11	7.15±0.21	1.56±0.07	1.28±0.04

We have received a high-quality beam throughout the experiment. Also, we have received all necessary assistance from the IUAC accelerator personnel. We express our sincere gratitude for the support provided by IUAC accelerator staff during the experiment. We are also thankful to the Target Development laboratory of IUAC for providing us with the enriched targets (^{178}Hf and ^{186}W) of required thickness.

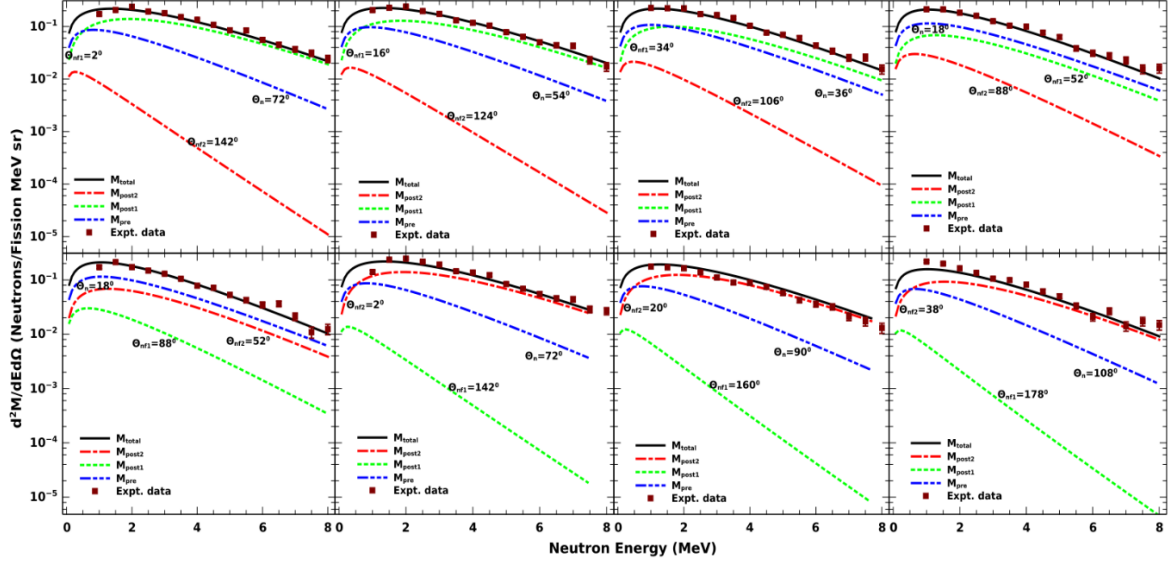


Figure 5.15: Calculated double differential neutron spectra with respect to neutron energy in the range of 1-8 MeV for the reaction $^{28}\text{Si}+^{178}\text{Hf} \rightarrow ^{206}\text{Rn}^*$ at $E_{\text{lab}} = 167$ MeV.

References:

1. Rohit Sandal *et al.*, Phys. Rev. C **100**, 014614 (2019).
2. N. Saneesh *et al.*, Nucl. Instrum. Methods A **986**, 164754 (2021).

5.1.17 Investigation of fusion-fission dynamics of ^{192}Hg

Pavneet Kaur¹, Moumita Maiti¹, Rishabh Kumar¹, Ankur Singh¹, Himanshu Sharma¹, M. V. S. Chandrachud¹, N. Saneesh², A. Parihari³, M. Kumar², K. S. Golda², A. Jhingan² and P. Sugathan²

¹Department of Physics, Indian Institute of Technology Roorkee, Roorkee 247667, Uttarakhand, India

²Inter-University Accelerator Centre, Aruna Asaf Ali Marg, New Delhi 110067, India

³Department of Physics and Astrophysics, University of Delhi, Delhi 110007, India

The experiment was performed utilizing ^{32}S pulsed beam from the 15UD Pelletron of IUAC. The beam with energies varying from $E_{\text{lab}} = 134 - 156$ MeV was bombarded on a ^{160}Gd target of thickness $\approx 80 \mu\text{g}/\text{cm}^2$ with carbon backing of thickness $\approx 20 \mu\text{g}/\text{cm}^2$. In order to detect the coincident fission fragments (FFs), two position-sensitive MWPCs having dimensions $16 \text{ cm} \times 11 \text{ cm}$ were employed in the scattering chamber of the NAND facility. The MWPC detectors were placed at a 134° folding angle and their distance from the target center was about 25 cm. The isobutane gas pressure within the detectors was maintained at 4.5 mbar. Moreover, two silicon surface barrier detectors for normalizing the beam flux were placed at $\pm 12^\circ$ with respect to the beam direction. The kinematical coincidence method was employed to derive the mass ratio distribution from the obtained velocities in the center of the mass frame. Fig. 5.16 depicts the two-dimensional plot of time-of-flight (TOF) signals, TOF 1 and TOF 2 from MWPC1 and MWPC2, respectively. The experimental FF mass distributions were found to be broad and flat-topped, which did not satisfactorily fit the single Gaussian for each studied E^* . This observation gave a signature of the presence of asymmetric mode along with the symmetric mode in the distributions. The 3-Gaussian fit reproduced the experimental mass distributions well. Further, the experimental and the-

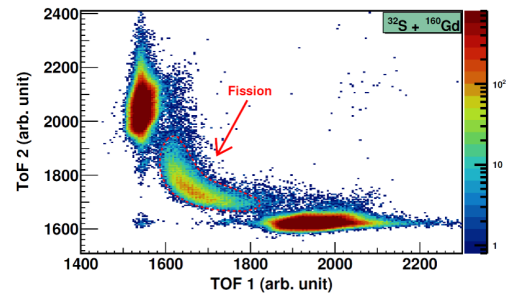


Figure 5.16: Scatter plot of TOF 1 versus TOF 2 corresponding to $^{32}\text{S}+^{160}\text{Gd}$ system, where the arrow is referring to the fission events (middle patch shown by graphical cut), which are well separated from the elastic or quasi-elastic events (extreme patches).

5. RESEARCH ACTIVITIES

oretical (GEF-predicted) mass distributions and corresponding fragment properties, *i.e.*, $Z_{l,h}$ values (mean proton values corresponding to light and heavy fragments), were compared. As a result, the GEF-predicted $Z_{l,h}$ values were found to agree with the experimental results, which reside in the vicinity of the quadrupole-deformed shell gaps ($Z = 34, 36, 42, 44$), with a deviation of only 1-2 proton number (as evident in Table 5.2). Also, the symmetric fission contributions were found to increase with rising E^* , reflecting the successive diminishing of the shell effects. A partial analysis has been carried out for ^{192}Hg [1], and a detailed analysis is being processed.

Table 5.2: The number of protons present in the light and heavy fission fragments (Z_l, Z_h) corresponding to the asymmetric fission mode, obtained from the 3-Gaussian fit of the experimental mass distributions and GEF predictions for all the three excitation energies.

E^* (MeV)	Experimental Z_l	Experimental Z_h	GEF-predicted Z_l	GEF-predicted Z_h
55.1	35.3 (0.1)	44.7 (0.1)	36.0	43.8
62.6	34.0 (0.2)	45.9 (0.2)	35.7	43.9
67.6	33.5 (0.1)	46.5 (0.1)	35.8	43.6

References:

1. Pavneet Kaur, Moumita Maiti, R. Kumar, A. Singh *et al.*, Proc. DAE Nucl. Phys. Symp. **67**, 405 (2023).

5.1.18 Reaction measurements in the interactions of ^{19}F with $^{92,100}\text{Mo}$ using the GPSC

Beant Kaur Guron¹, Sunil Kalkal¹, Rayees Ahmad Yatoo¹, Akhil Jhingan², Gobind Ram³, E. Prasad⁴, Ashna B.⁴, Anjali Merin⁴, Anamika Parahari⁵, Golda K.S.², P. Sugathan², Mohit Kumar² and N. Saneesh²

¹Department of Physics & Material Science, Thapar Institute of Engineering & Technology, Patiala 147004, India

²Inter-University Accelerator Centre, New Delhi 110067, India

³Department of Physics, University of Lucknow, Uttar Pradesh 226007, India

⁴Department of Physics, Central University of Kerala, Kasaragod, Kerala 671320 India

⁵Department of Physics, Rajdhani College, University of Delhi, New Delhi 110015, India

The reaction dynamics of heavy ion collisions at the bombarding energies near the Coulomb barrier are governed by the coupling of various reaction channels, which include inelastic excitations, nuclear deformations, particle transfer channels etc. It is important to understand the underlying reaction mechanism of these channels. To understand the interaction between the projectile and target nucleus, the elastic cross-section measurements proves to be fruitful [1]. Transfer angular distribution measurements help us understand the dynamics of nuclear transfer reactions and the angular dependence of the transfer products [2]. In the present study, the elastic and transfer measurements were performed in reaction of ^{19}F with $^{92,100}\text{Mo}$ near the Coulomb barrier. The elastic as well as transfer angular distributions have been extracted from the experimental data.

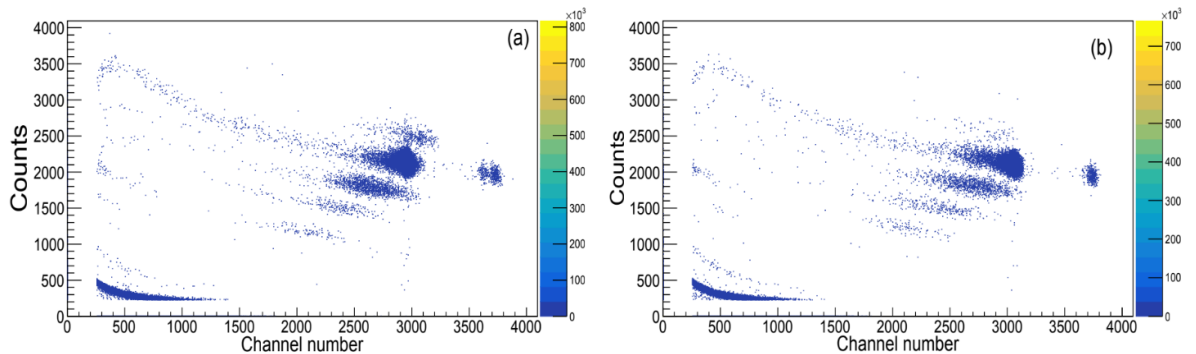


Figure 5.17: $\Delta E - E$ spectra of (a) $^{19}\text{F}+^{92}\text{Mo}$ and (b) $^{19}\text{F}+^{100}\text{Mo}$ systems at $E_{\text{lab}} = 66$ MeV and $\theta_{\text{lab}} = 80^\circ$.

The transfer excitation function measurements were performed in laboratory energy range of 42–72 MeV with 1.5 MeV steps in the below barrier region and 2 MeV steps in the above barrier region. Two silicon monitor detectors were kept at 10° with respect to the beam axis for beam monitoring and normalization of cross sections. Six hybrid ($\Delta E - E$) detectors with angular spacing of 20° were used on one arm of the General Purpose Scattering Chamber (GPSC) to cover the angular range. Four $\Delta E - E$ detectors were placed at the back angles ($\sim 173^\circ$) to record the back-scattered quasielastic (QEL) events. Each $\Delta E - E$ detector was a combination of a gas detector (ΔE) consisting iso-butane operating at 20–120 mbar pressure and a E silicon detector with thickness $\sim 300 \mu\text{m}$. The $\Delta E - E$ spectra of $^{19}\text{F} + ^{92,100}\text{Mo}$ systems at $E_{\text{lab}} = 66$ MeV depicting the elastic, inelastic and different proton transfer channels are shown in Fig. 5.17.

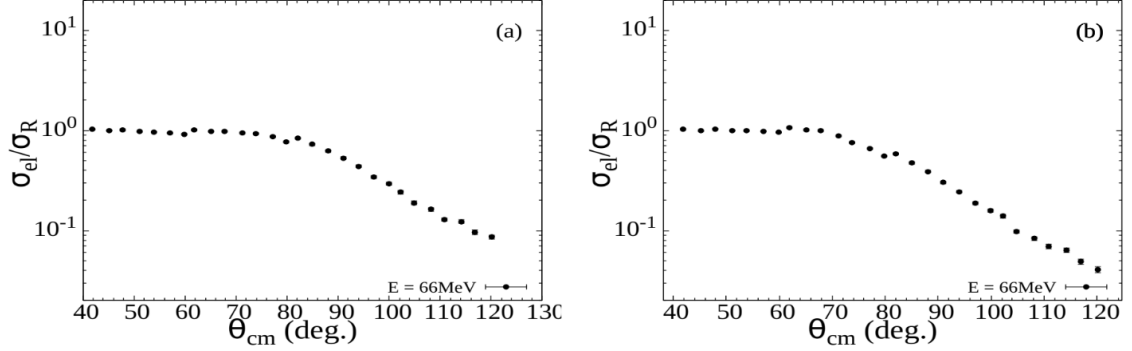


Figure 5.18: Elastic angular distribution for (a) $^{19}\text{F} + ^{92}\text{Mo}$ and (b) $^{19}\text{F} + ^{100}\text{Mo}$ measured at $E_{\text{lab}} = 66$ MeV. Statistical errors have been taken into consideration.

The experimental data were analyzed to extract the elastic and transfer angular distributions at $E_{\text{lab}} = 55.5, 60, 66$ and 72 MeV. The elastic cross sections extracted in reactions of ^{19}F with $^{92,100}\text{Mo}$ systems at $E_{\text{lab}} = 66$ MeV are shown in Fig. 5.18.

The transfer angular distributions were obtained using the expression

$$\left[\left(\frac{d\sigma}{d\Omega} \right)_{\text{tr}} \right]_{\text{tel}} = \frac{(Y_{\text{tel}})_{\text{tr}}}{(Y_{\text{M}})_{\text{R}}} \left[\left(\frac{d\sigma}{d\Omega} \right)_{\text{R}} \right]_{\text{M}} \frac{\Delta\Omega_{\text{M}}}{\Delta\Omega_{\text{tel}}} \quad (5.2)$$

where Y_{tel} is the yield of the transfer events at different angles in the telescopic detectors, Y_{M} is the geometric mean of the yield obtained from the two monitor detectors. $\frac{\Delta\Omega_{\text{M}}}{\Delta\Omega_{\text{tel}}}$ is the ratio of the solid angles of monitor and telescopic detector, respectively. To precisely determine the solid angle subtended by the monitors and back angle detector, a low energy run at 42 MeV was taken during the experiment by using ^{197}Au as the target. As this beam energy is well below the Coulomb barrier, elastic scattering at this bombarding energy is expected to be governed by Rutherford scattering. The transfer angular distribution results at $E_{\text{lab}} = 66$ MeV are shown in Fig. 5.19. The analysis using coupled reaction channel (CRC) theoretical model is under progress.

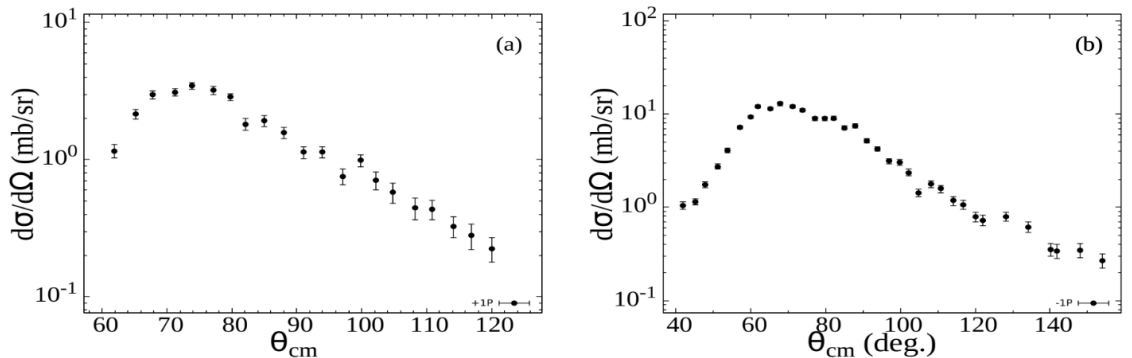


Figure 5.19: Transfer angular distributions for (a) one proton pick-up channel for $^{19}\text{F} + ^{92}\text{Mo}$ and (b) one proton stripping channel of $^{19}\text{F} + ^{100}\text{Mo}$ measured at $E_{\text{lab}} = 66$ MeV.

5. RESEARCH ACTIVITIES

References:

1. L. F. Canto *et al.*, *Eur. Phys. J. A* **56**, 1 (2020).
2. Z. Liao *et al.*, arXiv preprint arXiv:2407.05395 (2024).
3. A. Jhingan *et al.*, *Nucl. Instrum. Methods A* **903**, 326 (2018).
4. C. Joshi *et al.*, *Proc. DAE Int. Symp. Nucl. Phys.* **63**, 1210 (2018).

5.2 Materials science

A. Tripathi

The materials science facilities support various research programmes of users from universities and institutions from all over India and provide critical support on priority to programmes of national significance from organizations such as the ISRO. This year, a total of 28 user experiments spread over 109 shifts took place. Efforts continued this year to complete the projects of students in the final years of their Ph.D.s and most of the urgent requests were scheduled. A total of 25 experiments involving research scholars spanning more than 83 shifts were conducted. As for last few years, there was no beam time loss due to any major facility break down in the two beamlines for materials science experiments. The swift heavy ion (SHI) irradiation experiments mostly utilize irradiation facilities in materials science beamlines in Beam Hall I. In this year, 24 user experiments spread over 85 shifts took place in this chamber. There was one special run of 9 shifts from the ISRO performed in the GPSC for low fluence irradiation to study single event upset. High temperature irradiation experiments were done in materials science beamline in Beam Hall II and three high temperature irradiations at ~ 1000 K took place utilizing a total of 15 shifts.

Besides irradiation facilities, materials science group is also providing support to users with many materials synthesis and characterization facilities and this year more than six hundred samples were characterized by the users. The synthesis facilities for sample preparation were also utilized for preparing around 220 samples. The materials science research programmes utilize various irradiation facilities in Pelletron beamlines, LEIBF, NIBF, Table-top accelerators in a wide range of energies varying from tens of keV to hundreds of MeV. There were more than 70 publications in reputed journals such as ACS Omega, Applied Surface Science, Applied Physics A, Journal of Physics D, Journal of Physical Chemistry C, Physica B, Ceramic International, Radiation Physics and Chemistry, Journal of Alloys and Compounds etc. A list of publications is given in Chapter 6. This year, there were many interesting results in the various areas of research including those on nanocomposites, track formation, DFT calculations, velocity and synergetic effects, band gap tuning etc. and some of these are highlighted below.

Ion beams from the Pelletron are widely used for user experiments in the two Beam Halls. WC films prepared using RF sputtering technique were irradiated with 100 MeV Ag^{8+} ions to study the response of this material in extreme radiation environments and GAXRD, FE-SEM, HRTEM and Raman spectroscopy studies revealed grain size reduction accompanied with reduced crystallinity with increasing ion fluence without track formation. MoSe_2 / CNT nanocomposite was studied to understand impact of carbon nanotubes (CNTs) on the structural, morphological and thermoelectric properties of molybdenum diselenide (MoSe_2) and studies using XRD, Raman, EDS, SEM, TEM showed that the layers of MoSe_2 surrounded the CNTs and carrier transport occurred from MoSe_2 to CNTs. The results of this study demonstrated the potential of MoSe_2 / CNT nanocomposites for use in thermoelectric applications. Effects of rapid thermal annealing (RTA) on 100 keV Cu implanted germanium (Ge) thin films were studied using XRD and Raman showing crystallization of amorphized implanted films with crystallite size increasing from 10.5 to 11.6 nm. The broad PL emission in the visible region signifies the possible use of Ge for optoelectronic applications. The band gap of a few-layer MoS_2 has been marginally modified (20 meV) by 100 MeV Ni ions having a Se of 11.3 keV/nm, which has been observed due to strain induced by ion irradiation. The band gaps for the MoSe_2 samples irradiated by 60 and 150 MeV Ni ions, which have the same Se, indicates that the velocity effect is not playing any role in band gap modification. The band gaps of 1L- MoSe_2 and 1L- WSe_2 are 1.49 eV and 1.66 eV with direct nature, respectively. However, it is shown that when the heterostructure of MoSe_2 / WSe_2 was formed, the band gap was suppressed to 1.42 eV while keeping the direct nature. Furthermore, changing the value of x (from 1.00 to 0.00) in $\text{Mo}_x\text{W}_{(1-x)}\text{Se}_2$ provides a band gap range of 1.49–1.66 eV. On the other hand, the band structure of the 1L- MoSe_2 , 1L- WSe_2 and the MoSe_2 / WSe_2 heterostructure under the biaxial strain shows that the variation of the band gap has direct, indirect, and metallic nature showing possibilities for band gap tuning in these materials.

The effect of swift heavy ion (SHI) irradiation on exfoliated WSe₂ has been studied using 60 MeV N⁵⁺ ions, with fluences varying from 5×10^{11} to 5×10^{13} ions/cm². The study found that introducing defect states in the forbidden region finely tunes the WSe₂ bandgap to 0.37 eV along the K- Γ direction of the Brillouin zone (BZ). Development of droplet-based triboelectric nanogenerators was observed with PVDF-HFP-coated WS₂ nanosheets. The DTENG output is found to vary with the quality of water collected from different resources, which indicates the potential applicability of the system for monitoring water quality in our daily lives. Further modification of the device output will be tested upon irradiating the PVDF-HFP/WS₂ layer with swift heavy ion beams at IUAC. Monstera deliciosa-mediated single-step biosynthesis of gold nanoparticles by bottom-up approach and its nonantimicrobial properties synthesis of gold and silver nanoparticles using various novel biological sources and its characterization were carried out. Modifications in properties of titanium carbide MXene by Ag doping via ion implantation technique for quantum dot-sensitized solar cell applications, which is related to the ion implantation of transition metal (Ag) into MXene / TiO₂ films by utilizing low energy at different fluences of 5×10^{12} to 5×10^{15} ions/cm², respectively. The QDSSC device irradiated with 5×10^{14} ions/cm² Ag ions exhibited the highest power conversion efficiency of 3.94%, compared to the unimplanted MXene / TiO₂-based QDSSC (2.48%), which is attributed to enhanced absorption and minimization of charge recombinations, as corroborated by photovoltaic characteristics and Nyquist plots. The various copper ion irradiation studies on PNP transistors at different biasing conditions and cryogenic and high temperature effects on NPN transistors has been studied. In addition to that, the N-channel MOSFETs irradiated with 150 MeV Fe ions have also been studied. It is shown that degradation in electrical characteristics is less for the devices irradiated at -1 V bias than at +1 V and 0 V due to the carrier injection annealing mechanism. It can be observed that the degradation in electrical parameters is greater for the devices irradiated at 410 K than at 300 K and 100 K due to the fact that the radiation-induced traps will have high thermal energy at 410 K when compared to 300 K and 100 K. Study is undertaken to evaluate the anchoring mechanism of silver ions in TiO₂ photoanodes used in DSSCs using ion beam irradiations. The impact of magnetism on enhancing efficiency in photovoltaic cells has been analyzed, as has the utilization of advanced X-ray absorption spectroscopic techniques to probe and comprehend these intricate effects. Tuning of electrical properties through field effects for manganite-based n-n junctions with the role of SHI irradiation has been studied. The modification in the electrical properties of CLS-PRI was understood at different excitation frequencies of (a) 10 K and (b) 100 K in the application of light and dark modes. The focus area is to irradiate the CLS and CGS series samples in the application of SHI irradiation using 200 MeV Ag¹⁵⁺ ions with different ion fluences. The 100 MeV ¹⁶O⁷⁺ ion beam induced significant changes in PVDF films, including increased thickness and lattice modifications. XRD analysis revealed higher dislocation density, lattice strain and reduced crystallinity with rising fluence. Synthesis and Confirmation of Ge₂Sb₂Te₅ phase in bulk and thin sputtered GST thin films of 200 nm were annealed, showing a phase transition from amorphous to fcc at 150 °C and then to hcp at 250 °C.

The 7th International Conference on Nanostructuring with Ion Beams (7th ICNIB-2023) was jointly organized by IUAC and UPES Dehradun at UPES during November 2-4, 2023. International School on Ion Beams in Materials Science (IBMS-2023) was organized at IUAC during October 28-31, 2023, the details of which can be found in Chapter 6.

5.2.1 Irradiation effects of 60 MeV N⁵⁺ ions on exfoliated WSe₂

Hemanga J. Sarmah¹, Bhupali Deka¹, Dhanjit Talukdar², F. Singh³ and D. Mohanta¹

¹Nanoscience and Soft-Matter Laboratory, Deptt. of Physics, Tezpur University, Napaam, Tezpur 784028, Assam, India

²Optoelectronics and Photonics Laboratory, Deptt. of Physics, Tezpur University, Napaam 784028, Assam, India

³Materials Science Group, Inter-University Accelerator Center, New Delhi 110067, India

Ion irradiation offers a novel approach to modify the properties of nanomaterials, paving the way for its application in specific fields [1,2]. Through this work, the effect of swift heavy ion (SHI) irradiation in WSe₂ material was studied using 60 MeV N⁵⁺ ions, with fluences varying from 5×10^{11} to 5×10^{13} ions/cm². The structural analysis showed an anomalous variation in crystallite size at higher fluences. The full width at half-maximum (FWHM) values of the (002) diffraction plane in irradiated cases were compared to the pristine material in order to quantify the level of disorder and damage induced by SHI irradiation. From Raman spectra analysis, an increase in vibrational intensity was observed after irradiation for the in-plane (E_{2g}¹) and LA modes. Atomic force microscopy (AFM) imaging revealed eight-fold increase in the root mean square (RMS) roughness from 27.2 to 212.6 nm with irradiation. The post-irradiation morphological study

5. RESEARCH ACTIVITIES

using high-resolution transmission electron microscopy (HR-TEM) imaging displays craters on the surface of the sheets. Density functional theory (DFT) calculations were used to investigate the development of vacancy clusters during high-energy irradiation [3]. The study found that introducing defect states in the forbidden region finely tunes the WSe₂ bandgap to 0.37 eV along the K- Γ direction of the Brillouin zone (BZ). Prior to irradiation experiments, as-purchased WSe₂ bulk material was exfoliated through liquid phase exfoliation (LPE) method using 1-methyl-2-pyrrolidone (NMP) as the solvent. The dried exfoliated powder was infused into teflon-based pellets of area $1.3 \times 1.3 \text{ cm}^2$ for irradiation purpose. The WSe₂ pellets were irradiated with 60 MeV N⁵⁺ ion beam using the 15 UD Pelletron tandem accelerator at IUAC. The pellets were fixed on a rectangular ladder and placed inside the high vacuum target chamber maintained at pressure $\sim 10^{-6}$ torr with current of 1 pA. The teflon-supported WSe₂ pellets were irradiated with 5×10^{11} ions/cm², 1×10^{12} ions/cm², 1×10^{13} ions/cm², and 5×10^{13} ions/cm² at normal incidence. From SRIM calculations, it is found that the electronic energy loss ($S_e \sim 167.80 \text{ eV/A}$) is dominant over its nuclear energy loss ($S_n \sim 0.108 \text{ eV/A}$) counterpart (Fig. 5.20(a)). The schematic of N⁵⁺ ion irradiation on exfoliated WSe₂ is shown in (Fig. 5.20(b)). The surface modification observed after irradiation along with sheet like morphologies of WSe₂ material is displayed in (Fig. 5.20(c-j)).

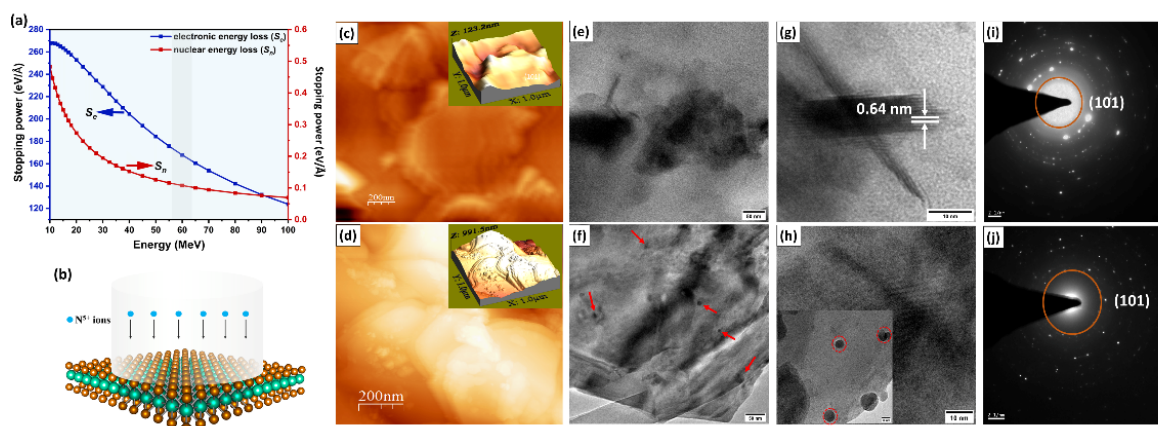


Figure 5.20: (a) SRIM calculation shows the stopping power vs. energy plot for nitrogen ion irradiation in WSe₂ material, (b) schematic illustration of the SHI irradiation in WSe₂ with N⁵⁺ ions. AFM images of 2D surface scans of (c) pristine (exfoliated WSe₂) and (d) after irradiation for fluence 5×10^{13} ions/cm², and its corresponding 3D topography are shown as an inset; HR-TEM imaging of (e,g) pristine WSe₂; (f,h) at fluence of 1×10^{13} ions/cm² at lower as well as higher magnification, note that scale bars shown are of 50 nm and 10 nm respectively (i,j) SAED pattern of pristine WSe₂ and 60 MeV N⁵⁺ ion irradiation in WSe₂ material.

References:

1. H. Vázquez, A. Kononov, A. Kyritsakis, N. Medvedev, A. Schleife and F. Djurabekova, Phys. Rev. B **103**, 224306 (2021).
2. B. Deka, D. Mohanta, V. Naik and A. Saha, Physica Status Solidi (b) **260**, 2200598 (2023).
3. A.-K. Anbalagan, F.-C. Hu, W.K. Chan, A.-C. Gandhi, S. Gupta *et al.*, ACS Nano. **17**, 6555 (2023).

5.2.2 Development of droplet-based triboelectric nanogenerators with PVDF-HFP coated WS₂ nanosheets

Madhav Barail¹, Bikash Baro¹ and Sayan Bayan¹

¹Department of Physics, Rajiv Gandhi University, Doimukh, Arunachal Pradesh 791112, India.

Harnessing mechanical energy from the surrounding environment is an excellent approach to develop self-powered gadgets. In this context, nanogenerators based on triboelectric properties have been an excellent choice for achieving self-powered systems and sensors. The triboelectric nanogenerators (TENG) operate by means of the conjugated effects of triboelectricity and charge induction phenomena (for details, see [1]). Apart from the potential sources of mechanical energy like transportation, machinery items etc. natural resources

like wind, and rainfall are regarded as excellent options for imparting mechanical energy. Thus the interaction of water drops on solid surfaces can lead development of liquid-solid TENG to harvest energy from water waves or raindrops. Over the years, suitable polymer nanocomposites have emerged as an excellent choice for active materials in energy harvesting devices (for details, see [2]). With this intention, PVDF-HFP coated WS₂ nanosheets have been exploited for the development of droplet-based TENG (DTENG) by our group. The WS₂ nanosheets have been achieved from the bulk counterpart through liquid phase exfoliation, while the composite has been obtained upon coating PVDF-HFP polymer over the nanosheets. The formation of nanosheets has been confirmed by characterization techniques like high-resolution transmission electron microscopy (HRTEM) and Raman spectroscopy. The HRTEM study reveals the interlayer spacing of 0.64 nm for the synthesized nanosheets, while the X-ray diffraction (XRD) pattern shows the formation of the hexagonal phase of WS₂ with the prominence of (002) plane. The observation of 2LA(M) mode of WS₂ at 348.17 cm⁻¹ and A_{1g} mode at ~ 419.7 cm⁻¹ in Raman spectroscopy indicates the formation of a few layered WS₂. Apart from the characteristic XRD peaks of WS₂, the existence of peaks related to α -phase and β -phases PVDF confirm the presence of the polymer and nanosheet phases in the composite sample. The DTENG has been fabricated upon attaching top and bottom electrodes on the layer of PVDF-HFP coated WS₂ nanosheets, while the output has been measured upon imparting water droplets on the device from a particular height. It has been found that the PVDF-HFP/WS₂ active layer can yield 89.5% higher output voltage than the bare PVDF-HFP layer. The observation of improvised output property has been assigned to the modification in dielectric properties and surface hydrophobicity of PVDF-HFP matrix upon the addition of WS₂. At a frequency of ~ 1MHz, the capacitance of the PVDF-HFP/WS₂ layer is ~4 times higher than that of bare PVDF-HFP and thus indicates the improvement in dielectric property which indeed helps in the retention of tribo-charges. Further contact angle measurements show a change in angle from 62° to 88° and indicate an improvement in the surface hydrophobicity PVDF-HFP layer. Again, the DTENG performance is found to be influenced by the water droplet frequency and height of impact on the DTENG surface. Finally, the DTENG output is found to vary with water quality collected from different resources and thus indicates the potential applicability of the system for monitoring water quality in our daily life. Further modification of the device output will be tested upon irradiating the PVDF-HFP/WS₂ layer with swift heavy ion beams at IUAC. It is expected that the modification in the dielectric constant of the layer upon irradiation with different fluences will lead to the modification/improvement in DTENG output.

References:

1. B. Baro, S. Khimhun, U. Das and S. Bayan, *Nano Energy* **108**, 108212 (2023).
2. D. Bhattacharya, S. Bayan, R. K. Mitra and S. K. Ray, *Nanoscale* **13**, 15819 (2021).

5.2.3 *Monstera deliciosa* mediated single step biosynthesis of gold nanoparticles by bottom-up approach and its non-antimicrobial properties

Janvi Shirsul¹, Ambuj Tripathi², Dambarudhar Mohanta³ and Balaprasad Ankamwar¹

¹Bio-Inspired Materials Research Lab, Dept. of Chemistry, Savitribai Phule Pune University, Ganeshkhind, Pune 411007, India

²Materials Science Group, Inter-University Accelerator Center, New Delhi 110067, India

³Department of Physics, Tezpur University, PO: Napaam 784028, Tezpur, Assam, India

In order to tailor the electronic properties, we have successfully reported an eco-friendly, simple, and cost-effective approach for the green biosynthesis of stable gold nanoparticles. An aqueous extract of *Monstera deliciosa* leaves was utilized to synthesize AuNPs, along with separating them at different speeds of centrifugation and further characterized them using various techniques. The UV–visible absorption spectra of AuNPs exhibited maxima bands in the range of 500–590 nm, indicating a characteristic of AuNPs. XRD analysis revealed the formation of the (111)-oriented face-centered cubic (FCC) phase of AuNPs. ATR-IR spectra showed signatures of stretching vibrations of O–H, C–H, C=C, C=O, C–O, and C–N, accompanied by CH₃ rocking vibrations present in functional groups of biomolecules. FESEM images confirmed spherical nanoparticles with an average diameter in the range of 53–66 nm and predominantly triangular morphology of synthesized AuNPs within the size range of 420–800 nm. NMR, GC–MS, and HR–MS studies showed the presence of different biomolecules, including phenols, flavonoids, and antioxidants in leaf extract, which play a crucial role of both, reducing as well as stabilizing and capping agents to form stable AuNPs by a bottom-up approach. They were then investigated for their antibacterial assay against Gram-positive (*S.*

5. RESEARCH ACTIVITIES

aureus, *B. subtilis*) and Gram-negative (*E. coli*, *P. aeruginosa*) microorganisms, along with testing of antifungal potential against various fungi (*Penicillium sp.*, *Aspergillus flavus*, *Fusarium oxysporum*, *Rhizoctonia solani*) using the well diffusion method. Negligible antibacterial and antifungal activity was shown by all AuNPs, the lack of antimicrobial properties of AuNPs reported here underlines their inert and biocompatible nature. This makes AuNPs a potential substitute in biomedical applications like drug delivery systems because of their biocompatible carrier system with targeted specificity. (for details, see [1]). Further synthesis of gold and silver nanoparticles using various novel biological sources and its characterization was carried out. Second research article on the topic “Sustainable, single step, green biosynthesis of silver nanoparticles utilizing *Monstera deliciosa* leaf extract and estimation of its antimicrobial characteristics” is submitted to the Scopus indexed journal and currently under review. To study the effects of the irradiation on gold and silver substrates and other analysis regarding loading of chemical and biological samples on irradiated sample are under process.

References:

1. Janvi Shirsul, Ambuj Tripathi, Dambarudhar Mohanta and Balaprasad Ankamwar, 3 Biotech **14**, 43 (2024).

5.2.4 Modifications in properties of titanium carbide MXene by Ag doping via ion implantation technique for quantum dot sensitized solar cell applications

Iqbal Singh¹, Aman Mahajan¹, Devarani Devi², Fouran Singh² and Sundeep Chopra²

¹Department of Physics, Guru Nanak Dev University, Amritsar 143005, India

²Inter-University Accelerator Center, New Delhi 110067, India

Third-generation quantum dot-sensitized solar cells (QDSSCs) have attracted significant interest due to their economical production, streamlined manufacturing processes, and their ability to operate efficiently even under low illumination [1]. QDSSCs typically comprise a photoanode made of TiO₂ as an electron transport layer (ETL) sensitized with quantum dots, a polysulfide electrolyte as a hole transport layer (HTL), and a counter electrode (CE) composed of Cu₂S@brass [2]. A conventional mesoporous TiO₂ (m-TiO₂) based photoanode still suffers from various limitations, such as low light harvesting attributed to a wide band gap of TiO₂, and sluggish charge transport dynamics and numerous recombinations owing to the large grain boundaries of m-TiO₂. The light-harvesting of m-TiO₂ photoanode can be enhanced by scattering the incoming light or alternatively, expanding the absorption spectrum of the photoanode enabling it to capture a wider spectrum of wavelengths. Further, electron-hole recombinations can be reduced by establishing a more efficient transport network, facilitating the swift movement of electrons to the electrode. Additionally, creating new trap levels in the material can prevent electron-hole recombination, helping in the separation of charge carriers [3].

The current work is related to the ion implantation of transition metal (Ag) into MXene/TiO₂ films by utilizing low energy at different fluences of 5×10^{12} , 5×10^{13} , 5×10^{14} and 5×10^{15} ions-cm⁻² respectively. Further, the morphology and crystal structure of transition metal implanted MXene/TiO₂ samples were characterized through field emission scanning electron microscope, X-ray diffraction, and Raman spectroscopy. In addition to this, X-ray photoelectron spectroscopy investigations unveil the presence of Ag(I) oxidation state at 5×10^{14} ions-cm⁻² fluence whereas at higher fluence of 5×10^{15} ions-cm⁻², both Ag(I) and Ag(0) states were found. Moreover, the optical properties of the transition metal implanted MXene/TiO₂ samples were also studied through UV-visible and photoluminescence studies. The transition metal implantation significantly enhanced the light absorption and reduced the charge recombinations owing to the formation of defect states. Finally, the QDSSC device fabricated with 5×10^{14} ions-cm⁻² (Ag_3) exhibited the highest power conversion efficiency of 3.94% compared to the unimplanted MXene/TiO₂ based QDSSC (2.48%), attributed to enhanced absorption and minimization of charge recombinations, as corroborated from photovoltaic characteristics and Nyquist plots.

References:

1. I. Singh, V. Bhullar and A. Mahajan, Energy Fuels **37**, 15054 (2023).
2. I. Singh, V. Bhullar, D. Devi, F. Singh, S. Chopra, A. K. Debnath *et al.*, Mat. Sci. Eng. B **290**, 116342 (2023).
3. V. Bhullar, D. Devi, F. Singh, S. Chopra, A. K. Debnath, D. K. Aswal and A. Mahajan, Opt. Mater. **132**, 112800 (2023).

5.2.5 Copper ion irradiation studies on PNP transistor at different biasing conditions

M. Darshan¹, Arshiya Anjum¹, Asha P. Shirmi¹, H. Ankitha Kanekal², N. Pushpa², R. C. Meena³, Ambuj Tripathi³ and A. P. Gnana Prakash¹

¹Department of Studies in Physics, University of Mysore, Manasagangotri, Mysore 570006, India

²Department of PG Studies in Physics, JSS College, Ooty Road, Mysore-570025, India

³Inter-University Accelerator Center, New Delhi 110067, India

Integrated circuits (ICs) are miniature electronic circuits that are made up of millions of semiconductor devices such as transistors, diodes, resistors etc. ICs are building blocks of modern electronics and have numerous applications. Transistors are biased in certain required way in these ICs according to the application. Space being an extreme environment filled with energetic photons and charged particles that can cause severe degradation in performance and operating life of the semiconductor devices and in turn, leads to failure of space missions [1]. Thus, it is important to study the reliability of these devices before employing them.

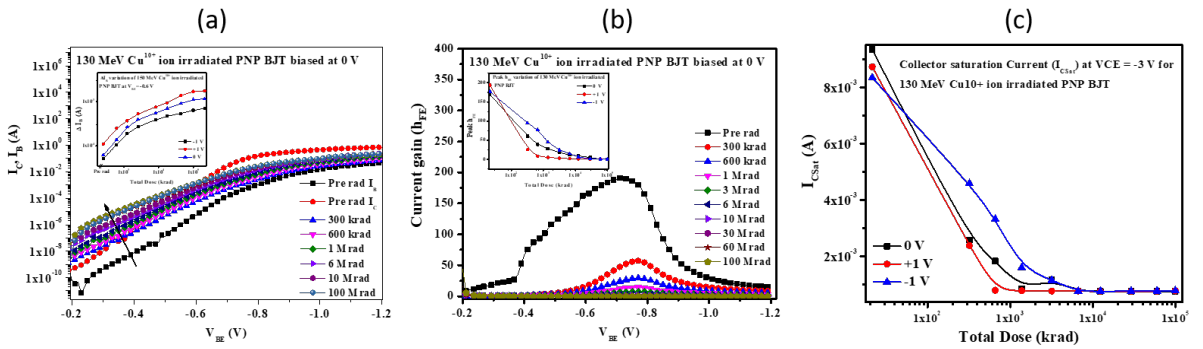


Figure 5.21: (a) Gummel characteristics of 130 MeV Cu^{10+} ion irradiated transistors biased at 0 V, (b) Variation of current gain for 130 MeV Cu^{10+} ion irradiated transistors biased at 0 V, (c) Variation of I_{CSat} at $V_{CE} = -3$ V for 130 MeV Cu^{10+} ion irradiated transistors biased at 0 V, +1 V and -1 V.

The PNP Bipolar Junction Transistors (BJTs) were exposed to 130 MeV Copper ions (Cu^{10+}) in 15UD Pelletron Accelerator at Inter University Accelerator Centre (IUAC), New Delhi, India. The irradiation was performed at different biasing conditions (0V, +1V and -1V) with fluence ranging from 5.5×10^8 ions/cm² to 1.8×10^{11} ions/cm² with current of 0.1 pA (particle nanoampere) which is equivalent to a dose range of 300 krad(Si) to 100 Mrad(Si). The ion irradiation and measurements were done in-situ to avoid the time dependent annealing of radiation defects created in the device. The experimental chamber was maintained at a vacuum of 10^{-6} mbar. The key electrical parameters like Gummel characteristics, excess base current ($\Delta I_B = I_{Bpost} - I_{Bpre}$), dc current gain (h_{fe}), output characteristics and collector saturation current (I_{CSat}) were studied as a function of total dose and some of the results are shown below. Fig. 5.21(a) shows the Gummel characteristics of 130 MeV Cu^{10+} ion irradiated transistors biased at 0 V, the inset shows the variation of ΔI_B with total dose for BJTs biased at 0 V, +1 V and -1 V. The variation of h_{fe} for 130 MeV Cu^{10+} ion irradiated PNP BJT biased at 0 V is shown in Fig. 5.21(b) and the inset shows the variation of peak h_{fe} with respect to total dose for devices biased at 0 V, +1 V and -1 V. The degradation in electrical parameters after irradiation is due to total ionizing dose (TID) and displacement damage effects. The PNP BJT has high emitter-periphery to emitter-area ratio which leads to greater TID effects in these devices. Fig. 5.21(c) shows the variation of I_{CSat} at $V_{CE} = -3$ V for 130 MeV Cu^{10+} ion irradiated transistors biased at 0 V, +1 V and -1 V with respect to total dose. The degradation in electrical characteristics is less for the devices irradiated at -1 V bias than at +1 V and 0 V due to the carrier injection annealing mechanism. The active mode operation for BJT is forward bias condition where the majority carriers (holes in PNP BJT) are flooded into the base region. The excessive charge carriers fill up the traps and thus decreasing the carrier trapping probability and eventually reduces the amount of ΔI_B [2-3]. The recombination current is more in +1 V biased PNP transistors. In BJTs, the degradation in current gain due to biasing during irradiation is highly dependent on transistor geometry.

5. RESEARCH ACTIVITIES

References:

1. R. D. Schrimpf *et al.*, IEEE Int. Reliab. Phys. Symp. **97**, (2008).
2. C. Liu *et al.*, IEEE Trans. Nucl. Sci. **62**, 3381 (2015).
3. L. J. Beattie *et al.*, Nucl. Instrum. Methods A **439**, 239 (2000).

5.2.6 130 MeV Copper ion and ^{60}Co gamma irradiation impact on electrical characteristics of N-channel depletion MOSFETs

H. Ankitha Kanekal¹, Arshiya Anjum², M. Darshan², Asha P. Shirni², N. Pushpa¹, R. C. Meena³, Ambuj Tripathi³, J. B. M. Krishna⁴ and A. P. Gnaa Prakash²

¹Department of PG Studies in Physics, JSS College, Ooty Road, Mysore 570025, India

²Department of Studies in Physics, University of Mysore, Manasagangotri, Mysore 570006, India

³Inter-University Accelerator Center, New Delhi 110067, India

⁴IUC-DAE CSR, Kolkata-700098, India

Metal Oxide Semiconductor Field Effect Transistors (MOSFETs) are the key components in advanced integrated circuits (ICs) and are extensively used in space, military and other high energy physics experiments like Large Hadron Colliders (LHCs) applications due to their faster switching speed and simple way of operation when compared to Bipolar Junction Transistors (BJTs) [1]. MOS devices need to be radiation tolerant upto multi Mrad's of total doses during their lifetime in order to use in space and planetary missions. Hence it is very essential to evaluate the radiation hardness of these devices. In this present work the N-channel depletion MOSFETs were exposed to 130 MeV Copper ions (Cu^{10+}) in fluence ranging from 5.5×10^8 ions/cm² to 1.8×10^{10} ions/cm² Cu^{10+} ions/cm² at room temperature at Inter University Accelerator Centre (IUAC), New Delhi. The corresponding gamma equivalent dose for the above mentioned fluence is 300 krad to 10 Mrad. The results of 130 MeV Cu^{10+} ion irradiation were compared with that of ^{60}Co gamma radiation results. The gamma irradiation was performed at Department of Studies in Physics, University of Mysore, Mysuru at a dose rate of 82.78 rad/s for the same identical doses.

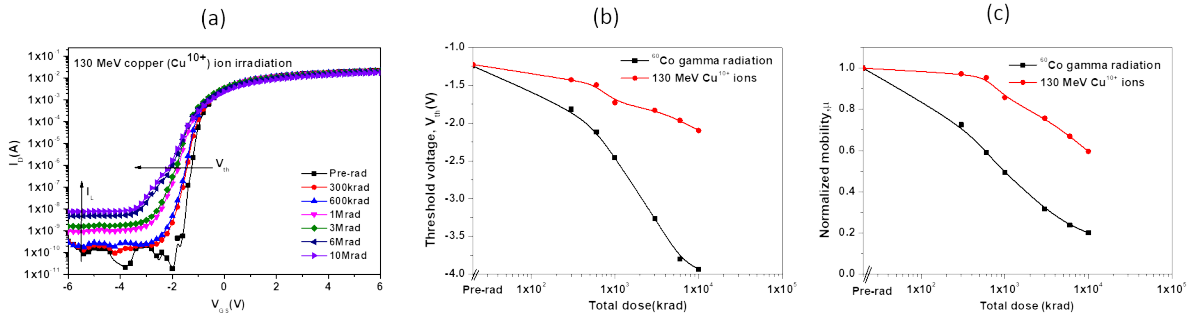


Figure 5.22: (a) Transfer characteristics of 130 MeV Cu^{10+} ion irradiated MOSFET, (b) Variation in (V_{th}) after 130 MeV Cu^{10+} ion and ^{60}Co gamma irradiation, (c) Variation in mobility after 130 MeV Cu^{10+} ion and ^{60}Co gamma irradiation.

Fig. 5.22(a) shows the transfer characteristics of N-channel MOSFET irradiated with 130 MeV Cu^{10+} ions. From the figure it can be observed that as the radiation dose increases the drain current (I_D) swings towards the negative gate voltage (V_{GS}). This degradation in the electrical characteristics of MOSFETs is due to the creation of interface (ΔN_{it}) and oxide trapped charges (ΔN_{ot}) near the Si/SiO₂ interface and SiO₂ respectively. These trapped charges induce a negative shift in the threshold voltage (V_{th}) of the MOSFETs as a result the leakage current and hence power consumption will increase which in turn degrade the functioning of MOSFET. Fig. 5.22(b) depicts the decrease in (V_{th}) with respect to radiation dose for 130 MeV Cu^{10+} ions and ^{60}Co gamma irradiated MOSFETs. The variation in the mobility (μ) of the charge carriers for 130 MeV Cu^{10+} ions and gamma irradiated MOSFETs is shown in Fig. 5.22(c). From the figure, it can be observed that the mobility of charge carriers decreases with increase in total dose. This observed reduction in the mobility of charge carriers in the channel is mainly due to the creation of radiation-induced interface trapped charges. These interface trapped charges act as Coulomb scattering centers and causes the removal of charge carriers from the channel thereby, degrading the mobility of charge carriers [3]. From the results, it is found that the degradation is more for the devices irradiated with ^{60}Co gamma radiation when

compared to 130 MeV Cu¹⁰⁺ ions. This may be due to the generation of more number electron-hole pairs during the gamma irradiation which results in the creation of more interface and oxide trapped charges.

References:

1. N. Pushpa *et al.*, Nucl. Instrum. Methods A **613**, 280 (2010).
2. A. P. Gnana Prakash *et al.*, Ind. J. Phys. **78**, 1187 (2004).
3. Arshiya Anjum *et al.*, IEEE Trans. Device Mater. Reliab. **19**, 696 (2019).

5.2.7 Cryogenic and high temperature effects on NPN transistors irradiated with 150 MeV iron ion

M. Darshan¹, Arshiya Anjum¹, Madhura N. Talwar¹, N. Pushpa², R. C. Meena³, Ambuj Tripathi³ and A. P. Gnana Prakash¹

¹Department of Studies in Physics, University of Mysore, Manasagangotri, Mysore 570006, India

²Department of PG Studies in Physics, JSS College, Ooty Road, Mysore-570 025, India

³Inter-University Accelerator Center, New Delhi 110067, India

Semiconductor devices are used in various applications such as communication systems, navigation systems, power systems and in scientific instruments such as gamma ray telescope used to detect high energy radiation from distant objects. Transistors are one of the widely used semiconductor devices in space applications due to their high linearity, small size, low power consumption and switching speed. The devices operating in the space environment are prone to radiation effects and other extreme environment effects such as extreme high and low temperatures, corrosive and pressure gradient condition etc., which can cause degradation to the electrical parameters of the device. Thus, it is very important to evaluate the radiation hardness of these devices for different radiations under different extreme environmental conditions [1].

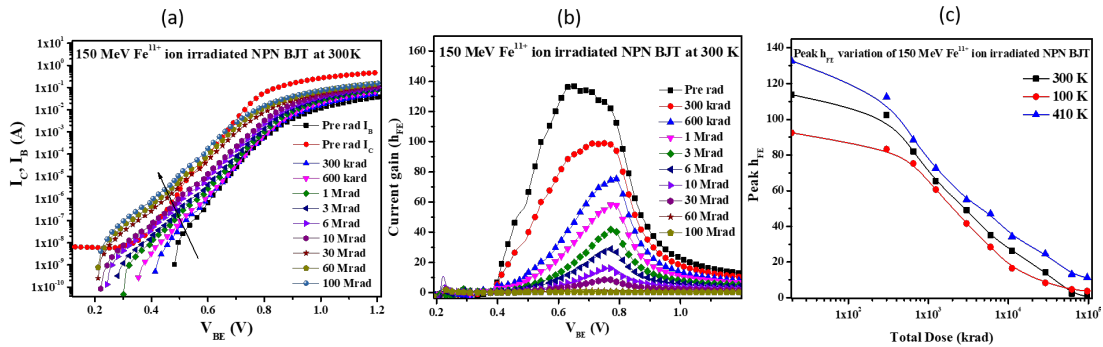


Figure 5.23: (a) Gummel characteristics of 150 MeV Fe¹¹⁺ ion irradiated transistors at 300 K, (b) Variation of current gain for 150 MeV Fe¹¹⁺ ion irradiated transistors at 300 K, (c) Variation of peak current gain for 150 MeV Fe¹¹⁺ ion irradiated transistors at 300 K, 100 K and 410 K.

In the present study the NPN transistors were exposed to 150 MeV Iron ions (Fe¹¹⁺) using 15UD Pelletron Accelerator at Inter University Accelerator Centre (IUAC), New Delhi, India. The irradiation was performed at room temperature (300 K), high temperature (410 K) and at cryogenic temperature (100 K) with the dose range of 300 krad(Si) to 100 Mrad(Si) which is equivalent to fluence ranging from 6.6×10^8 ions/cm² to 2.2×10^{11} ions/cm² with current of 0.1 pA (particle nanoampere). The experimental chamber was maintained at a vacuum of 10⁻⁶ mbar and all the terminals of the transistors were grounded during the irradiation. The key electrical parameters like Gummel characteristics, excess base current ($\Delta I_B = I_{Bpost} - I_{Bpre}$), dc current gain (h_{fe}), output characteristics and collector saturation current (I_{CSat}) were studied as a function of total dose. Fig. 5.23(a) shows Gummel characteristics of 150 MeV Fe¹¹⁺ ion irradiated transistors at 300 K. Fig. 5.23(b) shows the current gain degradation of NPN transistor irradiated with 150 MeV Fe¹¹⁺ ions at 300 K. The degradation in the electrical characteristics after irradiation is mainly due to the increased recombination current in the emitter base depletion region of the transistor. Fig. 5.23(c) shows the variation of peak current gain for 150 MeV Fe¹¹⁺ ion irradiated transistors at 300 K, 100 K and 410 K. It can be observed that the degradation in electrical parameters is more for the devices irradiated at 410 K than at 300 K and 100 K. This is due the fact that, the radiation induced traps will have high thermal energy at 410 K when compared to 300 K and 100 K. Excess electrons are injected from emitter to base since the built-in potential is very low at 410 K. The injected electrons recombine with holes in the

5. RESEARCH ACTIVITIES

base region thus contributing to the ΔI_B [2-3]. The increased surface recombination is due to the increased interface traps generated at high temperature.

References:

1. Denis I. Sotskov *et al.*, IEEE Trans. Nucl. Sci. **67**, 2396 (2020).
2. Daniel M. Fleetwood, IEEE Trans. Nucl. Sci. **68**, 509 (2021).
3. K. Naik *et al.*, Arch. Phys. Res. **4**, 74 (2013).

5.2.8 150 MeV Iron ion irradiation effects on N-channel MOSFETs at low temperature

Arshiya Anjum¹, M. Darshan¹, N. Pushpa², R. C. Meena³, Ambuj Tripathi³ and A. P. Gnana Prakash¹

¹Department of Studies in Physics, University of Mysore, Manasagangotri, Mysore 570006, India

²Department of PG Studies in Physics, JSS College, Ooty Road, Mysore 570025, India

³Inter-University Accelerator Center, New Delhi 110067, India

The electronic systems which operate under adverse ambient conditions that lie outside the domain of commercial or even military specifications are called extreme environment electronics (EEE). The N-channel depletion metal oxide semiconductor field effect transistors (MOSFETs) are the fundamental components for many EEE applications which require the devices to operate reliably for a long time at extreme temperatures and radiation-harsh environments. The incident ionizing radiation can cause an accumulation of charges to build up at the sensitive interface i.e., at Si/SiO₂ and thereby degrade the performance of the devices [1]. Thus, it is very important to study the radiation response of MOSFETs at different temperatures.

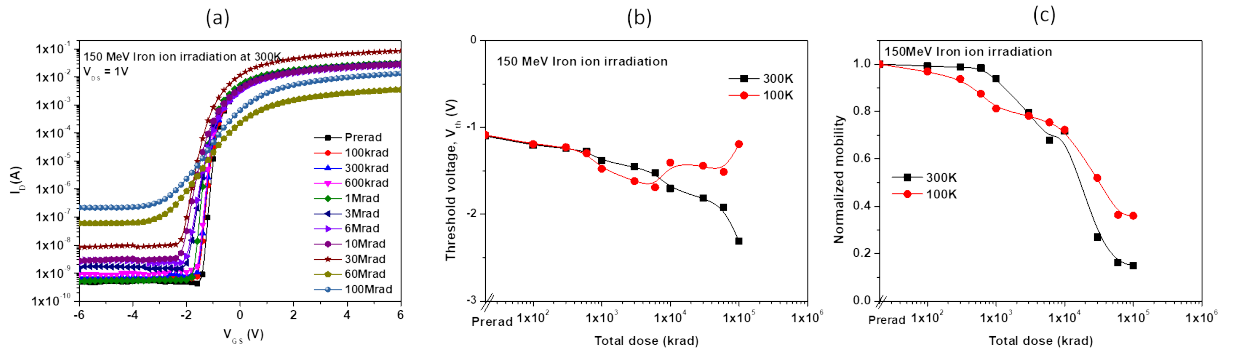


Figure 5.24: (a) Transfer characteristics of MOSFET irradiated at 300 K, (b) Variation in (V_{th}) after 150 MeV Fe¹¹⁺ ion irradiation, (c) Variation in μ after 150 MeV Fe¹¹⁺ ion irradiation.

The MOSFETs were exposed to 150 MeV Iron ions (Fe¹¹⁺) at room temperature (300 K) as well as low at temperature (100 K) at Inter University Accelerator Centre (IUAC), New Delhi in the fluence range of 2.18×10^8 ions/cm² to 2.18×10^{11} ions/cm² Fe¹¹⁺ ions/cm². The corresponding equivalent dose is 100 krad to 100 Mrad and the devices were grounded during irradiation. The electrical characterizations were done before and after irradiation at 300 K using Keithley dual source meter 2636A. The electrical characteristics of MOSFET such as threshold voltage (V_{th}), density of oxide trapped charges (N_{ot}), density of interface trapped charges (N_{it}), transconductance (g_m), mobility (μ) and leakage current (I_L) were studied as a function of total dose. The low temperature irradiation results were compared with the room temperature irradiation results. Fig. 5.24(a) represents the subthreshold characteristics of MOSFETs irradiated with 150 MeV Fe¹¹⁺ ions at 300 K. It can be observed from the figure that as the radiation dose increases the drain current (I_D) swings towards the negative gate voltage. A similar trend was observed for the devices irradiated at 100 K. The Fig. 5.24(b) and Fig. 5.24(c) show the variation of (V_{th}) and μ with respect to total dose for 150 MeV Fe¹¹⁺ ions irradiated MOSFETs at 100 K and 300 K. It can be seen that (V_{th}) degraded with increase in radiation dose however, the degradation is more for the MOSFETs irradiated at 300 K. This indicates that there will be very less generation of radiation-induced interface traps and oxide traps at 100 K along with the creation of some point defects and displacement damages at low temperature. This is due to the fact that at low temperatures the thermal energy of atoms will be very low as compared to room temperature as a result, the radiation-induced interface and oxide traps freeze out in the device structure. Hence, the MOSFETs show significant radiation hardness at low temperatures when compared to high temperature.

References:

1. V. N. Hegde *et al.*, Solid State Electronics **206**, 108671 (2023).
2. Daniel M. Fleetwood, IEEE Trans. Nucl. Sci. **68**, 509 (2021).
3. H. Zhao and X. Liu, Cryogenics **59**, 49 (2014).

5.2.9 Tailoring conductivity of FeS₂ thin films using ion implantation for photovoltaic applications

Rudra Narayan Chakraborty¹ and Kasilingam Senthilkumar¹

¹Department of Physics, National Institute of Technology Meghalaya, Shillong 793003, India

Iron pyrite (FeS₂) has been considered as a potential hole transport layer (HTL) material in copper zinc tin sulfide (CZTS) based solar cell due to its abundant availability, cost effectiveness and suitable optoelectronic properties. Since FeS₂ generally demonstrates n-type conductivity, it is not suitable to use as HTL. Some studies have reported p-type conductivity of FeS₂ thin films. This sudden change of conductivity is an active area of research. Controversies exist regarding variations in experimental conditions, synthesis techniques, dopant concentration and characterization methods, which can significantly impact the observed conductivity type and its reproducibility. Challenges are associated with achieving consistent and p-type conductivity through extrinsic defect doping in FeS₂. In that case ion implantation could potentially be the most suitable option due to its precision depth, and dose control as well as its versatility.

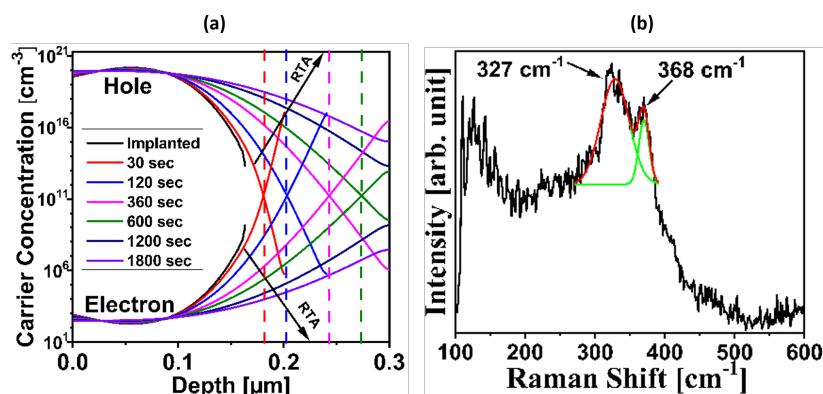


Figure 5.25: (a) Carrier concentration of oxygen implanted (dose 10^{15} cm^{-2}) FeS₂ thin film and annealed for different intervals, (b) Raman spectra of DC sputtered FeS₂ thin film on Soda lime glass substrate.

We used ATHENA process simulator module of SILVACO TCAD simulation package to simulate ion implantation and subsequent rapid thermal annealing (RTA). Pyrite phase crystal thin film of FeS₂ with dimensions of $0.3 \mu\text{m} \times 0.3 \mu\text{m}$ was utilized as target. Three different ions, namely ¹⁶O, ³¹P, and ⁷⁵As, were utilized for implantation simulation. We employed three distinct doses [10^5 , 10^{10} , and 10^{15} cm^{-2}] to investigate the carrier concentration variation with dose. The ion beam energy value was fixed at 40 keV for every ion. A substrate tilt of 7° was employed to avoid channeling. Due to the absence of experimental investigations on ion implantation in FeS₂, a sophisticated simulation model is required. The Monte Carlo technique was employed to simulate ion implantation because of its flexibility and universality under non-standard conditions. We have simulated RTA in N₂, Dry O₂, Wet O₂ ambient at 700°C and different time intervals (30 - 1800 sec) to study the diffusion properties and carrier concentration. We demonstrate successful p-type doping of FeS₂ with a hole concentration of $\sim 10^{20} \text{ cm}^{-3}$ in case of 10^{15} cm^{-2} dose [Fig. 5.25(a)]. We observed that p-type conductivity is achievable using O²⁻, P²⁻, and As²⁻ implantation. By tuning the ion beam energy, we can control the depth of the p-type layer for thin films of different thicknesses. Our investigation has provided valuable insights into a potentially fruitful approach for attaining p-type conductivity in FeS₂ thin films, which holds promise as a viable HTL for CZTS-based solar cells [1].

In order to experimentally validate our simulated result, we have prepared FeS₂ thin films on soda lime glass substrate at room temperature in Argon (Ar) atmosphere using DC sputtering. The DC power used was 100 W with an Ar flow rate of 10 sccm. The deposition was done for 1 hour and a substrate rotation

5. RESEARCH ACTIVITIES

of 10 rpm was maintained throughout the entire deposition time. The Raman spectra show FeS_2 peaks at 327 and 368 cm^{-1} which corresponds to E_g and A_g respectively [Fig. 5.25(b)]. T_g peak is not resolved. The peaks are broader, indicating a lower degree of crystallinity [2]. We expect annealing in sulfur environment will improve the crystallinity of the thin film. We will be doing implantation (^{16}O , ^{32}S , and ^{58}Ni) and subsequent characterization studies on these samples at IUAC.

References:

1. Rudra Narayan Chakraborty, Dipta Suryya Mahanta, Santu Mazumder and Senthilkumar Kasilingam, Phys. Scr. **99**, 055953 (2024).
2. Z. Mutlu, B. Debnath, S. Su, C. Li, M. Ozkan, K. N. Bozhilov, R. K. Lake and C. S. Ozkan, J. Mater. Chem. C **6**, 4753 (2018).

5.2.10 Z-Scheme based WS_2/WO_3 and WS_2/TiO_2 nanostructures for hydrogen evolution reaction investigation

Divyanshi Joshi¹, Shivani Dangwal¹, Saurabh Rawat¹, Charu Dwivedi² and Himani Sharma¹

¹Functional nanomaterial research laboratory, Department of Physics, Doon University, Dehradun 248001, India

²Department of Chemistry, Doon University, Dehradun 248001, India

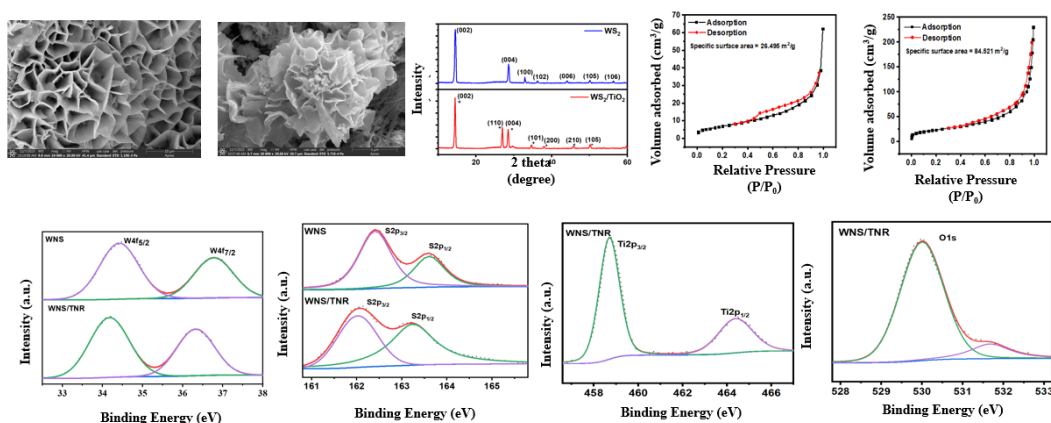


Figure 5.26: (a) SEM images of WNS, (b) SEM images of WNS/TNR, (c) XRD spectra of WNS and WNS/TNR, (d) BET plots of WNS, (e) WNS/TNR, (f) XPS plots of W in WNS and WNS/TNR, (g) XPS plots of S in WNS and WNS/TNR, (h) XPS plots of T in WNS/TNR, (i) XPS plots of O in WNS/TNR showing corresponding peaks for each elements.

WS_2 nanosheets were grown on TiO_2 nanorods (WNS/TNR) through hydrothermal method [1,2]. The samples' morphologies and structures underwent evaluation through field emission scanning electron microscopy (FESEM). Analysis of these images (Fig. 5.26(a)) unveiled that WNS displayed a sheet-like morphology. WNS was grown on these nanorods, showing their uniform distribution, as depicted in (Fig. 5.26(b)). Notably, TNR were covered completely by WNS. X-ray diffraction (XRD) was obtained to confirm the crystal structure of the samples i.e. pristine WNS (Fig. 5.26(c)) and the resulting WNS/TNR heterostructure (Fig. 5.24(d)). The specific lattice planes indexed as (002), (004), (100), (102), (006), (106) and (105) correspond to respective 2θ values of 14.36°, 28.56°, 32.86°, 36.22°, 44.08°, 50.2° and 56.3°. These indexing values align with the hexagonal phase of WNS, as referenced in the JCPDS file 08-0237 [1,2]. In the XRD patterns of the WNS/TNR heterostructure, diffraction peaks corresponding to rutile phase of TiO_2 can be observed corresponding to (110), (101), (200) and (210) at 27°, 34.6°, 38.03° and 45°, according to JCPDS file 82-0514 [2]. The remaining peaks observed at 14.4°, 28.5° and 50.23° are assigned to (002), (004) and (105), plane of WNS. The specific surface area of WNS and WNS/TNR were also analyzed using N_2 adsorption and desorption isotherms (Fig. 5.26(d,e)). The surface area for pristine WNS was found to be 26.495 m^2/g and for WNS/TNR heterostructure the specific surface area was 84.521 m^2/g . The increase in surface area of heterostructure implies it will provide higher catalytic active sites and thus will result in improved HER performance. For the analysis of electronic interactions at the interface of WNS and WNS/TNR heterostructure, X-ray photoelectron spectroscopy (XPS) characterization was utilized. As

illustrated in Fig. 5.26(f-i), peaks corresponding to W 4f, S 2p, Ti 2p and O 1s are observed in the obtained heterostructure, confirming the presence of elements in the samples. Fig. 5.26(f) illustrates the XPS scan of W in pristine WNS and WNS/TNR heterostructure. The binding energy observed at 37.3 eV and 35.2 eV corresponds to W 4p_{3/2} and W 4f_{5/2} respectively. Furthermore, peaks at 163.17 eV and 162.07 eV in Fig. 5.26(g) corresponds to S 2p_{1/2} and S 2p_{3/2} of S orbital. Additionally, spectra of Ti with peaks at 464.4 eV and 458.7 eV corresponding to Ti 2p_{1/2} and Ti 2p_{3/2} confirms its presence (Fig. 5.26(h)). The oxygen spectrum (Fig. 5.26(i)) for O 1s with peaks at 530 and 531.6 eV corresponding to lattice and non-lattice or hydroxyl oxygen was also obtained. The samples are irradiated with Au ions from Pelletron at various fluences and their characterization is under process.

References:

1. S. Cao, T. Liu, S. Hussain, W. Zeng, X. Peng and F. Pan, *Materials Letters* **129**, 205 (2014).
2. P. Bamola, M. Sharma, C. Dwivedi, B. Singh *et al.*, *Mats. Sci. Engg. B* **273**, 115403 (2021).

5.2.11 Ion beam induced modification of ferroelectric polymer nanocomposite for EMI shielding application

Santhoshkumar Dani¹, Arshad A. H.¹, S. S. Kulkarni², Ramcharan Meena³, Pravin Kumar³, Ambuj Tripathi³ and U. V. Khadke¹

¹*Department of Studies and Research in Physics, Vijayanagara Sri Krishnadevaraya University, Ballari 583105, India*

²*Department of Physics, KLS Gogte Institute of Technology, Visvesvaraya Technological University, Belgaum-06, India*

³*Material Science Group, Inter-University Accelerator Center, New Delhi 110067, India*

In today's world, electromagnetic interference (EMI) from electronic gadgets and wireless systems can wreak havoc on functionality, data integrity, and even human health. To tackle this issue head-on, the development of effective shielding materials is essential. Our research delves into the process of EMI shielding, which operates through three main modes: surface reflection, absorption, and multiple reflections. Different materials play different roles in this process - conductive materials reflect, those with high dielectric constants absorb, and magnetic materials enhance multiple reflections, all contributing to shielding effectiveness (SE).

Ion beam modification enhances EMI-SE properties by bombarding materials' surfaces with conducting (Carbon), magnetic (Nickel), and insulating (Oxygen) ion beams. To investigate the effects of swift heavy ion (SHI) irradiation on the structural, electrical, and EMI shielding properties of PVDF and PVDF NC thin films, they were irradiated with 100 MeV O⁷⁺ ions, 80 MeV C⁶⁺ ions, and 70 MeV Ni⁵⁺ ions at various fluences ranging from 1×10^{11} ions/cm² to 1×10^{13} ions/cm², and then compared with unirradiated samples.

Our study includes the synthesis of PVDF thin films and nanocomposites (NCs) using solution casting, incorporating TiO₂, MWCNT, NiO, BaTiO₃ and NiTiO₃ nanoparticles. Characterized via XRD, FTIR, and FESEM, enhancements in crystallinity and conformational changes were observed. EMI shielding effectiveness (EMI-SE) within the Ku-band (12 – 18 GHz) was evaluated using a Vector Network Analyzer, revealing uniform nanoparticle distribution and improved structural properties. Irradiation took place in a material science beamline chamber maintained with a high vacuum ($>10^{-6}$ torr), perpendicular to the sample surface, with the ion beam focused onto a 20 mm diameter spot and scanned over a 20×10 mm² area using a magnetic scanner. Further investigation exposed PVDF and its nanocomposite films to SHI irradiation to assess its impact on structural, electrical, and EMI shielding properties in the Ku band. This irradiation prompted noticeable changes such as increased thickness, lattice modifications, and reduced crystallinity. Dielectric properties exhibited varying decay rates and shifts in complex permittivity, indicating alterations in electronic oscillations.

The 100 MeV ¹⁶O⁷⁺ ion beam induced significant changes in PVDF films, including increased thickness and lattice modifications. XRD analysis revealed higher dislocation density, lattice strain, and reduced crystallinity with rising fluence [1,2]. FESEM micrographs depicted the emergence of an amorphous phase and grain-like structures due to swift heavy ion energy transfer, with EDS confirming elemental composition. Additionally, dielectric properties showed varying decay rates and shifts in the real part of complex permittivity (ϵ'), primarily due to free radicals and space charge relaxation at higher frequencies. A reduction in the imaginary part of complex permittivity (ϵ'') with increasing frequency suggested challenges in aligning induced charges with the reversing field, affecting electronic oscillations. Ion beam irradiation induced intricate modifications in the structure and electrical properties of PVDF films. Remarkably, the EMI shielding effectiveness (EMI-SE) improved with the increasing fluence of 100 MeV O⁷⁺ ions in the PVDF matrix [3], albeit decreasing with rising frequency. Above 16 GHz, EMI-SE plots for all samples converged due to the hindrance of dipole polarization concerning frequency.

5. RESEARCH ACTIVITIES

The research project under BTR1-68127 aims to comprehensively understand the effects of ion beam irradiation on structural, chemical, and electrical properties of PVDF and PVDF NC thin films, as well as EMI-SE.

References:

1. D. Fink, Fundamentals of ion-irradiated polymers, In: Springer Series in Materials Science.
2. D. S. Rana, D. K. Chaturvedi and J. K. Quamara, J. Optoelectron. Adv. Mater. **11**, 705 (2009).
3. S. Dani, A. A. H. Arshad, P. Patil, R. Meena, P. Kumar, A. Tripathi and U. V. Khadke, Radiat. Eff. Defects Solids (in press).

5.2.12 Development of novel thermoluminescent and photoluminescent nanomaterials and investigations on their response to C and Ag ions irradiation

Rahul Awasthi¹, R. Arun Kumar¹ and K. Asokan²

¹School of Sciences (Physics) National Institute of Technology Andhra Pradesh, Tadepalligudem 534101, India

²Material Science Group, Inter-University Accelerator Center, New Delhi 110067, India

Ion beams have gained growing attention in both fundamental and applied nanomaterial research. Judiciously selection of ion types and their energy to tailor the desired properties of thermoluminescent (TL) and photoluminescent (PL) responsive nanomaterials, pioneering a new research avenue. There's a growing demand to develop customizable TL materials for varied applications like dosimetry, 2D dose mapping, and temperature sensing [1]. In this regard, Lithium tetraborate ($\text{Li}_2\text{B}_4\text{O}_7$) boasts an effective atomic number (7.3) akin to human tissue, with excellent chemical and thermal stability and transparency spanning 200 to 3000 nm. Doping with copper (Cu), manganese (Mn), and co-doped (Cu, Ag, P), yields distinct glow peaks from 453-493 K, showcasing linear responses across doses ranging from 10^{-3} Gy to 10^{+3} Gy with minimal fading [2,3,4,5]. Likewise, LiKB_4O_7 shows tissue-equivalent properties, non-hygroscopic nature, and robust stability. The undoped single crystal displaying two resolved thermoluminescence peaks at 112 K and 132 K. Europium-doped exhibits two overlapping peaks at 457 K, advantageous for dosimetry [6].

Furthering the work, polycrystalline lithium tetraborate material was synthesized by the microwave-assisted combustion route. The structural parameters of the polycrystalline nanomaterial of lithium tetraborate ($\text{Li}_2\text{B}_4\text{O}_7$) were validated utilizing by the Bruker D8 Advance x-ray diffractometer equipped with (Cu-K_α) radiation operating with a wavelength of 1.540 Å. The diffraction peaks exhibited excellent conformity with the JCPDS data reference no. 18-0717. Following Rietveld refinement, the powder XRD pattern revealed the tetragonal structure of the sample with lattice parameters $a = b = 9.479$ Å, $c = 10.290$ Å and cell volume $V = 924.571$ Å³. Fourier transform infrared (FT-IR) spectra ranging from 400 to 4000 cm^{-1} were recorded to examine the bond characteristics and chemical composition of $\text{Li}_2\text{B}_4\text{O}_7$, utilizing the Bruker- α FT-IR spectrometer. Within the measured infrared spectrum, the vibrational modes of lithium tetraborate exhibit three discernible regions. The first region, spanning from 1200 to 1750 cm^{-1} , corresponds to the asymmetric stretching and bending vibrations of the B-O bond in trigonal BO_3 units. The second region, ranging from 800 to 1200 cm^{-1} , is attributed to the B-O bond stretching of tetrahedral BO_4 units. The third region, within the 600-800 cm^{-1} range, originates from the bending vibrations of the B-O-B linkages within the borate network. Additionally, the presence of Li-O stretching is indicated by the peak observed at 420 cm^{-1} [7]. UV-Visible-NIR spectroscopy was used to examine the electronic structure and determine the material's band gap. It was discovered that the band gap of the polycrystalline $\text{Li}_2\text{B}_4\text{O}_7$ nanomaterial is 5.32 eV. Additionally, it was observed that the material possesses a transmittance window within the range of 250-2200 cm^{-1} , highlighting its potential as a favorable host material. To assess the impact of ion irradiation on the designated material and ascertain the diverse parameters associated with ion interaction, such as range, vacancy creation, and energy dissipation, SRIM analysis was conducted for the 60 MeV carbon ion beam. The analysis indicates a penetration depth of 106 μm , and examination of the ionization curve suggests that the majority of the incident ion's energy is allocated towards generating ions within the material, with minimal recoil observed at this energy level. This implies that electronic energy loss predominates, presenting a favorable scenario for altering the structural and optical characteristics of the material under study.

References:

1. V. Kortov, Radiat. Meas. **42**, 576 (2007).
2. E. Pekpak, A. Yilmaz and G. Ozbayoglu, J. Alloys Compd. **509**, 2466 (2011).
3. A. Kumaresh, R. Arun Kumar, N. Ravikumar, U. Madhusoodanan *et al.*, Chin. Phys. B **25**, 058105 (2016).

4. C. Furreta, M. Prokic, R. Salamon, V. Prokic and G. Kitis, Nucl. Instrum. Methods A **456**, 411 (2001).
5. M. Ignatovych, M. Fasoli and A. Kelemen, Radiat. Phys. Chem. **81**, 1528 (2012).
6. N. Ravikumar, R. Arun Kumar and U. Madhusoodanan, J Mater Sci: Mater Electron **29**, 18511 (2018).
7. N. Can, T. Karali, P. Townsend and F. Yildiz, J. Phys. D: Appl. Phys. **39**, 2038 (2006).
8. V. T. Adamiv, O. T. Antonyak, Ya. V. Burak, I. M. Teslyuk and J. Lumin. **128**, 549 (2008).

5.2.13 Role of ion beam in dye sensitize solar cells

Allwin Rajesh Somu¹, Ragavendran Venkatesan¹, Jayanthinath Mayandi¹ and Indra Sulania²

¹Department of Materials Science, School of chemistry, Madurai Kamaraj University, Madurai 625021, India

²Inter-University Accelerator Center, New Delhi 110067, India

Our group has been working in the field of synthesizing various multiphase TiO₂ nanostructures to develop dye-sensitized solar cells [1,2]. Ion beam irradiation is a crucial tool for improving device efficiency and material properties, such as crystalline structure and defects, which can significantly impact solar cell performance. It is a valuable tool for investigating and optimizing the properties of dye-sensitized solar cells (DSSCs), leading to advancements in solar cell technology. The present study aims to evaluate the anchoring mechanism of silver ions in TiO₂ photoanodes used in DSSCs using ion beam irradiations. It also seeks to understand dye and electrolyte adsorption on the photoanode, potentially revolutionizing third-generation solar cells by demonstrating Ag ion bonding to semiconductor nanoparticles. The as-synthesized TiO₂ nanomaterial were found to poses highly crystalline anatase phase confirmed by X-ray diffraction (XRD) which is well matched with previous reports. SEM confirms the morphology of uniform hollow spheres which are self-assembled and provide large surface area and higher volumetric energy density. The band gap value of TiO₂ was 3.15eV. The elemental analysis by energy dispersive X-Ray spectroscopy (EDAX) confirmed the composition of titanium and oxygen.

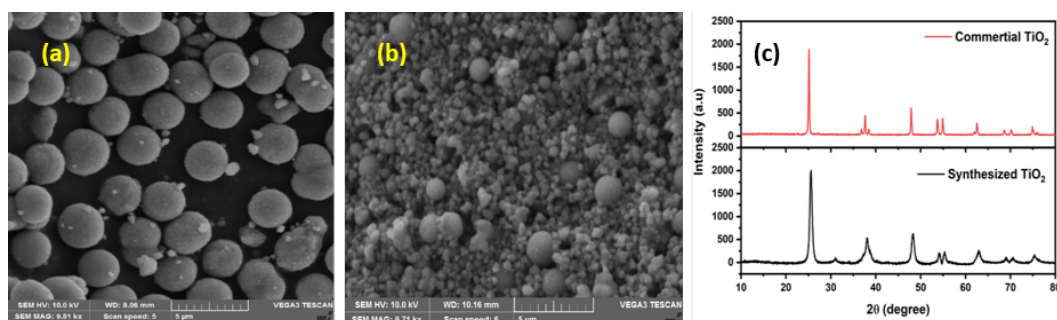


Figure 5.27: (a) the as synthesized TiO₂ micro spheres, (b) TiO₂ micro spheres after irradiating with Ag ion, (c) XRD pattern of synthezised and commertial TiO₂ spheres.

To investigate the effects of ion beam irradiation on the structural and optical properties of TiO₂ thin films, we deposited TiO₂ on FTO substrate using the screen-printing technique at Madurai Kamaraj University. After conducting a structural analysis, the films were irradiated with (Low energy ion beam) 100 keV Ag⁺ ions at three different ion fluences: 1×10^{14} ions/cm², 1×10^{15} ions/cm², and 1×10^{16} ions/cm² using NEIB facility at IUAC, New Delhi. Throughout the irradiation process, all the films were securely fixed to the target ladder placed inside a high vacuum chamber ($\sim 10^{-6}$ torr), To investigate the structural changes resulting from irradiation, we performed XRD measurements on thin films exposed to radiation at room temperature. SEM confirms the impact of ion irradiation on the samples and we can visualize the uniform craters like structures on the surface of the photo anode as shown in Fig. 5.27. Currently, our focus is on analysing the remaining measurements to gain insights into the impact of irradiation on optical properties.

References:

1. R. Selvapriya, T. Abhijith, V. Ragavendran, V. Sasirekha, V. Reddy and J. Mayandi, Mater. Lett. **276**, 128194 (2020).
2. R. Selvapriya, V. Sasirekha, P. Vajeeston, J. Pearce and J. Mayandi, Ceram. Int. **47**, 8094 (2021).

5. RESEARCH ACTIVITIES

5.2.14 Study on damage of Gd₂O₃-CeO₂ under electronic energy loss and nuclear energy loss regime: comparison between bulk-like and nanostructure

Waseem Ul Haq¹, Vinita Grover², Fouran Singh³, Sanjay Kumar³, Parswajit Kalita⁴ and Santanu Ghosh^{1*}

¹Department of Physics, Indian Institute of Technology Delhi, New Delhi 110016, India

²Chemistry Division, Bhabha Atomic Research Centre, Mumbai 400085, India

³Material Science Group, Inter-University Accelerator Centre, New Delhi 110067, India

⁴Department of Physics, University of Petroleum & Energy Studies, Dehradun 248007, India

To understand the physical phenomena responsible for radiation damage of the materials used in nuclear reactors, and thus study their operation life and/or efficiency, it is required to simulate the condition by exposing them to energetic ions. Ceria (CeO₂) has been proposed as one of the inert matrices for the transmutation of minor actinides in the futuristic inert matrix fuel (IMF) concept. The inert matrix should also consist of burnable poison to compensate the initial reactivity of fuel. In this context, Gadolinium (Gd) is an excellent burnable poison with a high neutron absorption cross-section. In view of this, Gd₂O₃-CeO₂ nano-powders were synthesized and sintered at 800°C and 1300°C to obtain different grain sizes and morphology. FESEM and TEM were carried out to study the grain size of pristine pellets. The sintered pellets were irradiated with 80 MeV Ag ions (electronic energy loss (Se) regime) at room temperature to emulate the effect of fission fragments. For analysis of the effect of grain size on the irradiation-induced structural degradation at different fluences, GIXRD and Raman spectroscopy were performed. Significantly large damage has been observed for the smaller grain-sized samples (sintered at 800°C) as compared to the large grain-sized sample (sintered at 1300°C). Neither of the samples amorphized under present experimental conditions as indicated by the presence of the Raman active T_{2g} mode (centred at 462 cm⁻¹) and all XRD peaks of fluorite cubic structure up to highest fluence employed (1×10¹⁴ ions/cm²). The radiation tolerance behaviour of the samples is understood with the help of thermal spike simulation, which indicates higher transient lattice temperatures with longer durations upon irradiation. Gd-doped ceria thus possesses good radiation stability in the Se regime indicating its potential for application in IMFs [1].

In order to investigate the effects of Low energy ion beam irradiation on the structural and behavioural change in Gd-doped Ceria, we prepared the three different-grained size samples and employed various characterization techniques. After initial characterization via XRD, Raman Spectroscopy and FESEM, these samples were exposed to 400 KeV Kr⁺ ions at different fluences at IUAC, New Delhi. GIXRD patterns & Raman Spectroscopy shows that there are significant changes in the Gd-doped Ceria post-irradiation. XPS measurement and detailed analysis of the irradiated samples were also performed.

References:

1. Waseem Ul Haq, V. Grover, Parswajit Kalita, Rakesh Shukla *et al.*, Phys. Chem. Chem. Phys. **26**, 5311 (2024).

5.2.15 Adsorption capacity of poly (N-tert-amylacrylamide-co-acrylamide/ionic liquid) Fe₃O₄ nanocomposite hydrogels in methylene blue solution

P. Pazhanisamy¹, Indra Sulania², E. Kayalvizhy³, T. Gomathi⁴ and B. Uma⁵

¹Department of Chemistry, Sir Theagaraya College (Affiliated to University of Madras), Chennai 600021, India

²Material Science, Inter-University Acceleration Centre, New Delhi 110067, India

³Department of Chemistry, PSGR Krishnammal College for Women, Coimbatore 641004, India

⁴Department of Chemistry, DKM College for Women, Vellore 632115, India

⁵Department of Zoology, Bharathi Women's College, Chennai 600108, India

(1) Adsorption capacity of poly (N-tert-amylacrylamide-co-Acrylamide/Ionic Liquid) Fe₃O₄: Nanocomposite hydrogels in methylene blue solution:

Poly(N-tart-amyl acrylamide-co-Acrylamide/AMPS IL) Fe₃O₄ nanocomposite hydrogels were synthesized by free-radical polymerization. About 0.5 g of N-tart-amyl acrylamide, 0.5 g of Acrylamide and 0.5 g of AMPSIL monomers were dissolved in 3: 1 Methanol/water medium with MBA crosslinker and APS as initiator maintained at 60°C for 6 hours. The synthesized hydrogels washed with the same solvent to remove the unreacted monomers. Fe₃O₄ NPs were intercalated via in situ polymerization. The synthesized Nanocomposite Hydrogels were characterized by FT-IR, SEM, TGA and XRD analysis. SEM analysis showed spherical like Fe₃O₄ NPs are present in the matrix (Fig. 5.28). The Hydrogels are subjected to swelling in the MB dye solution to study the swelling capacity [1].

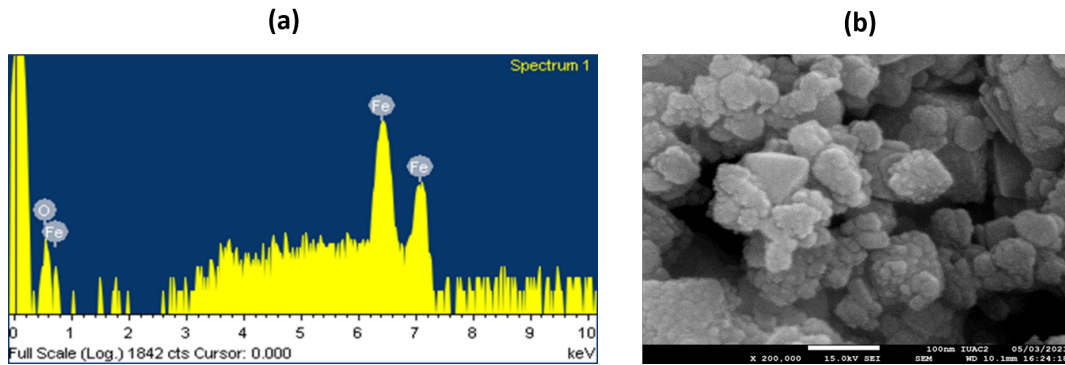


Figure 5.28: SEM and EDAX images of Bio charred materials (AC).

(2) Synthesis and catalytic reduction of methylene blue dye by bio-activated carbon based Fe_3O_4 nanocomposites:

Algae bio materials was collected from sea shore at Kovalam, Chennai, Tamil Nadu. The collected algae was dried at room temperature for a week under darkness. The dried algae was placed in a furnace maintained at 500°C to prepare the activated carbon and powdered. The powder carbon material dispersed in the $\text{Fe}^{2+}/\text{Fe}^{3+}$ solution with stirring at 80°C and Sodium hydroxide solution was added drop wise to reduce the Ferrate NPs on the surface of the carbon materials. The Functionalized activated carbon was characterized by FTIR spectroscopy, XRD, SEM analysis and UV-Visible spectrophotometer. The absorption peak at 555.56 cm^{-1} from the FTIR analysis confirmed the formation of Fe_3O_4 NPs on the surface of the carbon materials. XRD analysis indicated the crystallinity and the predominant peak at $2\theta = 35.5^\circ$ showed spherical shaped nanoparticles. SEM and EDAX reveals the formation functionalized Bio charred materials (AC). Methylene Blue dye adsorption by the activated carbon adsorbent showed 94.5% dye removal.

References:

1. P. Pazhanisamy, Indra Sulania, E. Kayalvizhy, T. Gomathi and B. Uma, *YMER* **22**, 363 (2023).

5.2.16 Structural, optical and magnetic properties of Ag irradiated $\alpha\text{-Fe}_2\text{O}_3$ thin films

Vimal Narayan Sahoo¹, R. N. Bhowmik¹, A. Tripathi², S. K. Kedia², R. C. Meena² and S. A. Khan²

¹Department of Physics, R.V Nagar, Pondicherry University, Kalapet 605014, India

²Material Science Division, Inter-University Accelerator Centre, Aruna Asaf Ali Marg, New Delhi 110067, India

Hematite ($\alpha\text{-Fe}_2\text{O}_3$) and transition metals (TMs) doped hematite ($\alpha\text{-Fe}_2\text{O}_3$) are materials of interest of this work [1]. In this work we used Co/Ti co-doped material as our basic material [2]. The basic focus of the work is to prepare this material using different methods and correspondingly studying their physical properties (which includes structural, morphological, electrical and magnetic). The works carried out in IUAC, New Delhi in session 2021-2022 are as follows (a) preparation of thin films of Fe_2O_3 and Co/Ti co-doped Fe_2O_3 , (b) FE-SEM and EDX analysis of target materials which were used for preparation of thin films. Some of the results of work done at IUAC, New Delhi in academic year 2021-2022 are published [2]. The works carried out in IUAC, New Delhi in session 2022-2023 are as follows (a) RBS measurements of undoped Fe_2O_3 and Co/Ti co-doped Fe_2O_3 thin films (b) Ion beam irradiation (Ag, Li, O) on undoped Fe_2O_3 and Co/Ti co-doped Fe_2O_3 thin films on Si $\langle 100 \rangle$ substrates at HEIBF. Some of the physical properties of the thin films and irradiated films has been studied in the academic year 2023-2024. These includes (a) Raman mapping, (b) optical properties using UV-Visible spectroscopy, (c) MOKE and (d) magnetic properties using PPMS. Some of the earlier works has been published in academic year 2023-2024.

The Raman mapping of the film has been studied using the Raman spectrometer (Renishaw, UK) which shows the presence of Fe atoms on the surface of the Ag- irradiated Fe_2O_3 film (120 MeV energy and 1×10^{13} ions/cm²). UV-Visible spectra of Ag irradiated Fe_2O_3 film has been studied using UV-VIS-NIR spectrometer (Varian model; 5000). The direct band gap for the irradiated films has been obtained from the $(\alpha h\nu)^2$ vs. $h\nu$ plots. The band gap (E_g) values are found to be 4.57 eV. In the similar way the band gap values for other irradiated films has been calculated. L-MOKE were measured at room temperature for the irradiated Ag ions on Fe_2O_3 thin films for determine the surface magnetic properties. Hysteresis loops are observed

5. RESEARCH ACTIVITIES

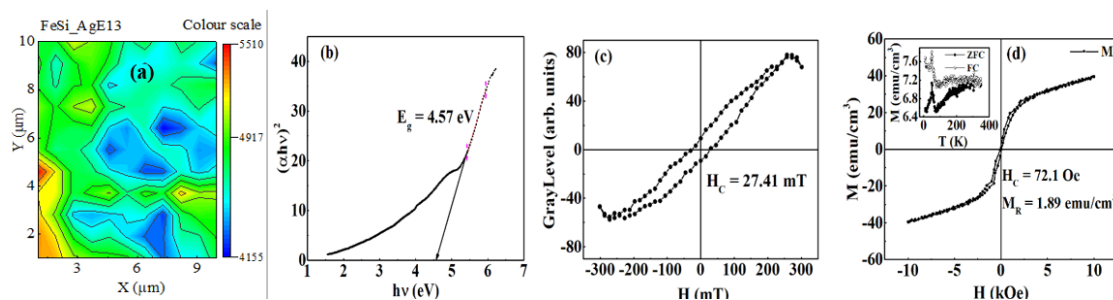


Figure 5.29: (a) Raman mapping, (b) $(\alpha h\nu)^2$ vs. $h\nu$ plots obtained using UV-Vis spectra, (c) L-MOKE (Longitudinal Magneto-Optic Kerr Effect), (d) M-H loop at 10 K and M-T plot (inset) for Ag irradiated (Fluence 1×10^{13} ions/cm²) Fe₂O₃ thin film.

for Ag irradiated Fe₂O₃ films in fluence range 1×10^{13} ions/cm²) is shown Fig. 5.29 with the average coercivity value around 24.41 mT. The magnetization vs. temperature (ZFC and FC) mode and magnetic field dependence of magnetization (M-H) curves were recorded using Physical property measurement system (PPMS-EC2, Quantum design, USA) at the temperatures 10 K and 350 K. The M-H curve of FeSi_Ag13 at 10 K has been shown in the figure. The coercivity and remanence of the irradiated film has been found to be 72.1 Oe and 1.89 emu/cm³. The coercivity and remanence value at 10 K is higher than at 350 K. The M-T plot (ZFC and FC) at 300 Oe showed a distinct peak which may be related to Verwey transition (~ 48 K) of magnetite phase due to high energy ion irradiation on the hematite films. The detailed analysis and draft making are under process.

References:

1. W. Eerenstein, N. D. Mathur and J. F. Scott, *Nature* **442**, 759 (2006).
2. V. Sahoo, R. N. Bhowmik and S. A. Khan, *Mater. Chem. Phys.* **296**, 127298 (2023).

5.2.17 Synthesis and confirmation of the Ge₂Sb₂Te₅-phase: Bulk and thin films

Puspender Singh Beniwal¹, Indra Sulania², Sanjay Kumar Kedia², G.R. Umapathy², Sunil Ojha² and Yogita Batra¹

¹Department of Physics, J. C. Bose University of Science and Technology, YMCA, Faridabad 121006, India

²Inter-University Accelerator Centre, Aruna Asaf Ali Marg, New Delhi 110067, India

Ge₂Sb₂Te₅ (GST) is a ternary compound composed of germanium, antimony, and tellurium alloyed in 2, 2, and 5 atomic ratios, respectively. It belongs to the chalcogenide family and is used as a phase change material with great thermoelectric potential. When GST alloys are doped with certain elements, there is a significant change in the properties, making them suitable for different applications. For example, doping of arsenic (As) with varying concentrations improves the thermal stability of GST, the temperature at which the amorphous to crystalline phase transition occurs, and switching behaviour can also be altered in GST systems [1,2]. The melting point of GST- alloy is 600°C (873 K), and its crystallization temperature ranges from 100 to 150°C [3].

For this reason, GST is a very suitable material for energy harvesting as a thermoelectric. Electrical energy transformation in thermoelectric materials is determined by the thermoelectric figure of merit $ZT = S^2\sigma T/(\kappa_e + \kappa_{ph})$, where S , σ , κ_e , κ_{ph} , and T are the Seebeck coefficient, electrical conductivity, thermal conductivity, phononic component of thermal conductivity, and operating temperature respectively [4]. The thermoelectric performance, including the performance factor ($PF = S^2\sigma$) and ZT , can be improved by modifying carrier concentration through doping or alloying with aliovalent elements. These factors depend very much on the structure and phase of the material.

A solid-state reaction [5] was carried out by step heating to form the desired GST phase. Germanium, antimony, and tellurium powders were taken in an atomic ratio of 2:2:5 and weighed according to a weight percentage ratio of 1:1.68:4.40. The powders of approximately 99.9% purity were mixed and ground with the help of pestle mortar for 2 hours. The mixed powder was then sealed in quartz ampoules under a vacuum of order $10^{-5} - 10^{-6}$ bar. After breaking the ampoules, the ingots were powdered again. The hydraulic press was then used to form pellets of 1 cm diameter by applying pressure of 8.5 tons for approximately 1 minute. X-ray diffraction (XRD) analysis of these samples was done using 'Bruker D8- Advance diffractometer'. The phase formed for these synthesized samples studied through XRD analysis (Fig. 5.30(a)) was found

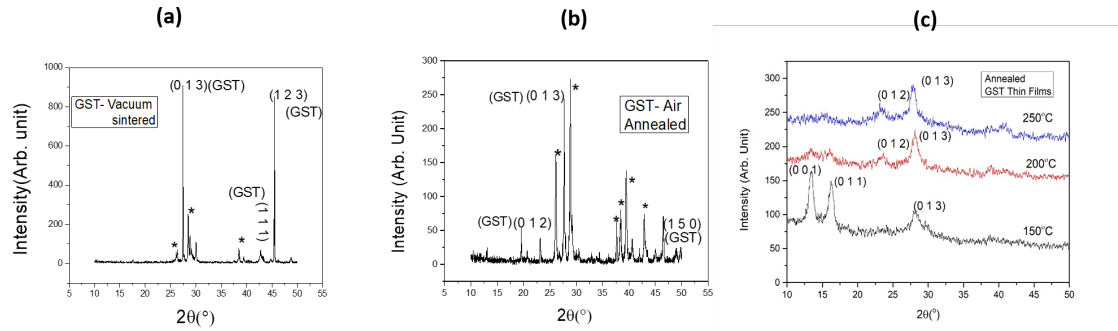


Figure 5.30: (a) XRD Pattern of GST pellet sintered at $10^{-2} - 10^{-3}$ bar. (b) XRD Pattern of GST pellet annealed in air (* represents the planes corresponding to oxides of GST), (c) XRD Pattern of annealed GST thin films.

to be GST-225. The XRD analysis validates the change in the crystallinity with an increase in annealing temperature for the samples. The peak intensity of XRD plots for these sets of samples tells us about the quality of the GST phase. Increased intensity and less FWHM of the XRD peaks (as shown in Fig. 5.30(b)) for the GST phase justifies the increased crystallinity.

The thin film samples of GST were deposited over glass and silicon substrates using a DC magnetron sputtering system [6]. DC magnetron is used with an optimized pressure and temperature. A GST target of approximately 99.99% purity was used to obtain the thin film samples. XRD and Ultraviolet-visible-Near Infrared (UV-Vis-NIR) spectroscopy were used to characterize the bulk and thin film samples. Scanning electron microscopy (SEM) and energy-dispersive X-ray (EDAX) analyses were carried out to study the morphology and stoichiometry of the samples [7]. The composition and thickness of the deposited thin films were confirmed using Rutherford backscattering spectrometry (RBS) [8,9]. UV-Vis-NIR spectroscopy was performed using UV VIS NIR (UV-3600i Plus) Shimadzu. SSEM-EDAX was performed using EVO18 ZEISS. RBS measurements were performed using a 5SDH-1.7MV Tandem accelerator at PARAS (Pelletron Accelerator for RBS-AMS System) at IUAC. The energy of the He^+ beam used is 2 MeV. These studies confirmed the structure of GST as trigonal with hexagonal lattice. The composition of the obtained samples is validated by both EDAX and RBS analysis for both bulk and thin films. The as-deposited and annealed thin film thickness is calculated precisely by analyzing RBS data using SIMNRA. Sputtered GST thin films of 200 nm were annealed, showing a phase transition from amorphous to *fcc* at 150°C and then to *hcp* at 250°C . It can be seen from Fig. 5.30(c), which depicts the XRD peaks corresponding to these phases.

References:

1. M. V. E. Madhavan, M. Carignano, A. Kachmar and K. S. Sangunni, *Sci Rep.* **9**, 12985 (2019).
2. P. Singh, A. P. Singh and A. Thakur, *J. Mater. Sci. Mater. Electron.* **30**, 3604 (2019).
3. J. E. Boschker and R. Calarco, *Adv. Phys. X* **2**, 675 (2017).
4. S. H. Kang, V. Jella, S. V. N. Pammi, J. H. Eom, J. S. Choi, J. R. Jeong *et al.*, *Curr. Appl. Phys.* **17**, 744 (2017).
5. M. L. Meena, S. Som, C. -H. Lu, R. S. Badgoti *et al.*, *Met. Oxide-Based Heterostruct.*, Elsevier, p. 297 (2023).
6. F. Wang and J. Wu, *Mod. Ion Plat. Technol.*, Elsevier, p. 189 (2023).
7. J. D. Brock and M. Sutton, *Mater. Today* **11**, 52 (2008).
8. M. Mayer, *Rutherford Backscattering Spectrometry (RBS)*.
9. G. R. Umopathy, S. Ojha, K. Rani, M. Thakur *et al.*, *Proc. DAE-BRNS Symp. Nucl. Phys.* **61**, 1038 (2016).

5.2.18 Investigation of the effect of implantation of tetravalent ions on thermally evaporated iron oxide films

Divya Sherin G. T.¹, R. N. Bhowmik¹, A. Tripathi², R. C. Meena² and K. D. Devi²

¹Department of Physics, R. V. Nagar, Pondicherry University, Kalapet 605014, India

²Material Science Group, Inter-University Accelerator Centre, Aruna Asaf Ali Marg, Delhi 110067, India

The aim of our research was to tailor properties of corundum structured $\alpha\text{-Fe}_2\text{O}_3$ (hematite) by doping tetravalent ions (Ge, Si) [1-2]. The FE-SEM images and EDX spectra Ge-doped hematite samples were recorded from Material Science division, IUAC. The results were published in the session 2023-2024 [2]. The thin film deposition by thermal evaporation method was carried out at IUAC during academic session

5. RESEARCH ACTIVITIES

2021-2022. RBS measurements of hematite films were recorded at Pelletron accelerator RBS-AMS systems at IUAC during 2022-2023. Ion beam implantation was performed at the Negative ion beam facility (NIBF), IUAC in session 2023-2024. The effect of low energy implantation of ions (^{28}Si : 65 keV, ^{74}Ge : 140 keV, ^{47}Ti : 100 keV, 16O: 40 keV) at about 50 nm depth within iron oxide films at various fluences has been analyzed.

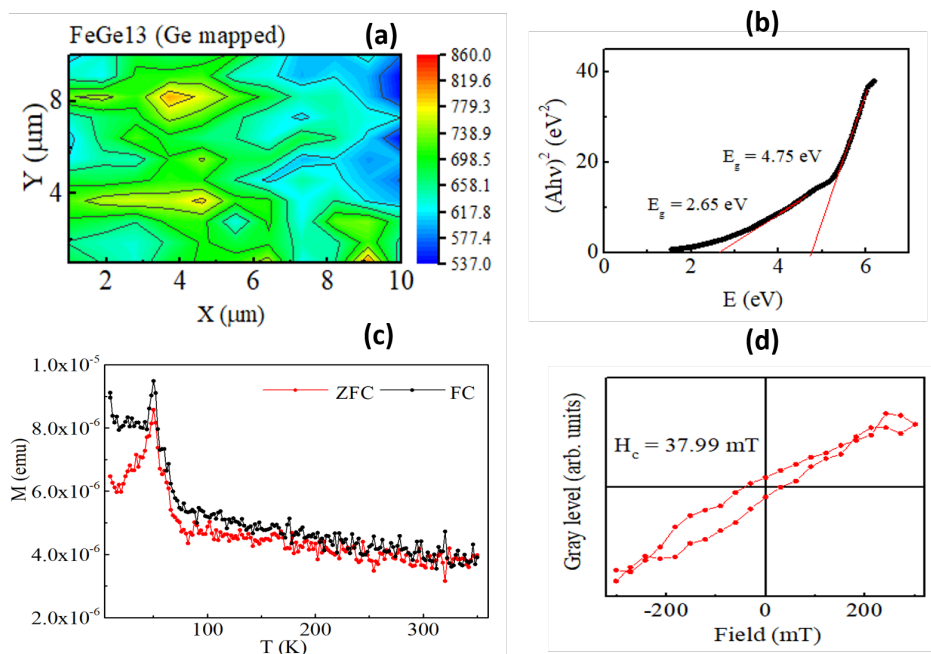


Figure 5.31: (a) Raman mapping of FeGe13 film showing almost uniform implantation of Ge on the surface of iron oxide. (b) Direct band gap of FeGe13 film. (c) Temperature-dependent curves of FeGe13 film. (d) MOKE image recorded for the film within a field range of ± 300 mT.

The structural, optical and magnetic properties of the Ge implanted films were characterized using Raman spectroscopy, UV-visible spectroscopy, L-MOKE and physical property measurement system (PPMS-EC2, Quantum design, USA). Fig. 5.31 shows results of iron oxide film implanted by Ge ions at low fluence (1×10^{13} ions/cm²), indicated as FeGe13. Fig. 5.31(a) shows the mapping of Ge ions which are distributed within a depth of 50 nm within the FeGe13 film (the 785 nm laser has a penetration depth upto ~ 12 μm). The UV-visible spectrum (Fig. 5.31(b)) showed two optical absorptions around 2.65 eV and 4.75 eV. The band gap (E_g) at the lower energy side corresponds from α -Fe₂O₃ while that on the higher energy side could be due to the effect of the implanted Ge ions into iron oxide [2]. We observed the variation of E_g values as 2.65 eV, 2.70 eV, 2.40 eV and 2.43 eV on increasing the ion fluence, i.e., 10^{13} ions/cm², 10^{14} ions/cm², 10^{15} ions/cm², 10^{16} ions/cm², respectively. The temperature dependent magnetization curves (ZFC and FC) in Fig. 5.31(c) show distinct peak around 50 K arises from trapped oxygen in the films and it could be coincided with freezing temperature of the spin moments. Surface magnetization from L-MOKE (Fig. 5.31(d)) shows non-saturating narrow loops in ion implanted films, providing coercivity (H_c) values of 37.9 mT, 16.8 mT and 24.5 mT for fluences 10^{13} ions/cm², 10^{14} ions/cm², and 10^{16} ions/cm², respectively.

References:

1. Y. Peng, Q. Ruan, C. H. Lam, F. Meng *et al.*, J. Alloys Compd. **870**, 159376 (2021).
2. Divya Sherin G. T. and R. N. Bhowmik, Mater. Sci. Semicond. Process. **170**, 107949 (2024).

5.2.19 Photovoltaic efficiency enhancement via ion beam

Sanjeev Gautam, Monika Verma and Ram Charan Meena

¹Advanced Functional Materials Lab., Dr. S. S. Bhatnagar University Institute of Chemical Engineering & Technology, Panjab University, Chandigarh, 160014, India

²Energy Research Centre, Panjab University, Chandigarh 160014, India

³Materials Science Division, Inter-University Accelerator Centre, New Delhi 110067, India

The efficiency of photovoltaic cells has long been a subject of intense concern and research. Diverse photovoltaic cell types have been developed, including crystalline silicon cells (achieving up to 27.6% efficiency), multijunction cells (reaching up to 47.4% efficiency), thin film cells (attaining up to 23.6% efficiency), and emerging photovoltaic cells (exhibiting up to 33.7% efficiency). Despite advancements, achieving high efficiency on an industrial scale remains a significant challenge due to factors like charge carrier recombination rate, defects, temperature's influence, etc. Numerous approaches have been explored to address these challenges, encompassing strategies such as incorporation of nanoparticles within the active layer, studying transport properties and defects using ion beams, utilizing magnetite materials, and leveraging the application of magnetic fields. The influence of a magnetic field can amplify the generation of charge transfer states exhibiting triplet characteristics, increasing the charge separation time. However, magnetic fields introduce spin-based effects, enabling the investigation of interactions between electron spins and magnetic fields through state-of-the-art synchrotron radiation techniques like XMCD. Several innovative cell configurations have reported substantial efficiency enhancements under the influence of magnetic fields. Examples include $\text{TiO}_2\text{-BiFeO}_3$ dye-sensitized cells, polymer-based cells with $\text{Fe}_3\text{O}_4\text{@PANI}$ additives integrated into TiO_2 -based dye-sensitized cells, and the incorporation of Fe-doped SnO_2 within the active layer of heterojunction organic solar cells (for details see [1]). In this perspective review, the profound impact of magnetism on enhancing efficiency in photovoltaic cells has been analyzed, and the utilization of advanced X-ray absorption spectroscopic techniques to probe and comprehend these intricate effects.

The use of ion beams can alter the transport processes in commercially available silicon solar cells to enhance their efficiency. Ion beams can also be used alternately in the fabrication process of solar cells, and further, ion beam irradiation (SHI) can be employed to produce defects. These defects could act as trap centers that restrict electron-hole pair recombination, thereby increasing the photocurrent and simultaneously enhancing efficiency. Therefore, ion-beam technology (both low and high energy) could be utilized to understand the fabrication and efficiency enhancement phenomenon. In this direction, ion implantation beam time has been executed and characterization is in progress.

References:

1. Monika Verma and Sanjeev Gautam, *J. Magn. Magn. Mater.* **588**, 171436 (2023).

5.2.20 Tuning of electrical properties through field effects for manganite based n-n junctions: Role of swift heavy ion irradiation

Mayur Parmar¹, P. S. Solanki¹, Ambuj Tripathi² and N. A. Shah¹

¹Department of Physics, Saurashtra University, Rajkot 360005, Gujarat, India

²Inter-University Accelerator Centre, Aruna Asaf Ali Marg, New Delhi 110067, India

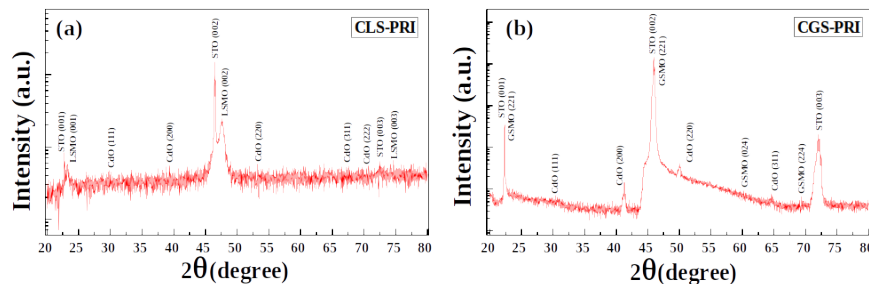


Figure 5.32: XRD patterns of (a) CLS-PRI, and (b) CGS-PRI thin film samples.

In order to investigate the modification in the electrical properties of manganite-based n-n junctions, previously the two different series of n-n junctions (i) CLS series: CdO (50 nm) // LSMO (100 nm) // STO and (ii) CGS series: CdO (50 nm) // GSMO (100 nm) // STO were prepared using the low-cost spin coating-based chemical solution deposition (CSD) technique [1]. For the pristine samples of the CLS series (CLS-PRI) and CGS series (CGS-PRI), the prepared thin films underwent many characterizations, wherein the structural properties were investigated using the x-ray diffraction method wherein, it can be observed from the x-ray patterns that the sample possesses a polycrystalline single-phasic nature without any external

5. RESEARCH ACTIVITIES

unwanted impurities which is depicted in Fig. 5.32(a) and Fig. 5.32(b) where it shows x-ray peaks of both well prepared films as well as substrates with miller indices [2].

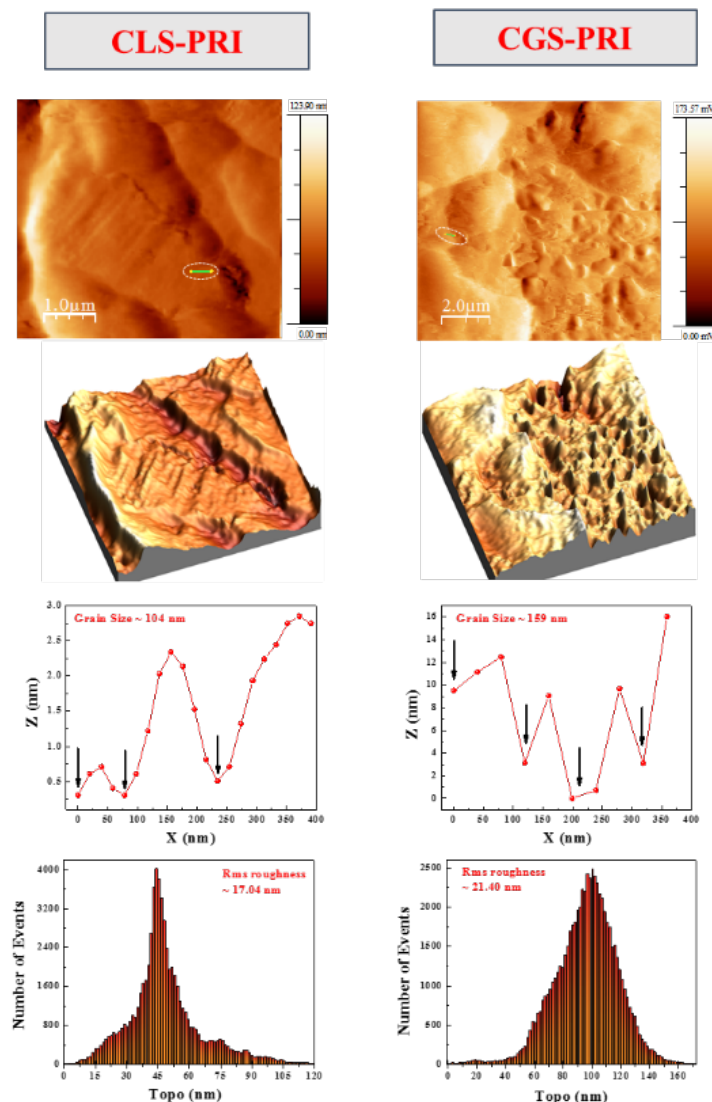


Figure 5.33: (i) 2D view with z-axis bars, (ii) 3D view, (iii) surface granular profiles with grain size and (iv) average rms roughness.

For understanding the granular morphology of the sample, the microstructural characterization were performed using the atomic force microscopy (AFM) measurements for both CLS and CGS series pristine samples, which were replicated here in Fig. 5.33(a) and (b), wherein it can be clearly observed that the CLS-PRI sample possesses a grain size of 104 nm, whereas the RMS surface roughness is 17.04 nm, and for the CGS-PRI sample, the observed grain size is 21.40 nm. From the findings of AFM measurements, Fig. 5.33 shows that the film's compactness is high with the batter grain distributions throughout the films.

Firstly, the modification in the electrical properties of CLS-PRI was understood at different excitation frequencies of (a) 10 K and (b) 100 K in the application of light and dark modes, as shown in Fig. 5.34 (a) and (b), wherein significant modifications were observed in both samples. The further analysis of the structural, microstructural, and electrical properties of the CLS-PRI sample is under way.

In the upcoming sanctioned year of the research project, now the main focused area is to irradiate the CLS and CGS series samples in the application of swift heavy ion (SHI) irradiation using 200 MeV energy Ag+15 ions with different ion fluence of i.e., 1×10^{11} ions/cm², 1×10^{12} ions/cm² and 1×10^{13} ions/cm² which were are further characterized by tuning different electrical properties. The characterized data will be further analyzed followed by communication of the manuscript to the international journals.

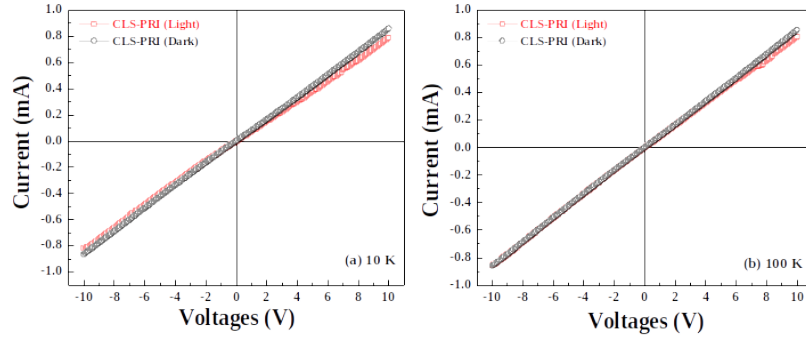


Figure 5.34: current-voltage characteristics of CLS-PRI sample at different excitation frequencies of (a) 10 K and (b) 100 K.

References:

1. D. Venkateshwarlu, Himanshu Dadhich, Bhargav Rajyaguru *et al.*, *Mater. Sci. Semicond. Process.* **136**, 106154 (2021).
2. Supriya Priyadarshinee, Jayashree Pati, Ranjita Mahapatra *et al.*, *J. Supercond. Nov. Magn.* **37**, 139 (2024) .

5.2.21 Studying the impact of swift heavy ion on exfoliated, nanoscale SnS

Stuti Tamuli¹, D. Mohanta¹ and Furan Singh²

¹*Nanoscience and Soft-Matter Laboratory, Deptt. of Physics, Tezpur University, Napaam, Tezpur 784028, India*

²*Materials Science Group, Inter-University Accelerator Center, New Delhi 110067, India*

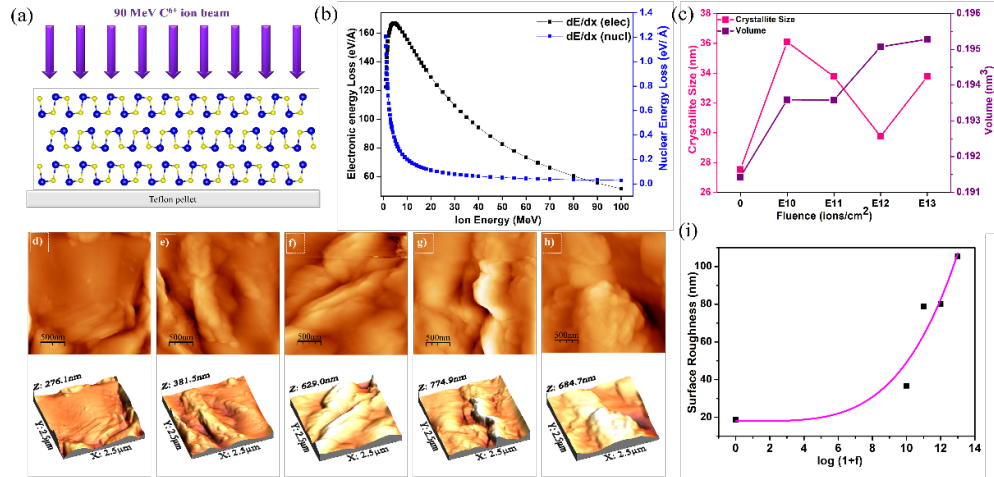


Figure 5.35: (a) Schematic diagram illustrating SHI irradiation of SnS material with 90 MeV carbon ions, (b) graph showing the variation in electronic (S_e) and nuclear energy (S_n) losses obtained from SRIM software, (c) variation of average crystallite size and unit cell volume with increasing ion fluence, (d-h) AFM images depicting (d) pristine and irradiated exfoliated SnS at fluences of (e) 1×10^{10} , (f) 1×10^{11} , (g) 1×10^{12} , and (h) 1×10^{13} ions/cm², (i) plot of surface roughness vs. $\log(1+f)$, where f is actual fluence.

With their layered structure and exceptional properties, group IV-VI metal monochalcogenides (MMCs) have gained prominence as one of the technologically important two-dimensional (2D) materials, distinguished by their earth-abundant nature, affordability, and environment-friendly attributes [1]. Among these notable MMCs, tin sulfide (SnS) stands out. SnS is natively a p-type semiconductor with an orthorhombic crystal structure and 1:1 stoichiometry. Its unique puckered structure, in-plane anisotropy and tunable band gap render it attractive for desired applications [2].

5. RESEARCH ACTIVITIES

Here, we have explored the swift heavy ion (SHI) irradiation-induced modifications on the tin sulfide (SnS) system. The SnS nanosheets were synthesized via a convenient, and user-friendly liquid-phase exfoliation process. Firstly, SnS powder was mixed with 2-propanol (IPA) at 1 mg/ml. The solution was ultrasonicated in a bath sonicator for 8 h, followed by high-speed centrifugation (~ 6000 rpm, 15 min) and then washed thoroughly with deionized (DI) water before oven drying at a temperature of 50°C , up to 12 h. To facilitate irradiation, the dried SnS powder was carefully dispersed onto a circular teflon pellet firmly compressed onto the surface with the help of a hydraulic press to ensure a uniform sample. The irradiation was carried out using a 90 MeV C^{6+} ion beam with a current of 1 pA at the 15 UD pelletron accelerator at IUAC, New Delhi as shown in Fig. 5.35(a). Four different fluences (1×10^{10} , 1×10^{11} , 1×10^{12} , and 1×10^{13} ions/ cm^2) were employed for the irradiation purposes. The SRIM simulation as shown in Fig. 5.35(b) revealed an electronic energy loss (S_e) of $55.53 \text{ eV}/\text{\AA}$, nuclear energy loss (S_n) of $3.07 \times 10^{-2} \text{ eV}/\text{\AA}$ and determined the projectile range of the carbon ion inside the SnS material to be $103.54 \mu\text{m}$.

The structural evaluation of both pristine and irradiated samples was conducted using X-ray diffraction (XRD). Notably, the crystallite size of the irradiated samples exhibited an increase compared to the pristine system as displayed in Fig. 5.35(c). Raman analysis revealed structural modifications in the SnS nanosystem upon ion irradiation, with higher fluences leading to amorphization. Morphological changes in the SnS samples due to ion irradiation were examined through atomic force microscopy (AFM) as shown in Fig. 5.35(d-h). The root mean square (RMS) roughness displayed an increase corresponding to ion fluence (Fig. 5.35(i)). SHI irradiation also prompted a non-linear rise in the electrical conductivity for both pristine and irradiated samples.

References:

1. A. S. Sarkar and E. Stratakis, *Adv Sci.* **7**, 2001655 (2020).
2. N. Koteeswara Reddy, M. Devika and E. S. R. Gopal, *Crit. Rev. Solid State Mater. Sci.* **40**, 359 (2015).

5.2.22 Growth and characterization of L-malic acid and Guanidine Carbonate based NLO single crystals

B. Sivasankari¹, Indra Sulania², S. Jayanthi¹ and D. Lakshmi Piriya¹

¹*Department of Physics, The Standard Fireworks Rajaratnam College For Women, Sivakasi, Tamil Nadu 626123, India*

²*Inter-University Accelerator Center, New Delhi 110067, India*

The samples studied in the present work are single crystals of Guanidine Carbonate incorporated Urea (GU), Succinic Acid incorporated L-Malic acid (SL), and Zinc Sulphate incorporated TrisThiourea (ZTS). The above crystals were grown at room temperature by solution method with a slow evaporation technique using double distilled water as the solvent [1-6].

Good quality crystals were selected and subjected to various studies like Fourier Transform Infrared (FTIR) Spectroscopy, UV Visible Spectroscopy, Dielectric Studies, Single Crystal XRD, Powdered XRD, and Second Harmonic Generation (SHG). The results obtained from the studies are as follows:

1) The functional groups present in the grown crystal samples GU, SL, and ZTS were examined with the help of FTIR study using IR Tracer – 100 SCHIMADZU in the frequency range between $4000 - 400 \text{ cm}^{-1}$.

2) The absorption and transmittance spectra of all the grown crystal samples were analyzed using UV Visible Spectrophotometer in the wavelength range between $200 - 800 \text{ nm}$. From this study, it was noted that the transparency of all the grown crystals was above 90% and it matches the requirement of optical devices. Using Tauc's plot (Fig. 5.36(c)), the optical band gap (E_g) was evaluated by the extrapolation of the linear part to the x-axis. The obtained band gap values for GU, SL, and ZTS single crystals are 5.9 eV, 4.3 eV, and 4.9 eV respectively. These wide band gap values show that the grown crystals can be used for optoelectronic applications.

3) The frequency-dependent dielectric parameters such as dielectric constant (ϵ_r), dielectric loss ($\tan \delta$), and the A.C. Conductivity (σ_{ac}) were examined for all the crystals using an LCR meter. It is observed that for all the grown crystal samples there is a high value of dielectric constant (ϵ_r) in the lower frequency region, which may be due to the space charge polarization. The low value of dielectric loss at a higher frequency is also noted for all the samples which reveals that the crystals are less defective, which qualifies these crystals to be used for the fabrication of NLO (Non-Linear Optical) devices. The higher value of A.C. Conductivity (σ_{ac}) is also noted in the higher frequency region for all these single crystal samples.

4) To identify the structure of these crystals and to observe the changes in the lattice parameters, X-ray diffraction analysis for all the crystals was carried out. The results show that GU has the crystal structure

as TETRAGONAL ($a = 6.9622$, $b = 6.9622$ and $c = 19.648$; $\alpha = 90^\circ$, $\beta = 90^\circ$ and $\gamma = 90^\circ$), ZTS has the ORTHORHOMBIC structure ($a = 11.178$, $b = 7.765$ and $c = 15.594$; $\alpha = 90^\circ$, $\beta = 90^\circ$ and $\gamma = 90^\circ$) and SL crystals has the TRIGONAL structure.

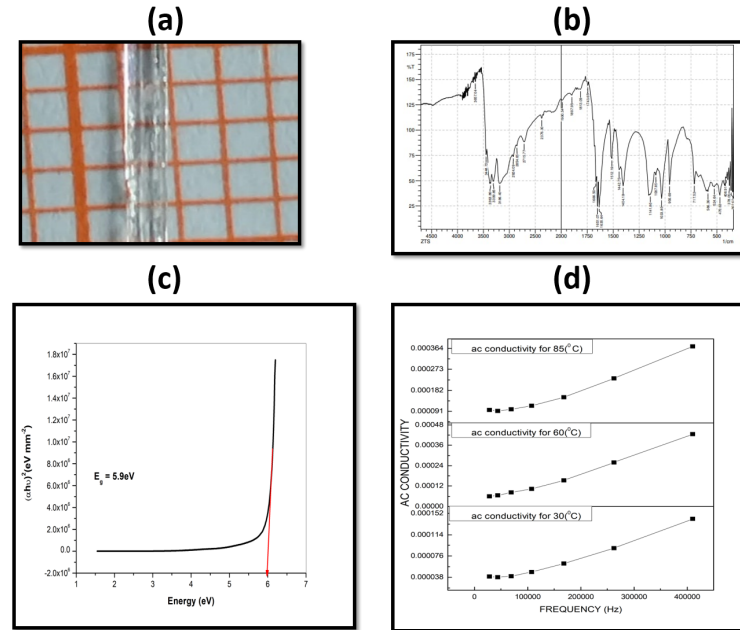


Figure 5.36: (a) Single crystal of SL, (b) FTIR spectra of ZTS single crystal, (c) Tauc's plot of GU single crystal, (d) AC conductivity of GU single crystal.

5) NLO properties of all the samples were studied as the major involvement of NLO materials in different technological applications, especially in photonics, telecommunications, laser technology, and in optical computing. From these studies, GU and ZTS are found to be non-centrosymmetric, so they may show Second Harmonic Generation (SHG), an NLO property. The SHG efficiency of ZTS single crystal was confirmed with an output of 2.3 mJ for an input of 0.50 mJ and it is compared with KDP (Potassium Dihydrogen Phosphate) also. However, the crystal of SL has a TRIGONAL and centrosymmetric structure, indicating that it may exhibit third-order harmonic generation (THG). Thus all the crystals grown in this study satisfy the usage as optical devices. All these studies on the above single crystal samples are complete and ready for exposure to irradiation in IUAC.

References:

1. B. Deepa and P. Philominathan, *Optik* **127**, 1507 (2016).
2. K. Krishnaraj, N. Sivakumar and P. Praveen Kumar, *Bull. Mater. Sci.* **43**, 41 (2020).
3. B. Sivasankari and P. Selvarajan, *Optik* **226**, 165909 (2021).
4. A. Venkatesan, S. Arulmani, E. Chinnasamy, S. Senthil *et al.*, *Mech. Mater. Sci. Eng.*, ISSN 2412-5954 (2017).
5. B. Sivasankari and P. Selvarajan, *J. Exp. Sci.*, 01-03 (2010).
6. B. Sivasankari and S. MohanaRoopan, *Optik, Int. J. Light Electron Opt.* **226**, 165909 (2021).

5.2.23 Swift heavy ion induced modification at the Si/SiO₂ interface of MOS devices at different gate biasing conditions

Arshiya Anjum¹, Darshan M.¹, Pushpa N.², Meena R. C.³, Ambuj Tripathi³ and Gnana Prakash A. P.¹

¹Department of of Studies in Physics, University of Mysore, Manasagangothri, Mysore 570006, India

²Department of PG Studies in Physics, JSS College, Ooty Road, Mysore 570025, India

³Inter-University Accelerator Centre, Aruna Asaf Ali Marg, New Delhi 110067, India

The P-channel and N-channel MOSFETs have been proven to be efficient in measuring the radiation dose in several applications like space radiation monitoring, medical radiotherapy and nuclear physics experiments [1]. The sensing principle of the MOSFET dosimeters is based on the generation of radiation-induced electron-hole pairs in the SiO₂ layer of the MOSFETs which produces additional oxide traps (ΔN_{ot}) and

5. RESEARCH ACTIVITIES

interface traps (ΔN_{it}) in the SiO_2 and SiO_2/Si interface of the MOSFETs respectively which causes the shift in threshold voltage (ΔV_{th}). Hence, the sensitivity of the radiation-sensitive field effect transistors (RADFETs) can be defined as the shift induced in the V_{th} due to the absorbed radiation dose [1]. The sensitivity of these MOSFETs to high energy radiations is greatly dependent on the bias voltage applied during the irradiation, and they too can modify the overall charge-dependent properties of MOS devices [2]. Therefore, it is very interesting and essential to study the gate polarization effects on MOSFETs during irradiation.

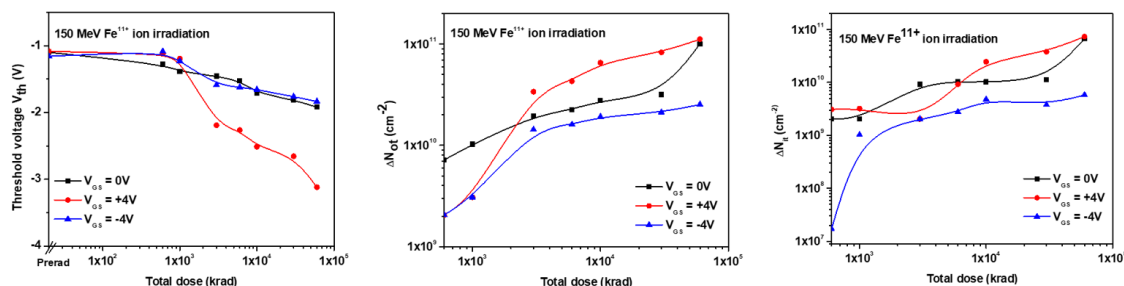


Figure 5.37: (Left) Variation in V_{th} of 150 MeV Fe^{11+} ion irradiated MOSFET at different V_{GS} , (middle) Variation in ΔN_{ot} of 150 MeV Fe^{11+} ion irradiated MOSFET at different V_{GS} and (right) Variation in ΔN_{it} of 150 MeV Fe^{11+} ion irradiated MOSFET at different V_{GS} .

The 150 MeV Iron ion (Fe^{11+}) irradiation was carried out at IUAC. The devices were irradiated with different gate biases ($V_{GS} = -4, 0$ and $+4$ V) at room temperature. The irradiation experiments were conducted at different radiation fluences ranging from 1.3×10^9 to 1.3×10^{11} Fe^{11+} ions/ cm^2 with different gate biases as mentioned above. The corresponding equivalent dose is 600 krad to 60 Mrad and the beam current was of the order of 0.1 pA. The electrical characterizations were done before and after irradiation at 300 K using Keithley dual source meter 2636A. The electrical characteristics of MOSFET such as threshold voltage (V_{th}), density of oxide trapped charges (ΔN_{ot}), density of interface trapped charges (ΔN_{it}), transconductance (g_m), mobility (μ) and leakage current (I_L) were studied as a function of the total dose at different V_{GS} . These parameters were extracted from the charge separation technique proposed by McWhorter and Winkur using the subthreshold measurements [3]. The obtained results were compared with the different biasing voltages applied during irradiation. Left panel of Fig. 5.37 depicts the variation in V_{th} with respect to total dose for 150 MeV Fe^{11+} ions irradiated MOSFETs at different V_{GS} . It can be observed from the figure that the shift in V_{th} is more for MOSFET irradiated at $V_{GS} = +4$ V. The middle and the left panels of Fig. 5.37 represent the change in ΔN_{ot} and ΔN_{it} produced in the device as a function of total dose at different V_{GS} . It can also be seen from the figures that the increase in ΔN_{ot} is comparatively higher than ΔN_{it} of the irradiated MOSFETs. It can also be seen from the figures that ΔN_{it} and ΔN_{ot} increased significantly after ion irradiations at different gate biases. However, the increase in ΔN_{it} and ΔN_{ot} is more for the MOSFETs irradiated at $V_{GS} = +4$ V. This is because when the gate is positively biased, the radiation-induced electron-hole pairs can not recombine and results in the large amount of charge yield. Thus, positive bias applied to the gate during irradiation enhances the degradation in the electrical characteristics of MOSFETs.

References:

1. E. Yilmaz *et al.*, Applied Radiation and Isotopes **127**, 156 (2017).
2. A. P. Gnana Prakash *et al.*, Ind. J. Phys. **78**, 1187 (2004).
3. P. J. Mc Whorter and P. S. Winkur, Appl. Phys. Lett. **48**, 133 (1986).

5.2.24 Ion-beam irradiation induced modifications in functional properties of chiral liquid crystals and their applications in fabrication of ultrasensitive chip based optical sensors

Satyabratt Pandey¹, Rohit Verma² and Sachin Kumar Singh¹

¹Department of Chemistry, DDU Gorakhpur University, Gorakhpur 273009, India

²Department of Applied Physics, Amity Institute of Applied Sciences, Amity University, Noida 201313, India

In order to incorporate liquid crystallinity into the aroylhydrazone moiety- a well-known core renowned for its high liquid crystalline capabilities, promesogenic groups (mono-, di- and tri-alkoxyester derivatives)

and their hydrazide analogues were initially designed, synthesized and characterized. Further condensation resulted in the successful synthesis of liquid crystalline ligands. The coordination of these ligands with Nickel(II) and Boron fluorides (BF₂) led to the formation of metallomesogens (metal-containing liquid crystals) suitable LCs for sensing applications. Three analogue series of liquid crystals, namely SP1, SP2 and SP3, were synthesized to investigate the influence of terminal substituents on liquid crystallinity, varying in terms of the number, length, and position of the alkoxy chains.

The molecular structures of all newly synthesized molecules were characterized by spectroscopic techniques (¹H and ¹³C NMR, IR, Raman etc) at BHU, Varanasi. The mesophase (liquid crystal) properties of the series were identified and analyzed using polarizing optical microscopy (POM) at DDU Gorakhpur University. The transition from the calamitic nematic phase to the Smectic (SmC) mesophase was observed in the first series (SP1) with variations in alkoxy chain length, while the SP3 series with tri-alkoxy chains exhibited a clearly visible targeted columnar mesophase under POM studies. Furthermore, the introduction of Nickel(II) and Boron fluorides (BF₂) complexes improved the mesogenic properties of the designed ligands in terms of clearing temperature.

To optimize the fabrication technique, newly synthesized amphiphilic potassium N-dodecyl aminedithiocarbamate (DTC) derivatives were utilized, doped in 4-cyano-4'-pentyl biphenyl (5CB) liquid crystal, aligning liquid crystal molecules at the aqueous interface observed under POM investigations. The application of the fabricated sensor system was screened under heavy metal ion-contaminated aqueous solutions under a cross polarizer, revealing transient shifts from dark to bright transitions of liquid crystals. The limit of detection (LOD) of the system was determined to be in the micromolar concentration range with very high selectivity towards target. Additionally, we demonstrated that this sensor is capable of detecting heavy metal ions in real water samples (tap water) too.

Hence, we have successfully designed columnar LCs and established fabrication techniques for LC-chip-based sensors. To study the effect of ion-beam irradiation-induced modification of the designed LC for chip-based sensors, we will utilize facilities at IUAC, New Delhi.

References:

1. S. Pandey, R. Verma, A. Tripathi and S. K. Singh, Fabrication of liquid crystal based sensor system for the detection of mercuric ions in real water samples using amphiphilic probes (to be reported).

5.3 AMS and geochronology

5.3.1 Landscape evolutionary history under episodic domination of tectonic, climatic, and fluvial dynamics in the Thamirabarani Basin, Southern India

Athira. P¹, M. Ramkumar¹, K. Balasubramani², R. Nagarajan³ and V. Thirukumar⁴

¹Department of Geology, Periyar University, Salem, India

²Department of Geography, Central University of Tamil Nadu, Thiruvavur, India

³Department of Applied Geology, Curtin University, Miri, Sarawak, Malaysia

⁴Department of Geology, Govt. Arts College, Salem, India

River systems, through their actions together with other mechanisms and processes such as tectonic upliftment and subsidence, erosion, and deposition, modify the landscape on a variety of spatial and temporal scales. Coeval, and independently acting internal tectonic process deforms the lithosphere while external climate forcing shapes the surface topography resulting in a myriad variety of surficial expressions of the land. Understanding these processes and products on a basin scale plays an important role in the documentation and prediction of earth surface processes and helps in natural environmental management. River has an important role in the hydrosphere. It shapes the land by erosion and deposition. The evolution of landscape takes place due to five different mechanisms: they are upliftment, subsidence, deposition, erosion, and volcanism [1]. The Thamirabarani River originates from Pothigai hills which is situated in the eastern part of Western Ghats. The present study is an attempt to document and understand the spatial and temporal dynamics of landscape evolution in the Thamirabarani River Basin with the use of a variety of tools including, but not limited to geology, quantitative morphometry, soil and sediment texture, heavy mineral assemblage and their distribution, analyses of occurrences and distribution of paleosols, knickpoints, terraces and other proxies of climate, tectonics, erosional and depositional episodes of the past. When these data are integrated with relative and absolute chronological information, evaluating and disentangling the times and roles played by the dominant controls on a spatial scale could be deciphered [2].

5. RESEARCH ACTIVITIES

In this context, the collaboration of scientific personnel in the IUAC was sought for availing the sophisticated analyses for measurement of radiocarbon (^{14}C) and beryllium-10 (^{10}Be) isotopes—and optical luminescence data can yield important insights into the dynamics of sedimentation, erosion rates, and landscape change under the influences/controls of tectonics and climate. With these premises, stratigraphic occurrences of various types of paleosols located at different terraces and elevational sites are documented in the basin and are subjected to ^{14}C analysis in IUAC vide reference BTR No. 73248. According to the results obtained, we have delineated the radiocarbon ages (BP) from 22928 to 2428. Comprehensive analysis of granulometric, mineralogical, geochemical, heavy mineral and other data of these paleosols and river sediments are being conducted. Further, additional sample analyses for carbon isotopes and possible utilization of Be isotopic analytical facilities are being sought, as the mapped/sampled terraces and sample materials are beyond the precise chronological limits of radiocarbon dating and without the additional chronological data, the proposed landscape evolution model may not be complete, commensurate to qualify for international publication(s). Once complete, it is believed that a landscape evolutionary model along with differing roles of controls of intrinsic and extrinsic processes will be revealed.

References:

1. M. Ramkumar *et al.*, Geological Journal **5**, 2870 (2019).
2. Athira P. it et al., Indian Geographical Journal (submitted).

5.3.2 High resolution foraminiferal response to the climatically induced changes in the southeast Arabian Sea

Ajai Kumar Rai and Vishwesh Kumar Pathak

Department of Earth and Planetary Sciences, University of Allahabad, Prayagraj 211002, India

The present work is based on the benthic foraminiferal study of Gravity Core SK-221, GC-1 situated near the Laccadive-Chagos Ridge (Latitude 8.1187°N, Longitude 73.2730°E, Water Depth 2180 m) in the Southeastern Arabian Sea during last ~ 50 ka BP. Core samples are commonly taken at a regular interval of 1cm from top 1.0 m long section. To extract the foraminiferal tests larger than 125 μm size, we applied the wet sieving method, following standard micropaleontological procedures as outlined by Pathak et al. (2021). The available samples were treated with 10% Calgon solution for at least 24 hours. The material then wet sieved by Tyler sieves through 63 μm and 125 μm and then dried in oven at constant temperature. After drying > 125 μm fraction of samples were split into an aliquot containing more than 300 specimens of benthic foraminifera. All specimens were identified and counted. We have analysed 15 foraminiferal samples at IUAC for AMS ^{14}C dates. A total of 59 genera which included 108 benthic foraminiferal species were recorded from a total of 100 studied core samples. The relative abundance of several important taxa of foraminifera was determined using the data from the faunal census. The most dominant taxa recorded at this site are *Uvigerina proboscidea*, *Bulimina alazanensis*, *Bulimina aculeata*, *Globocassidulina subglobosa*, *Astrononion umbilicatum*, *Oridorsalis umbonatus*, *Cassidulina carinata*, *Cibicides wuellerstorfi*, *Nuttallides aff. umbonifera*, *Epistominella exigua* and unilocular forms. The Q-mode factor analysis of the reduced quantitative benthic foraminiferal abundance data extracted four distinct faunal assemblages reflecting different paleoceanographic conditions. The benthic foraminiferal census data was also used to measure various species diversity parameters to understand the biodiversity changes in the southeastern Arabian Sea during last ~ 50 ka BP.

The prominent occurrence of *Uvigerina proboscidea* assemblage prior to 40 ka BP indicates more surface productivity possibly due to intense upwelling during strong southwest summer monsoon. *Cassidulina carinata* assemblage during 30 to 15 ka BP along with higher abundance of *Bulimina aculeata*, *Cibicides wuellerstorfi* and *Cassidulina carinata* were possibly reflecting the northeast winter monsoon led convective deep sea mixing which also moderately increased the surface productivity. The dominant occurrence of *Globocassidulina subglobosa* assemblage during 15 to 12 ka BP along with the higher abundance of unilocular taxa and lower percentage of biogenic carbonate suggested moderately low trophic levels (oligotrophic) with relatively better oxygenation in the deep sea due to weaker monsoonal strength. *Bulimina alazanensis* assemblage during the period of 12 to 2 ka BP (Holocene) corresponds to the higher relative abundance of *Bulimina alazanensis*, *Nuttallides aff. umbonifera* and *Cibicides wuellerstorfi* along with higher percentages of biogenic carbonate and moderately low diversity. These changes were possibly due to enhanced surface water productivity in response to enhanced southwest summer monsoon however, deep sea at abyssal depths

in the southeastern Arabian Sea was also possibly influenced by the cold and well oxygenated subsurface waters from the southern source. In addition, the study of planktic foraminifera is also under process to gain better understanding of the surface water hydrographic changes in the southeastern Arabian Sea.

References:

1. Vishwesh Kumar Pathak, Ashish Kharwar and Ajai Kumar Rai, *J. Earth Sys. Sci.* **130**, 163 (2021).

5.3.3 Sedimentological and geochemical responses of lake sediments to climate changes in Southern India during the late Holocene.

A. S. Yamuna¹, Anish Kumar Warriar¹, Vyshnav P¹, Sandeep, K.², M. C. Manoj³, Rajveer Sharma⁴ and Ritesh Rao⁵

¹Centre for Climate Studies, Department of Civil Engineering, Manipal Institute of Technology, Manipal, Karnataka 576104, India

²Department of Geology, School of Earth Science Systems, Central University of Kerala, Kasaragod 671320, India

³Birbal Sahni Institute of Paleosciences, 53 University Road, Lucknow 226007, India

⁴Inter-University Accelerator Centre, Aruna Asaf Ali Marg, New Delhi 110067, India

⁵Department of Marine Geology, Mangalore University, Mangalagangothri 574199, Karnataka, India

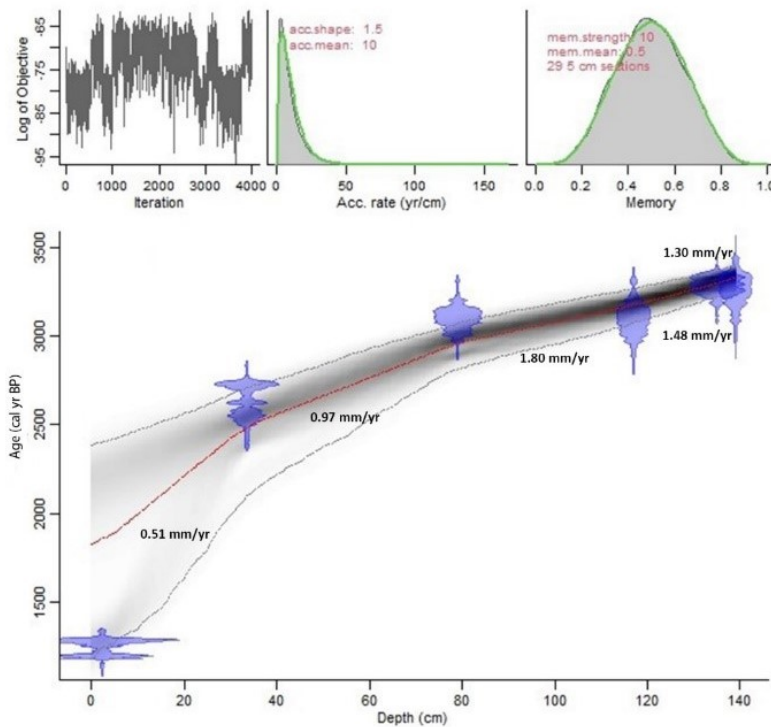


Figure 5.38: Age-depth model for SSB sediment core constructed using BACON.

In this study, we are trying to understand the intrinsic paleoenvironmental changes of southern India in the past 3300 years by investigating the dynamics of weathering and sedimentation processes in Lake Shantisagara, one of the largest lakes in Karnataka, through a high-resolution multiproxy study (geochronology, sediment geochemistry, sedimentology, and end member modelling analysis) in a 1.4 m long sediment core. Radiocarbon dating of the SSB sediment core using accelerator mass spectrometry (AMS) was carried out on bulk sediment samples from six uniform depths. The AMS dating was done at IUAC. The ^{14}C ages were calibrated, and an age-depth model was obtained using Bacon (version 2.3.9) [1] running on 'R' (version 4.0.4) using the IntCal20 calibration curve [2]. The chronology for the entire core was obtained by linear interpolation. The sedimentation rate of the core was computed from the age-depth model.

The chronology of the SSB is provided by six ^{14}C dates. Details of the depths of the sediment samples used for dating, the radiocarbon ages, and their calibrated ages are given in Table 5.3. An age-depth model was constructed using six ^{14}C dates (Fig. 5.38). The age for the entire core was calculated by linear interpolation. The average sedimentation rate for the entire core is 1.14 mm/yr. The SSB sediment core spans for about 1500 yrs from 3331 to 1828 cal yr BP. The minimum sedimentation rate (0.51 mm/yr) is

5. RESEARCH ACTIVITIES

Table 5.3: AMS ^{14}C dates of the SSB sediment core.

Sl. no.	Sample name	Depth (cm)	^{14}C Age (BP)	Calibrated age range	Sedimentation rate (mm/yr)
1	SSB-1	2.25	1337 \pm 26	1828-1860	0.79
2	SSB-2	33.5	2561 \pm 41	1860-2483	0.51
3	SSB-3	79	2943 \pm 29	2483-2958	0.97
4	SSB-4	117	2940 \pm 47	2958-3176	1.80
5	SSB-5	135	3071 \pm 27	3176-3300	1.48
6	SSB-6	139	3064 \pm 57	3300-3331	1.30

obtained for the period between 1860 and 2483 cal yr BP (2.5-33.5 cm) and the maximum sedimentation rate (1.80 mm/yr) between 2958 and 3176 cal yr BP (79-117 cm).

References:

1. M. Blaauw and J. A. Christen, *International Society for Bayesian Analysis*, **6**, 457 (2011).
2. P. J. Reimer *et al.*, *Radiocarbon* **62**, 725 (2020).

5.3.4 Radiocarbon dating of sediment cores from Cauvery Delta: A study to understand climate and land use

Deepthi N. and Balasubramani K.

Department of Geography, Central University of Tamil Nadu

The present work was carried out with active support from the IUAC facility at New Delhi. Sediment samples were collected from the Cauvery delta region. The study was carried out to document and analyze the link between climate, land use and delta development from sediment archives for longer temporal scale. The samples were taken from the tidal flat in the Muthupet region, both surface and core samples were taken. Five samples were approved and the sample preparation was carried out at the AMS facility, IUAC. The data obtained is yet to be adapted into the thesis.

5.3.5 Pollutant assimilation and nutrient export dynamics of a tropical estuary: Vettar tributary of the Cauvery River system, Southern India

Deepthi N. and Balasubramani K.

Department of Geography, Central University of Tamil Nadu

The Vettar estuary is a microtidal, bar-built estuary with a tidal range of less than 2 meters. Estuaries worldwide serve as sites for effluent discharge from shipyards, harbours, petrochemical industries, aquaculture facilities, and extensive agriculture. The complex and dynamic interaction between fresh and saltwater, along with sediments, in estuarine environments necessitates understanding seasonal and spatial variations in physiochemical parameters as they form the basis for biological and chemical reactions. Pollution assimilation in estuarine water and sediments can lead to bioaccumulation and magnification within the food chain. This study aims to collect water samples and in-situ data in pre, post, and monsoon months. Data is collected both vertically (depth) and horizontally (spatially). Parameters such as salinity, total dissolved solids, dissolved oxygen, and temperature are measured in-situ, while water samples are subjected to trace element analysis.

The proposed research aims to create a comprehensive database on the current environmental status of Vettar estuary to improve our understanding on its pollutant assimilation capacity. The goal of this study is to provide an integrated solution for the conservation of environmental resources, aligning with wetland conservation goals and policies.

A total of 270 water samples for trace element analysis and the sediment samples were digested with microwave digester and the samples were analysed for trace and rare earth metals using ICP MS facility at IUAC and yet to be translated into manuscript.

5.3.6 Paleomonsoon and Paleoenvironment study using multi-proxy data from marine and lake archives

Anil Kumar Gupta¹, Biswajit Palar², Abhijeet Santra¹, Arpita Parhi¹, Puja Ghosh¹, Mainak Ghosh¹ and Pankaj Kumar³

¹Department of Geology and Geophysics, Indian Institute of Technology Kharagpur, Kharagpur 721302, India

²Centre for Ocean, River, Atmosphere and Land Sciences, Indian Institute of Technology Kharagpur, Kharagpur 721302, India

³Inter-University Accelerator Center, Aruna Asaf Ali Marg, New Delhi

The Indian Summer Monsoon (ISM) is a complex atmospheric phenomenon that depends on insolation, ocean circulation, and wind movements. In order to understand past variability and intensity of the ISM over the Indian sub-continent, sediment cores were collected from eleven lakes in Eastern and Northern India. Total fourteen cores of length 5.10 m, 3.5 m, 1.06 m, 1.36 m, 1.12 m, 4.88 m, 6.30 m, 5.11 m, 5.94 m, 5.02 m, 0.85 m, 0.35 m, 1.44 m and 0.38 m were obtained from Hansadanga, Nowpara, Sartola, Karajgram, Mathura Beel, Duma Baor and Panchita-Chanda lakes respectively, located in the Nadia, Burdwan and North 24 Pragana district of West Bengal. Six cores of length 7.17 m, 14.64 m, 9 m, 11.70 m, 7.8 m and 7.5 m were obtained from Chilika, Anshupa and Tampara lakes in Ganjam and Cuttack districts of Odisha using gravity and auger drilling method. Lake samples have also been collected recently from Sahaswan Lake, Budaun, Uttar Pradesh, with a total penetration of 2.15 m and 3.30 m. The samples are sub-sampled at 5 mm, 10 mm and 2 cm intervals. The age of the 80 approved samples (including bulk sediments, gastropods, and bivalvia) from different lakes and marine sediments was done at the AMS radiocarbon facility of IUAC. The samples were finely crushed using mortar and pestle and sieved to remove the detrital materials and plant roots. Afterward, sediment samples were pre-treated in the Graphitization laboratory of IUAC using acid-base-acid treatment, and the ages were determined using the techniques after Sharma *et al.*. Some coarse samples with low organic carbon concentrations are sent to WIHG, Dehradun, using the OSL dating method to determine OSL dates.

The West Bengal lakes are mostly oxbow lakes of the lower Ganga plain system, mainly formed in the Holocene epoch. Hence, these lakes are a good indicator of extreme events like floods and droughts and are also used for paleoclimatic study. Hansadanga Lake covers the age range of 12000 cal yr BP, whereas Karajgram has a bottom age of nearly 20000 cal yr BP. The Sartola and Mathura Beel lakes have the ages of 1339 cal yr BP and 1490 cal yr BP with a penetration of 287cm and 129 cm, respectively. The analysis of the bottom samples below the mentioned depth of the above two lakes may cover mid to lower Holocene. Radiocarbon dates of Chilika Lake sedimentary cores have provided an age range of nearly 25000 cal yr BP to the Recent, whereas the coastal lake Tampara goes up to 10000 cal yr BP. The Fluvial freshwater lake Anshupa provides an age range from 6200 cal yr BP to the Present. The radiocarbon age of these lakes records several climate events like the Dark Ages Cold Period (DACP), Medieval Climate Anomaly (MCA), Little Ice Age (LIA), 4.2 ka and 8.2 ka events, Younger Dryas, and many more.

To study the effects on benthic foraminifera due to gas hydrate occurrences along the Chilean margin, an age-depth model for the concerned site (ODP Leg 202 Site 1235A) was required. For the present study, the analysis was done at IUAC, from which age ranges up to 23000 years were obtained.

The grain size and XRF analyses of these lakes have been completed. Magnetic and biomarker analyses of some lakes have also been completed. Samples are prepared for other proxy records, including XRD, TOC, Pollen, and Stable isotope studies (*e.g.*, ¹³C), and analysis will be done soon to reconstruct the past climate and environments. We have approval for 85 samples for AMS dates, which will be done later at IUAC.

References:

1. J. Majumder *et al.*, Global and Planetary Change **234**, 104397 (2024).
2. R. Sharma *et al.*, Nucl. Instrum. Methods B **438**, 124 (2019).
3. A. Kaushik *et al.*, Palaeogeography, Palaeoclimatology, Palaeoecology **619**, 111544 (2023).
4. Sreya Sengupta *et al.*, The Holocene (accepted).

5.3.7 (BTR 73125) Constraining the Little Ice Age in the Western Himalaya

Rakesh Saini^{1,2}

(BTR 74211) Reconstruction of style and timing of the glacial fluctuations in the Chandrabhaga Basin, Lahaul Himalaya

Ganga Sagar Bhagat¹ and Rakesh Saini^{1,2}

5. RESEARCH ACTIVITIES

(BTR 74219) Reconstruction of palaeo and present glacial fluctuations in the Zaskar Basin through landform interpretation

Shubham Sahu¹ and Rakesh Saini^{1,2}

¹Department of Geography, Hemvati Nandan Bahuguna Garhwal University, Srinagar 246174, India

²Department of General and Applied Geography, Dr. Harisingh Gour Vishwavidyalaya, Sagar 470003, India

Under the BTR 73125, 74211 and 74219 the PI received approval of 10 samples each of ^{10}Be / ^{26}Al and ^{14}C for each BTR. As of now the PI have processed the chemically treatment for the 26 samples following the laboratory protocols for measuring ^{10}Be / ^{26}Al , however only 14 samples qualified for the AMS measurements (Table 5.4). These 14 samples are ready for AMS measurement and we are expecting the dates at the earliest whereas 30 soil samples were processed to measure the major and minor elements using x-ray fluorescence. Fig. 5.39 shows locations of the samples in the study area.

Table 5.4: Current status of CRN samples.

Sl.	Sample code	Name	Remarks	Status
1	GS-01	Bara.Shigri CRN-1	Ready for AMS	Complete anion and cation process
2	GS-02	Bara.Shigri CRN-2	Ready for AMS	Complete anion and cation process
3	GS-03	PDM CRN-1	Ready for AMS	Complete anion and cation process
4	GS-04	PDM CRN-2	Ready for AMS	Complete anion and cation process
5	GS-05	PDM CRN-3	Ready for AMS	Complete anion and cation process
6	GS-06	DRD-T CRN-1	Not sufficient amount	Dissolved during leaching process
7	GS-07	DRD-T CRN-2	Ready for AMS	Complete anion and cation process
8	GS-08	DRD CRN-1	Ready for AMS	Complete anion and cation process
9	GS-09	PAR CRN-1	Ready for AMS	Complete anion and cation process
10	GS-10	PAR CRN-2	Ready for AMS	Complete anion and cation process
11	GS-11	ZGT-1	Not applicable for AMS	Dissolved during leaching process
12	GS-12	ZGT-2	Not applicable for AMS	Dissolved during leaching process
13	GS-13	ZGF-1	Not applicable for AMS	Dissolved during leaching process
14	RS-I	Doksa CRN-1	Not sufficient amount	Dissolved during leaching process
15	RS-II	Miyar Holocene CRN-1	Ready for AMS	Complete anion and cation process
16	RS-III	Miyar LIA CRN-1	Not sufficient amount	Dissolved during leaching process
17	RS-IV	Miyar LIA CRN-1	Ready for AMS	Complete anion and cation process
18	RS-V	Gumba Strath CRN-1	Ready for AMS	Complete anion and cation process
19	RS-VI	Gumba Strath CRN-2	Not sufficient amount	Dissolved during leaching process
20	RS-VII	Tharang LIA CRN-1	Not sufficient amount	Dissolved during leaching process
21	RS-VIII*	Tharang LIA CRN-2	Ready for AMS	Complete anion and cation process
22	RS-IX	Tharang LIA CRN-3	Not sufficient amount	Dissolved during leaching process
23	RS-X	Tak LIA CRN-1	Not sufficient amount	Dissolved during leaching process
24	RS-XI	Tak LIA CRN-2	Not sufficient amount	Dissolved during leaching process
25	RS-XII	Takdung CRN-1	Not sufficient amount	Dissolved during leaching process
26	RS-XIII*	Takdung CRN-2	Ready for AMS	Complete anion and cation process

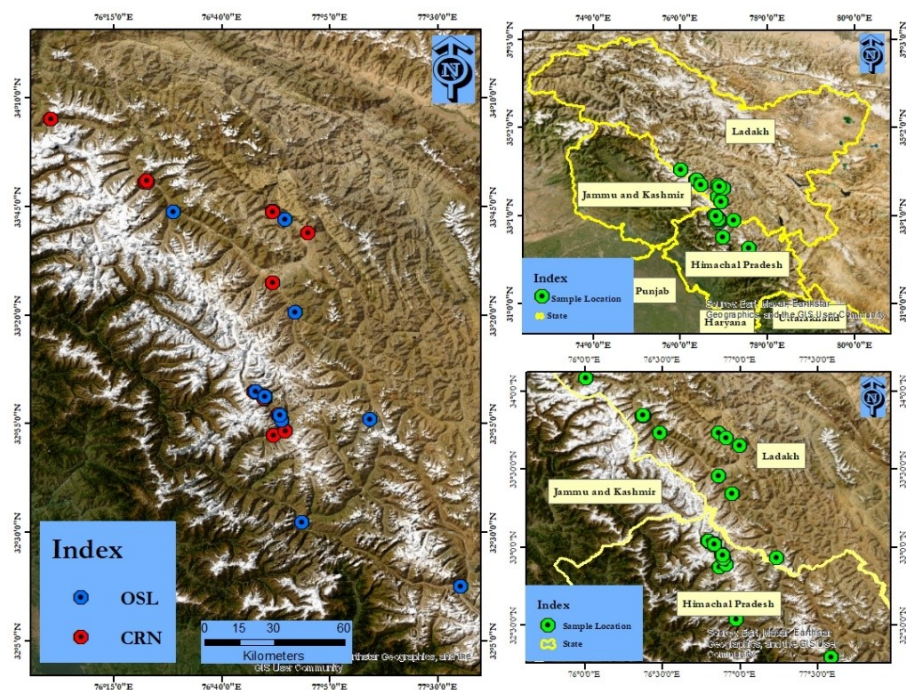


Figure 5.39: Locations of the samples in the study area.

5.3.8 Using past analogues to understand the role of fire and climate change in Central India

M. Agarwala¹ and C. Kulkarni²

¹*Department of Environmental Studies, Ashoka University, Sonapat 131029, India*

²*School of Sustainability, IIT Madras, Chennai 600036, India*

Analyzing long-term paleoecological records in conjunction with fire, temperature, and precipitation data, using spatially-explicit models and hypothesis testing [1] will help us understand the resilience of different species and plant traits to fire and climatic stressors as well as the positive feedback between fire and climate change. Ecological studies show that fire and seasonal drought are important drivers of functional traits in dry deciduous forests of Southern India [2], and our recent meta-analysis of 15 Central Indian paleo-sites finds that fire predicts low canopy cover in Central India across the Holocene [3].

Given the impending consequences of climate change, this study quantifies fire occurrence in two sites in Central India. According to our meta-analysis, one of the two sites shows switches between alternative stable states while the other maintains the same state [Biotropica, in review]. The AMS dating of the cores at IUAC show both cores to be >6 ka, with one spanning ~ 19 ka. Understanding long-term fire regimes will help to identify “natural” fire regimes in Central Indian forests, i.e. the threshold of fire frequency and intensity that would not alter the ecosystem, and aid in forest fire management in the region.

References:

1. D. J. Beerling and F. E. Mayle, *Global Change Biology* **12**, 1977 (2006).
2. J. Ratnam, S. K. Chengappa, S. J. Machado, N. Nataraj *et al.*, *Frontiers in Ecology and Evolution* **7**, 1 (2019).
3. M. Agarwala, K. Komanduri, M. F. Quamar, J. Ratnam and C. Kulkarni, *Biotropica* (in review).

5.3.9 Multi-proxy approach to palaeoclimate reconstruction by study of sediment cores from pristine lakes of Manipur NE, India

K. Ronald Terieng¹, Pramod Singh¹ and Pankaj Kumar²

¹*Dept. of Earth Sciences, School of Physical, Chemical & Applied Sciences, Pondicherry University, Puducherry 605014, India*

²*Inter-University Accelerator Centre, Aruna Asaf Ali Marg, New Delhi 110067, India*

Paleoclimate studies play a vital role in enhancing our understanding on climate variability and help in developing workable models for forecasting future climate as it has a direct link to the socio-economic stability of a region. Lake sediment deposits serve as prominent terrestrial archives and can be used in delineating past climate and monsoon variability. Using lacustrine archive, various proxies, such as geochemistry, mineralogy, texture, and stable isotope studies help decipher the region’s climate. Paleoclimate studies in the North Eastern Himalayan region are mostly based on limited proxies and therefore we are carrying out a multi-proxy study to better understand the past climate beyond instrumental records and also correlate with other parts of the country and the world. With regard to this, work has been initiated on two sediment cores from two pristine lakes of Manipur. One collected from the Zaimeng Lake located at Thonglang village, Kangpokpi District and another from the Zeilad Lake located in the Zeiladzung village of Tamenglong District. Thus, for the above purpose it becomes essential to find the chronology of the lake sediments for which ¹⁴C measurement procedures have been initiated at AMS facility at IUAC, New Delhi.

Field work was initially carried out to collect the sediments from the two lakes. The Samples from the Zaimeng Lake are collected by digging a trench of 90 cm depth from the dried part of the lake sub-sampled at 2 cm interval. However only up to 56 cm is taken for processing and analysis as samples below was part of bedrock. Sediment core of 72 cm length retrieved from Zeilad Lake was sub-sampled at 1 cm interval. All the above samples have been processed and geochemical analysis, C, N, texture, mineralogy and $\delta^{13}\text{C}$ measurements on these samples have been carried out at the Department of Earth Sciences, Pondicherry University. XRD facility at IUAC was utilized for clay mineral identification of 7 samples of the Zeilad Lake sediments. To obtain preliminary geochronology first batch of 11 samples were selected, 5 from the Zaimeng lake sediment core, 4 from Zeilad Lake Sediment core and 2 from Kadagathur Lake, Tamil Nadu (for correction of previously measured date) were sent to IUAC. All Samples were pretreated using acid-base-acid protocol in the graphitization laboratory of IUAC. Samples were subjected to graphitization after pre-treatment. An adequate amount of graphite could be obtained from all samples and were measured using AMS facility at IUAC for obtaining ¹⁴C dates. Out of the above, 7 dates obtained for Zaimeng Lake

5. RESEARCH ACTIVITIES

and Kadagathur Lake has given promising results and samples of Zeilad Lake have given younger ages. The Zaimeng Lake sediments show early to mid Holocene record whereas the Zeilad Lake sediments reveal a very recent record, up to ~ 300 yr B.P. Therefore, with aim to cover the mid to late Holocene climate record we have retrieved 3 more cores and samples from trenches from different lakes during our recently concluded field work from Manipur region. We plan to carry out ^{14}C measurement on these new sediment cores at AMS facility at IUAC.

References:

1. N. Mehrotra, S. K. Shah, and A. Bhattacharyya, *Quaternary international* **325**, 41 (2014).
2. O. Kumar, R. Devrani, and A. L. Ramanathan, *Journal of Climate Change* **3**, 11 (2017).
3. A. Yadav, B. Mehta, A. Anoop and P. K. Mishra, *Monsoon variability in the Indian subcontinent –A review based on proxy and observational datasets*, Editor(s): N. Kumaran and P. Damodara, *Holocene Climate Change and Environment*, Elsevier (2022), Pages 369-390.

5.3.10 Reconstructing human-fire-vegetation inter-relationships in a protected dry tropical forest, Mudumalai National Park, southern India

Prabhakaran Ramya Bala¹, Nithin Kumar¹ and Raman Sukumar²

¹*National Institute of Advanced Studies, Bengaluru, India*

²*Indian Institute of Science, Bengaluru, India*

Tropical dry forests are recognized globally as the first frontier of human land-use change, due to multiple factors that make them amenable to human occupation, especially with the use of fire. However, in southern India, biodiversity ‘hotspots’ with human habitation are not uncommon with a long-term co-existence of humans in pristine environments. This points to the need for more accurate evidence-based (using charcoal, pollen, phytoliths) understanding of if, when and how land use and land cover changes impact regional vegetation-fire relationships. We are trying to understand this relationship history for Mudumalai National Park, a fire-prone dry forest with $>30\%$ of the park subject to annual fires. For this study, we specifically sample seasonal wetlands, locally called ‘vayals’. The peat core that was dated at IUAC is from an intermediate fire frequency of 2-3 events annually and receives an average rainfall of about 1200-1400 mm per year [1]. The samples were collected using a Russian Peat Borer (RPB) and is ~ 210 cm in length. The sample comprises of five core units (A-E) where each core unit was cut at a resolution of 2 cm. Out of the 115 samples, 25 of them were chosen (5 from each core) for carbon dating at IUAC.

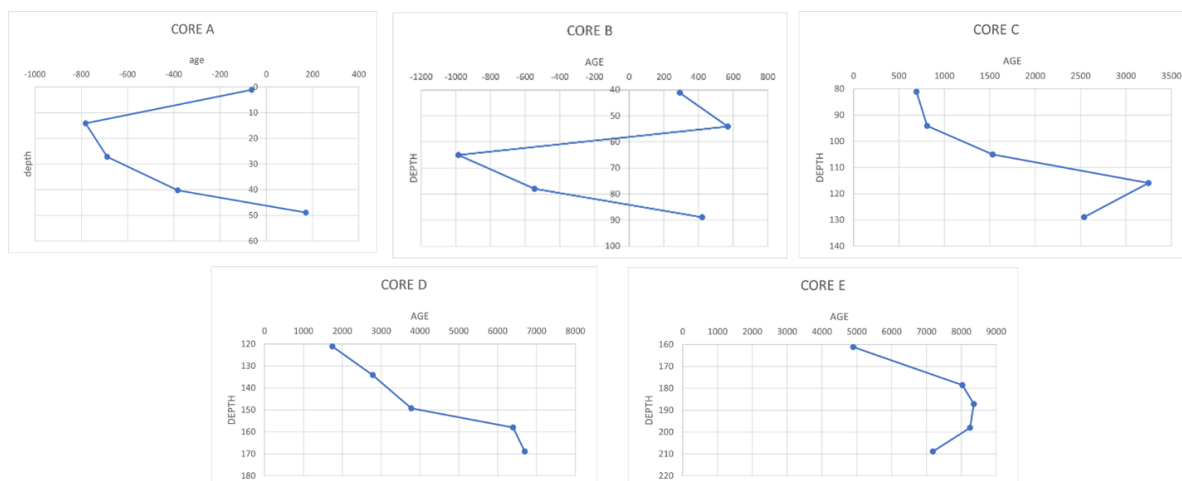


Figure 5.40: Age versus depth for each of the cores.

Carbon dating is critical to constrain the chronology of the wetlands. Our radiocarbon results show that this core goes as far as ~ 7000 years into the past. However, radiocarbon inversions complicate the establishment of a reliable age-depth model, requiring further investigation into the underlying causes. We are attempting to resolve these inconsistencies in the chronology to formulate a robust age-depth model and thus provide an accurate interpretation of historical events. Multi-proxy analysis is under process

to understand the overall temporal patterns of landscape change and human occupation and change; this includes fire proxies (macrocharcoal, microcharcoal and Polycyclic Aromatic Hydrocarbon (PAHs)) and vegetation proxies ($\delta^{13}\text{C}$, pollen and n-alkanes). This will help us in understanding fire intensity, extent and its variability over time and understand fire-vegetation relationships over mid-late Holocene. Such an analysis to characterize the temporal human-fire-vegetation relationships, to our knowledge, is the first from a protected forest in India. This study would also offer critical insights for fire management in forested landscapes.

References:

1. N. Mondal and R. Sukumar, PLOS ONE 11, e0159691 (2016).

5.4 Atomic and molecular physics

5.4.1 Energy and Z dependence of low velocity N^{q+} ion induced M x-ray relative intensities for some heavy elements

Balwinder Singh¹, Shehla², Anil Kumar¹, Deepak Swami³, Ajay Kumar⁴ and Sanjiv Puri¹

¹Department of Physics, Punjabi University, Patiala, Punjab, India

²Department of Physics, Govt Mohindra College, Patiala, India

³Inter-University Accelerator Centre, New Delhi, Delhi 110067, India

⁴Nuclear Physics Division, Bhabha Atomic Research Centre, Trombay, Mumbai 400085, India

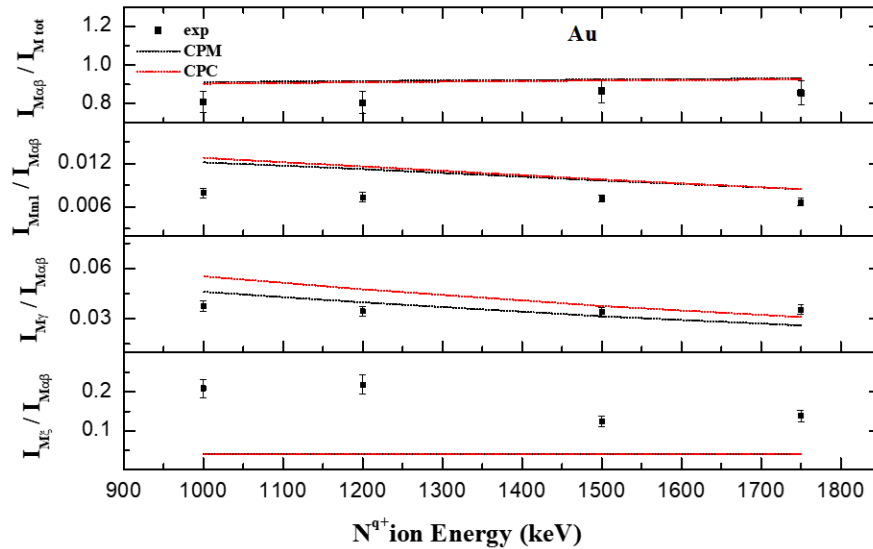


Figure 5.41: A plot of the present measured intensity ratios $I_{Mk}/I_{Mn}(exp)$ ($k=\xi, \gamma, m1$ and $\alpha\beta$; $n = \alpha\beta$ and tot) along with $I_{Mk}/I_{Mn}(CPM)$ and $I_{Mk}/I_{Mn}(CPC)$ for ^{79}Au as a function of incident N^{q+} ion energy.

The interaction of low velocity charged particles with the heavy elements, dominated by direct Coulomb ionization, creates M-shell vacancies. Besides, the target electron captured by the projectile also contribute to the production of M-shell vacancies. Decay of these primary vacancies through non-radiative transition give rise to the Auger electron spectrum, whereas the radiative vacancy decay leads to production of the M-series X-ray lines. Experimental investigation of M X-ray emission is of interest for understanding basic ion-atom collision processes involving tightly bound atomic inner-shell electrons. Accurate and reliable data on the M X-ray relative intensities are required in different applications including plasma studies, investigations of astronomical X-rays, ion-implantations, radiation shielding, radiation dosimetry and elemental analysis employing PIXE technique. Comparison of measured X-ray intensity ratios with the calculated ones provides

5. RESEARCH ACTIVITIES

a testing ground for the theoretical models used to evaluate different physical parameters characterizing the ion-atom collision processes. It may be added that the existing theoretical models used to evaluate different physical parameters ignore the influence of multiple vacancies produced by the incident heavy charge particles.

The intensity ratios, $I_{Mk}/I_{Mn}(exp)$ ($k=\xi, \gamma, m1$; $n=\text{total}, \alpha\beta$), for some heavy elements, ${}_{70}\text{Yb}$, ${}_{79}\text{Au}$, ${}_{81}\text{Tl}$, ${}_{82}\text{Pb}$ and ${}_{83}\text{Bi}$ induced by 1000 – 1750 keV N^{q+} ($q=4, 5$) ions have been measured in order to investigate their dependence on the projectile energy and atomic number of the respective target elements. The measured intensity ratios have been compared with two sets of values calculated using the M_j ($j=1-5$) sub-shell ionization cross sections based on the ECPSSR-UA model [1], the X-ray emission rates based on the Dirac-Hartree Slater (DHS) model [2], two sets of the fluorescence and Coster-Kronig yields based on the DHS model [3] and those evaluated by McGuire [4] employing non-relativistic Hartree-Slater model. Significant differences have been observed between the present measured $I_{Mk}/I_{M\alpha\beta}(exp)$ ($k = \xi, \gamma, m1$) intensity ratios and those calculated using independent particle approximation (IPA) models based single atomic vacancy state physical parameters.

The present measured X-ray intensity ratios, $I_{Mk}/I_{M\alpha\beta}(exp)$ ($k=\xi\gamma, m1$), for ${}_{70}\text{Yb}$, ${}_{79}\text{Au}$, ${}_{81}\text{Tl}$, ${}_{82}\text{Pb}$ and ${}_{83}\text{Bi}$ induced by low energy N^{q+} ($q = 4+, 5+$) ions are found to exhibit significant deviations from calculated values. As specified above, the theoretical values of different M_j ($j=1-5$) sub-shell physical parameters, required to calculate the X-ray intensity ratios, available in the literature are based on the IPA models and these were evaluated considering the single atomic vacancy states. Therefore, calculation of values of these parameters incorporating many-body effects and considering simultaneous presence of outer-shell multiple ionization are highly desired to explain the observed significant discrepancies between present measured and calculated intensity ratios.

References:

1. G. Lapicki, Nucl. Instrum. Methods B **189**, 8 (2002).
2. S. Puri, At. Data Nucl. Data Tables. **93**, 730 (2007).
3. Y. Chauhan and S. Puri, At. Data Nucl. Data Tables **94**, 38 (2008).
4. E. J. McGuire, Phys. Rev. A. **5**, 1043 (1972).